View metadata, citation and similar papers at core.ac.uk

brought to you by CORE

provided by UNT Digital Library

SANDIA REPORT

SAND2004-0482
Unlimited Release
Printed April 2004

Resolving Fundamental Limits of Adhesive Bonding in Microfabrication

Rachel K. Giunta, John A. Emerson, Kerry P. Lamppa, Melissa A. Holmes, Michael S. Kent, Jessica S. Hall, Douglas H. Read, Douglas R. Adkins, Amalie L. Frischknecht, Stacie T. Kawaguchi

Prepared by
Sandia National Laboratories
Albuquerque, New Mexico 87185 and Livermore, California 94550

Sandia is a multiprogram laboratory operated by Sandia Corporation,
a Lockheed Martin Company, for the United States Department of Energy's
National Nuclear Security Administration under Contract DE-AC04-94AL85000.

Approved for public release; further dissemination unlimited.

Issued by Sandia National Laboratories, operated for the United States Department of Energy by Sandia Corporation.

NOTICE: This report was prepared as an account of work sponsored by an agency of the United States Government. Neither the United States Government, nor any agency thereof, nor any of their employees, nor any of their contractors, subcontractors, or their employees, make any warranty, express or implied, or assume any legal liability or responsibility for the accuracy, completeness, or usefulness of any information, apparatus, product, or process disclosed, or represent that its use would not infringe privately owned rights. Reference herein to any specific commercial product, process, or service by trade name, trademark, manufacturer, or otherwise, does not necessarily constitute or imply its endorsement, recommendation, or favoring by the United States Government, any agency thereof, or any of their contractors or subcontractors. The views and opinions expressed herein do not necessarily state or reflect those of the United States Government, any agency thereof, or any of their contractors.

Printed in the United States of America. This report has been reproduced directly from the best available copy.

Available to DOE and DOE contractors from
U.S. Department of Energy
Office of Scientific and Technical Information
P.O. Box 62
Oak Ridge, TN 37831

Telephone: (865)576-8401
Facsimile: (865)576-5728
E-Mail: reports@adonis.osti.gov
Online ordering: http://www.osti.gov/bridge

Available to the public from
U.S. Department of Commerce
National Technical Information Service
5285 Port Royal Rd
Springfield, VA 22161

Telephone: (800)553-6847
Facsimile: (703)605-6900
E-Mail: orders@ntis.fedworld.gov
Online order: http://www.ntis.gov/help/ordermethods.asp?loc=7-4-0#online

SAND2004-0482
Unlimited Release
Printed April 2004

Resolving Fundamental Limits of Adhesive Bonding in Microfabrication

Rachel K. Giunta, John A. Emerson, Kerry P. Lamppa, Melissa A. Holmes
Organic Materials Department

Michael S. Kent, Jessica S. Hall, Douglas H. Read
Microsystems Materials, Tribology & Technology Department

Douglas R. Adkins
Micro-Total-Analytical Systems Department

Amalie L. Frischknecht
Materials and Process Modeling Department

Stacie T. Kawaguchi
Organic Materials Aging and Reliability Department

Sandia National Laboratories
P.O. Box 5800
Albuquerque, NM 87185-0958

Abstract

As electronic and optical components reach the micro- and nanoscales, efficient assembly and packaging require the use of adhesive bonds. This work focuses on resolving several fundamental issues in the transition from macro- to micro- to nanobonding. A primary issue is that, as bondline thicknesses decrease, knowledge of the stability and dewetting dynamics of thin adhesive films is important to obtain robust, void-free adhesive bonds. While researchers have studied dewetting dynamics of thin films of model, non-polar polymers, little experimental work has been done regarding dewetting dynamics of thin adhesive films, which exhibit much more complex behaviors. In this work, the areas of dispensing small volumes of viscous materials, capillary fluid flow, surface energetics, and wetting have all been investigated. By resolving these adhesive-bonding issues, we are allowing significantly smaller devices to be designed and fabricated. Simultaneously, we are increasing the manufacturability and reliability of these devices.

Acknowledgements

The authors would like to thank Patrick Klein for making dynamic viscosity measurements of RSL1462 with T403, PACM, and TETA. They would also like to acknowledge Dave Tallant and Manuel Garcia for their infrared spectroscopy work.

Table of contents

List of figures

List of tables

1 Wetting/dewetting of epoxies

1.1 Introduction

Two general mechanisms are known to lead to the instability of single component liquid films on substrates and a nominal appearance of dewetting. The first is true dewetting, which occurs when the spreading parameter *S* is less than zero, where

$$S = \gamma_{sv} - \gamma_{sl} - \gamma_{lv} . \qquad \textbf{Equation 1-1}$$

Here, γ is the surface tension and the subscript *s* denotes the substrate, *l* denotes liquid, and *v* denotes vapor. In this case, the liquid film completely retracts leaving behind a bare substrate. The second mechanism has been called pseudo partial dewetting [1], and occurs when the excess interface potential $\Phi(h)$ has a global minimum as a function of film thickness (*h*). In this case, the bulk of the film retracts but leaves behind a thin layer of material on the substrate. Since $\Phi(h) \to S$ as $h \to 0$, at short range the excess interface potential is determined by both short-ranged interactions, such as dipole-dipole interactions and hydrogen bonds, as well as by van der Waals interactions. At long range, $\Phi(h)$ is presumably determined only by van der Waals interactions and described by the Hamaker constant for the film on the substrate [2].

Nonpolar, single component polymer films have been studied extensively and the stability of these is fairly well understood. Seeman et al. determined the excess interface potential for the case of polystyrene (PS) on silicon oxide with different oxide thicknesses [3]. Because the sign of the Hamaker constant differs for PS on Si and SiO_2, the shape of the excess interface potential changes qualitatively as a function of the oxide thickness on silicon wafers. This leads to a complex potential function with a global minimum between 8 Å and 12 Å and, for thin oxides, a local maximum at about 20 Å. Having $\Phi(h)$, they were able to establish regimes in which spinodal and nucleation and growth mechanisms were operative.

In contrast to the case of nonpolar single component polymer films, little progress has yet been reported in understanding the much more complicated case of adhesives. Here we consider the case of thin epoxy films. Several complicating factors must be considered with epoxy films. Epoxies involve at least two components referred to below as A and B, which are very different chemically. This raises several issues.

1. The strength of A-B interactions can differ from A-A or B-B interactions. In that case the effective interface potential based only on van der Waals interactions at long range, combined with Equation 1-1 as $h \to 0$, may no longer be an adequate description. For example, fluid structuring or packing effects may occur near the interface that could play a role. To our knowledge, a detailed analysis for the two component case has not yet been derived.

2. The possibility exists for strong preferential segregation at interfaces. If a monolayer of one component were to adsorb to the substrate, an additional

interface would be created, and the stability of the bulk film on the adsorbed layer, rather than on the bare substrate, must then be considered.

3. Since the two components are polar, the influence of water vapor must be considered.

4. While we chose conditions such that reaction of the two components would not be a contributing factor, we discovered that the crosslinking reaction can be accelerated at the interface in some cases.

In this work, we considered three chemical systems composed of Shell Chemical RSL1462 epoxy resin mixed with each of three crosslinkers: T403 (Huntsman), PACM (Air Products), and TETA (Shell). RSL1462 is chemically identical to EPON 828, but is more highly purified (low ionic content). The chemical structures of the resin and crosslinkers are shown in Figure 1-1. These three crosslinkers make an interesting contrast because they have the same functionality (amine) but the rate of the curing reaction with RSL1462 varies in each case. The relative rate of cure is in the following order: TETA > PACM >> T403. In addition, whereas PACM and TETA are symmetric, T403 is asymmetric. Therefore its orientation at an interface may affect the surface energy and its ability to bond with a bulk film, although our work showed no evidence for this. Despite the fact that the chemical functionality of the crosslinkers is the same, we observed dramatically different behavior for the three mixtures.

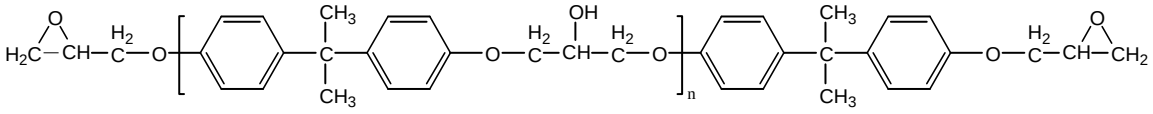

RSL1462 resin

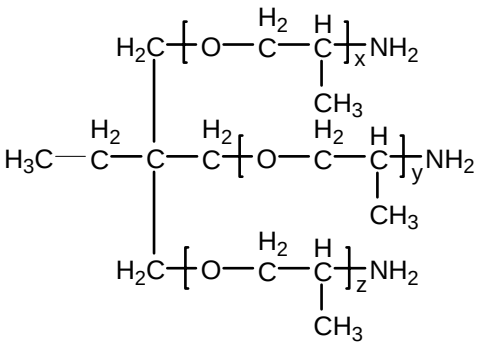

T403 crosslinker

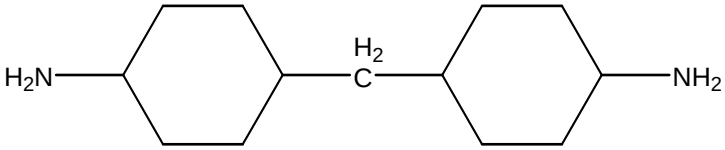

PACM crosslinker

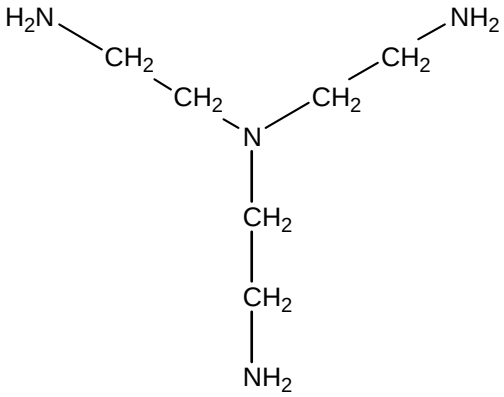

TETA crosslinker

Figure 1-1. Chemical structures of the resin and crosslinkers used in this study.

1.2 Studies involving Shell RSL1462 and T403

When thin films of RSL1462 epoxy resin and T403 amine crosslinker (46 parts T403 per 100 parts resin, or 46 phr) are spin-coated or dip-coated from 10 wt % solution in toluene, they dramatically dewet from silicon wafer substrates. In ambient, dewetting was observable on the time scale of five minutes, as illustrated in Figure 1-2. In contrast, spin coated films of each component alone were stable. This interesting result was further investigated to determine the origin of the behavior. Infrared spectroscopy and dynamic viscosity measurements were used to study the reaction kinetics of the mixture in the

bulk. Wetting/dewetting studies were performed using a variety of substrate surfaces and also varying the level of water vapor present. Surface energetics and the excess interface potential were considered as potential driving forces for the observed dewetting behavior.

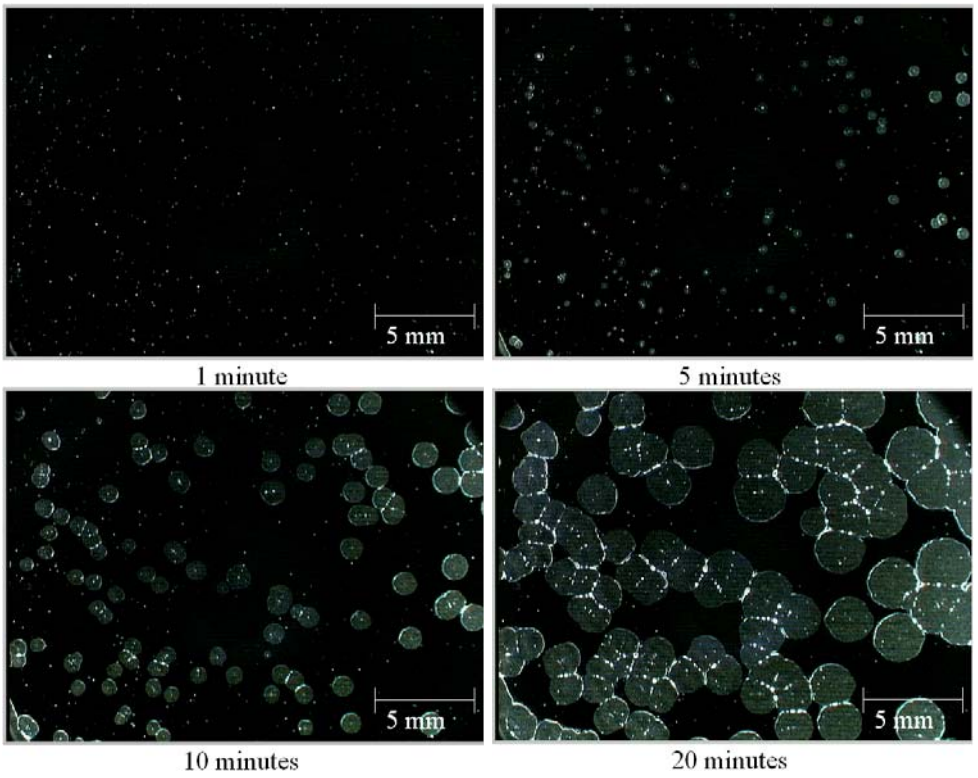

Figure 1-2. Images of thin films of epoxy resin/crosslinker mixture on silicon wafers with native oxide at time increments of 1, 5, 10, and 20 minutes after spin-coating.

1.2.1 Kinetics of the crosslinking reaction in bulk

The extent of cure as a function of time at ambient temperature was obtained using FTIR and dynamic viscosity. For FTIR, the two components were mixed by hand for 5 minutes and then immediately placed between two salt plates and inserted into a N_2-purged compartment of the infrared spectrometer. Spectra were obtained at various time intervals for roughly five and a half days. Following this, the samples were exposed to elevated temperature to achieve full cure, and then final spectra were obtained. Several reference spectra were obtained for each component separately. The extent of cure was calculated using a multivariate analysis of the spectra. The results are shown in Figure 1-3. Of the three systems investigated, the T403/RSL1462 system is by far the slowest curing system.

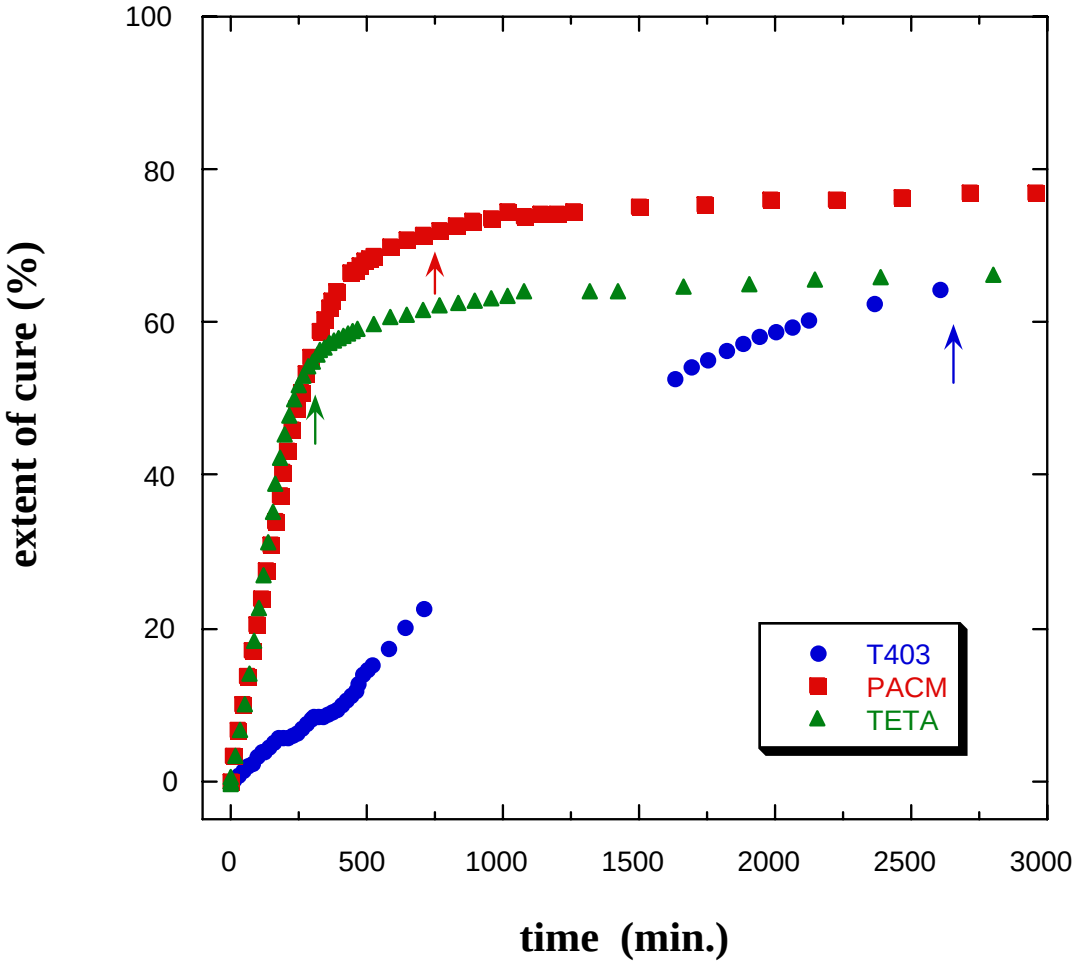

Figure 1-3a. Extent of cure for bulk samples of the three systems as measured by FTIR. Arrows indicate gel time by dynamic viscosity measurements.

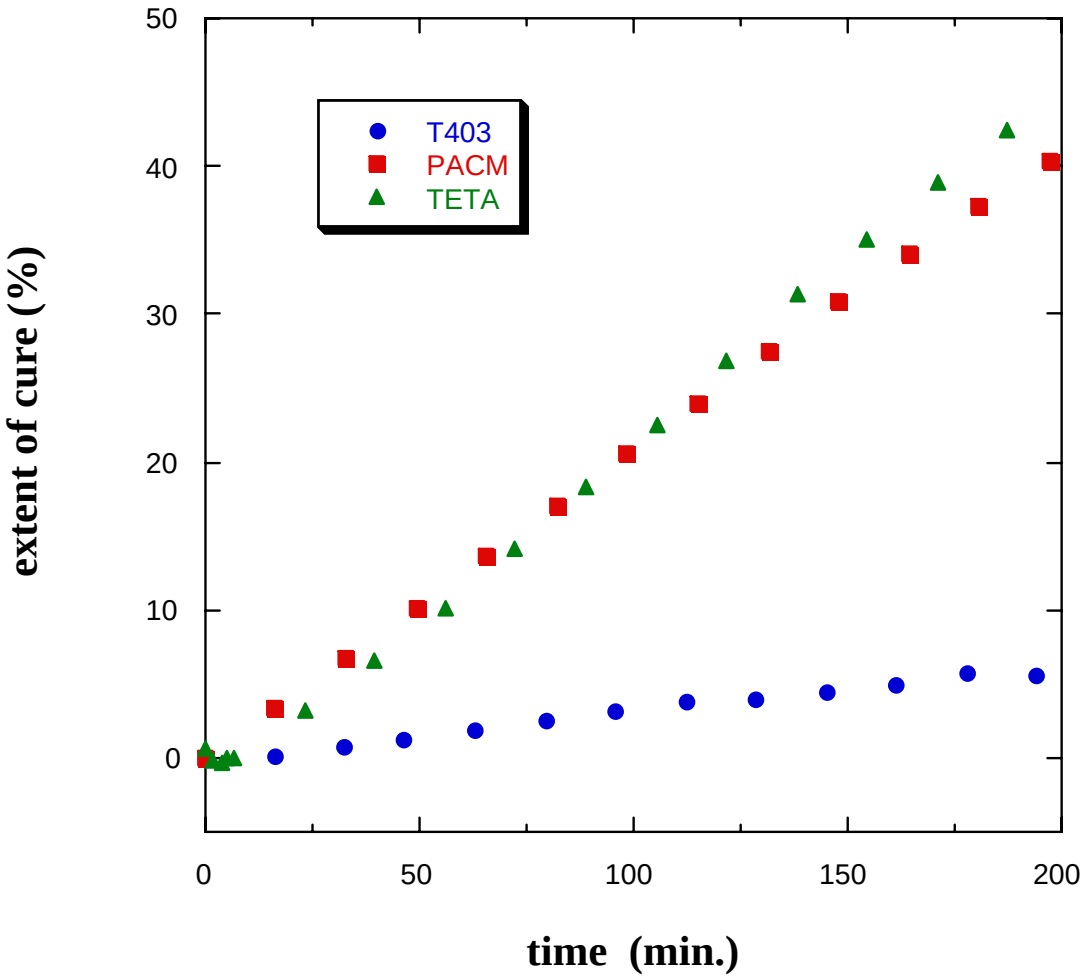

Figure 1-3b. Extent of cure for bulk samples of the three systems as measured by FTIR. Expanded view of the early time data.

For dynamic viscosity measurements, the two components (25-30 g of resin) were mixed by hand for five minutes and then vacuum degassed until foaming ceased, about 10 minutes. The required amount of the mixture (about 0.25 ml) was then transferred to a syringe. Finally, the mixture was dispensed onto the parallel plate fixture, which was inside the N_2-purged rheometer environmental chamber. The environmental chamber was held at a constant 22 ºC for the duration of the test. For the TETA sample cured in ambient conditions, the parallel plate fixture was kept outside of the environmental chamber (~ 21 ºC, 50 % RH). The gel time was determined by the point in time at which $\eta' = \eta''$. The gel time in dry nitrogen is indicated by an arrow in Figure 1-3a. For T403, reasonable agreement was obtained between the gel time by dynamic viscosity and the cure kinetics obtained by FTIR. Results for the other two crosslinkers will be discussed in Sections 1.3 and 1.4 below.

1.2.2 Wetting/dewetting studies

The stability of spin-coated films of the two components was examined on silicon with and without its native oxide as well as on many other substrates. Films were generally prepared by spin-coating at 3000 rpm from a 10 wt % solution in toluene. This gave thicknesses in the range of 2000-4000 Å. The effect of thickness was examined to a limited extent. For thicknesses ranging down to ~500 Å, no qualitative changes in wetting/dewetting behavior were observed. We note that the surface tension values of each bulk component and the mixture in liquid form have been reported previously [4], and values are given in Table 1-1.

Table 1-1. Surface tension of resin, crosslinker, and mixture [4].

Component	Surface tension (mN/m)
T403 crosslinker	33.5
RSL1462 resin	47.8
Resin/crosslinker mix at 46 phr	35.2

Table 1-2 summarizes the observations. The state of the film is characterized in this matrix in a simple manner: "unstable" if the film dewets on the time scale of several days or less and "stable" if the film does not dewet on that time scale. However, we note that there were variations in the appearance of the films that are not captured in this simple matrix. Some images are shown in Figure 1-4a – Figure 1-4g.

Table 1-2. Ambient conditions: matrix of substrates.

Substrate	**Isoelectric point**	**T403**	**RSL1462**	**Mixture**
silicon (native oxide)	2.2	stable	stable	unstable
silicon (no oxide)	n/a	stable	unstable	unstable
Au (50Å)	n/a	--	--	unstable
Au (250 Å)	n/a	--	--	stable
Mo (native oxide)	2.8	stable	stable	unstable
Ta (native oxide)	2.8, -0.7[a]	stable	stable	stable
Ti (native oxide)	5.0	stable	stable	stable
Al (native oxide)	9.0	stable	stable	stable
Ni (native oxide)	10.4	stable	stable	stable

[a] Conflicting values were found in two different references.

In all cases where films were unstable, there was a thin (~8-10 Å) layer of material that remained on the substrate surface. In other words, the bulk material did not dewet from the bare silicon substrate but rather from a thin film of the applied material.

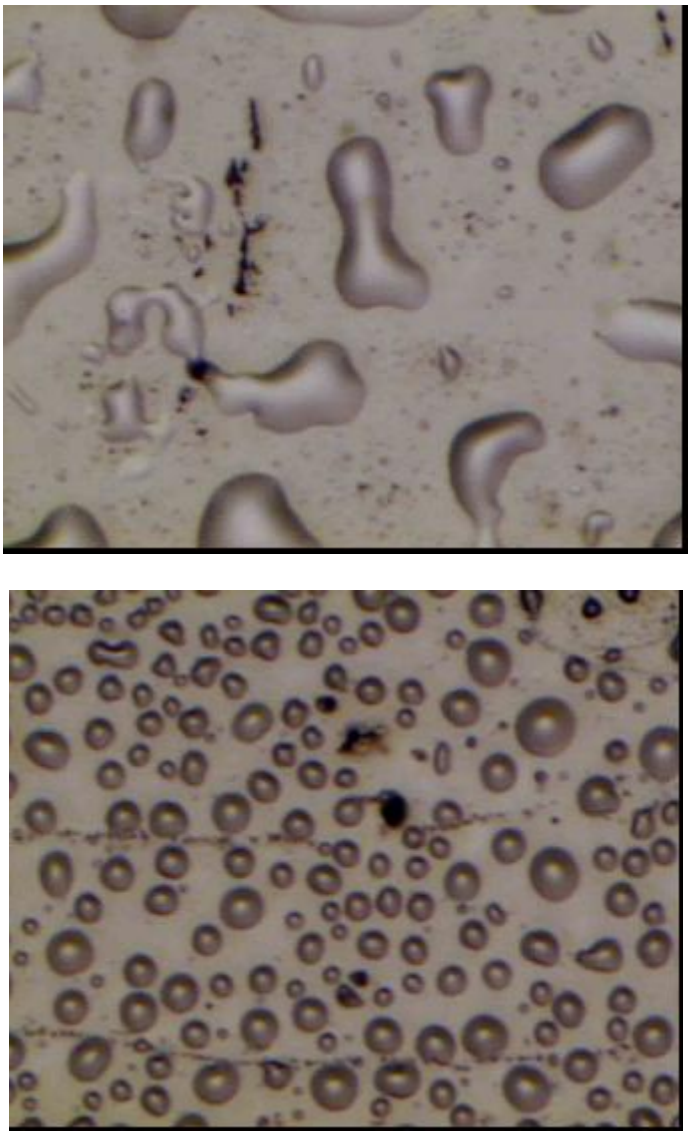

Figure 1-4a. Images of thin films of epoxy resin (top) and the resin/crosslinker mixture (bottom) on silicon wafers with oxide removed with HF. T403 formed a stable film.

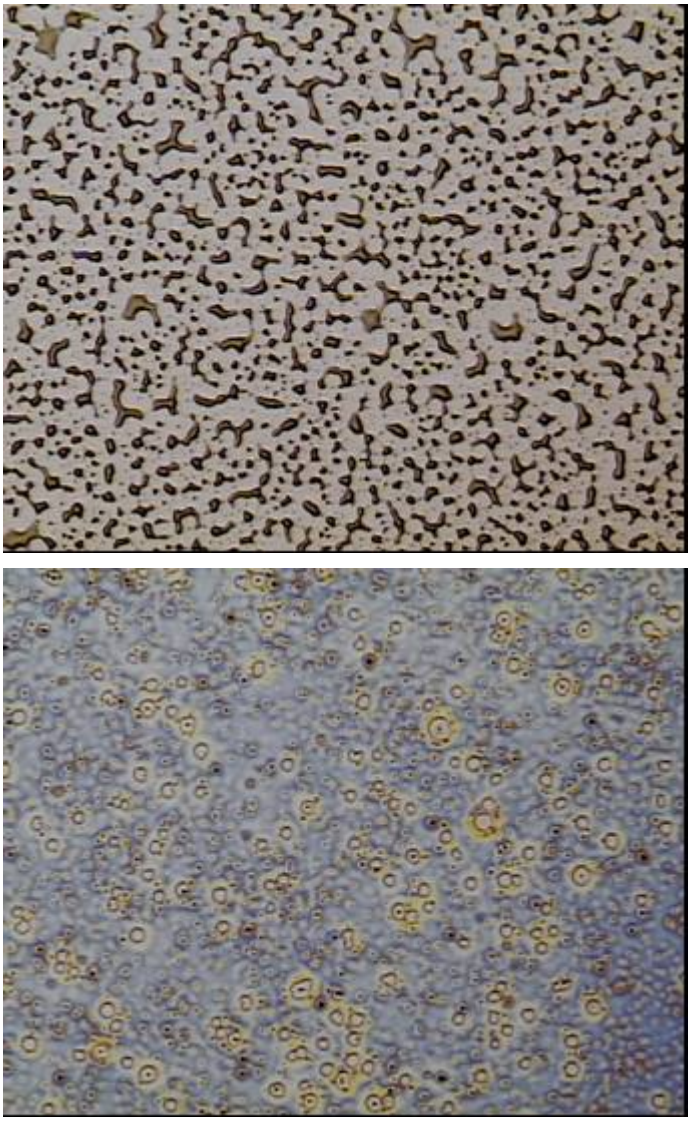

Figure 1-4b. Images of thin films of resin/crosslinker mixture on gold-coated silicon wafers. Thicknesses of the gold coatings were ~ 50 Å (top) and ~ 250 Å (bottom).

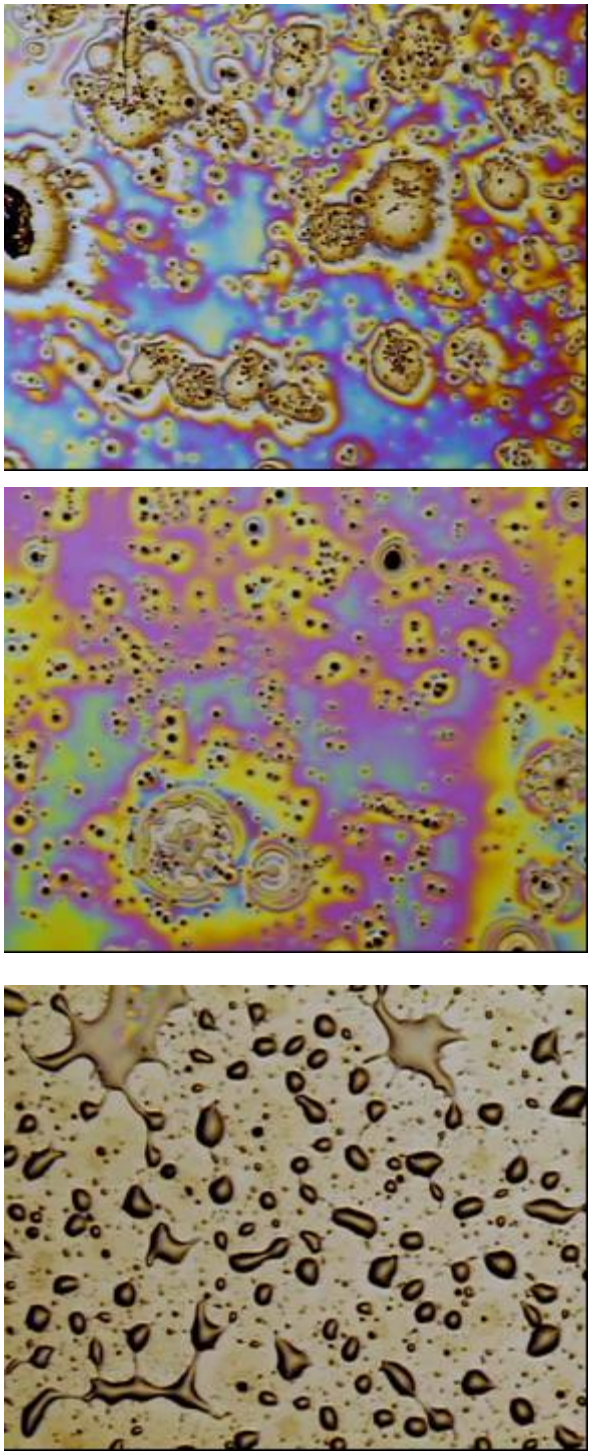

Figure 1-4c. Images of thin films of resin (top), crosslinker (middle), and resin/crosslinker mixture (bottom) on molybdenum-coated silicon wafers. Same magnification in all pictures.

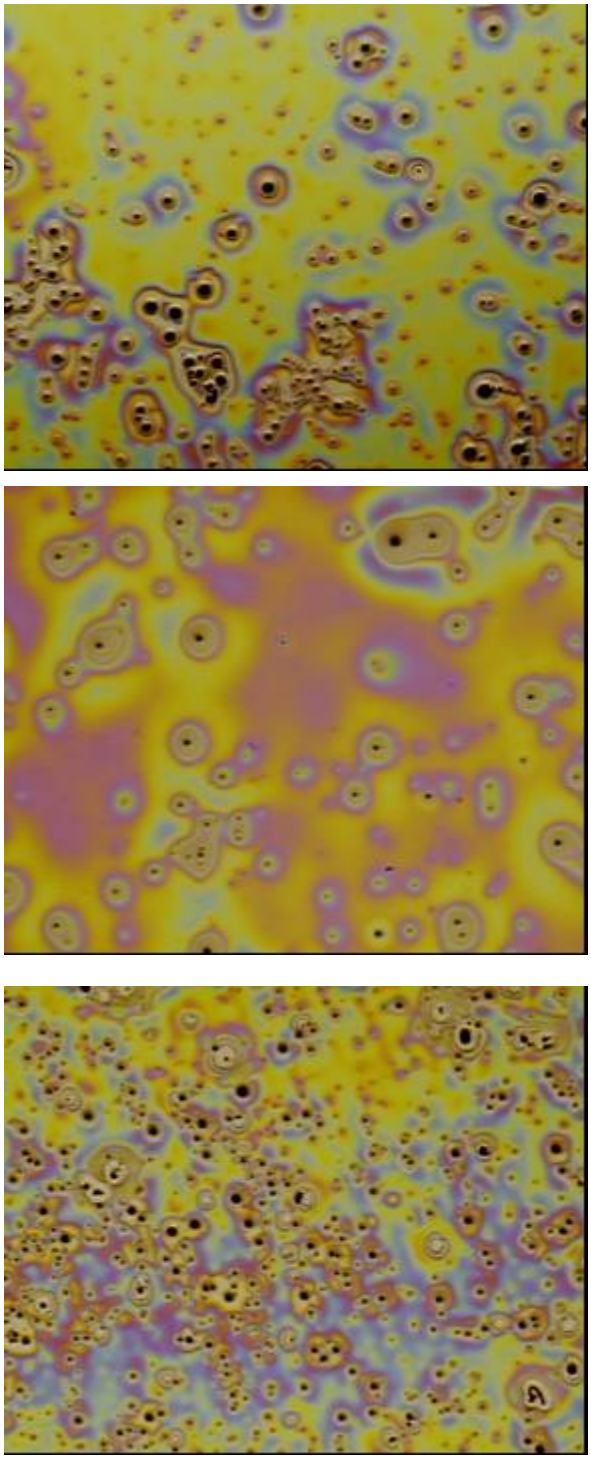

Figure 1-4d. Images of thin films of resin (top), crosslinker (middle), and resin/crosslinker mixture (bottom) on tantalum-coated silicon wafers. Same magnification in all pictures.

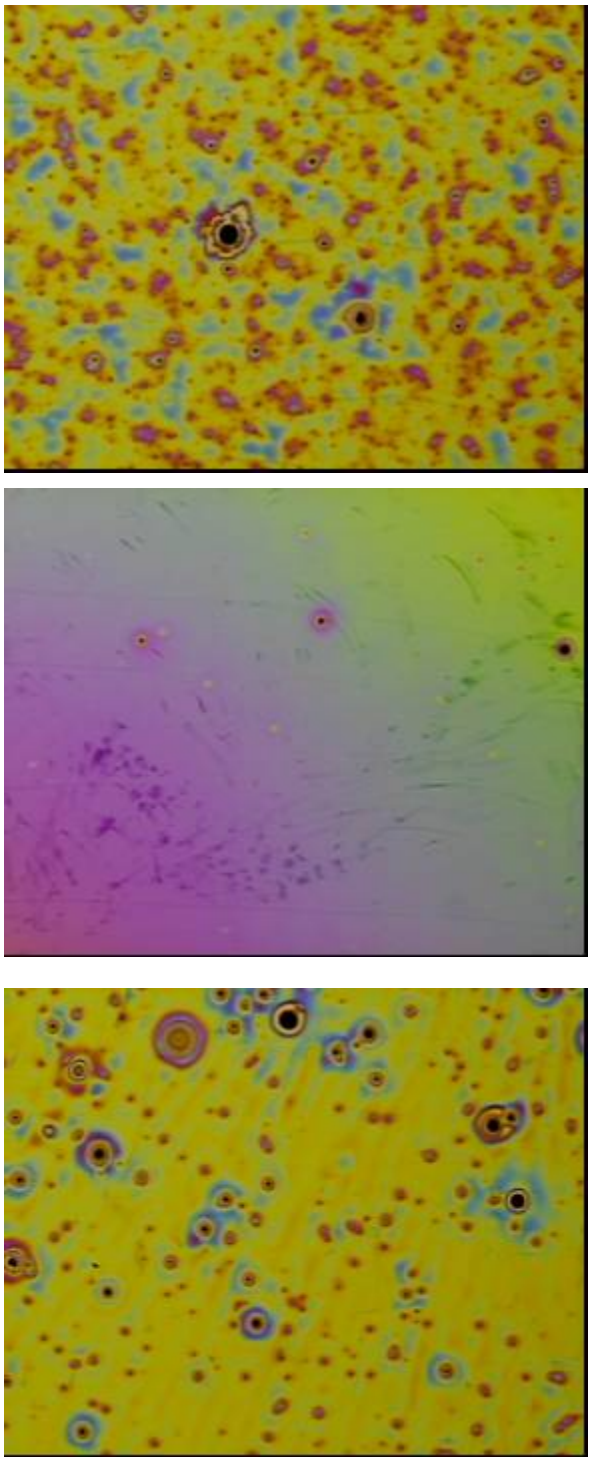

Figure 1-4e. Images of thin films of resin (top), crosslinker (middle), and resin/crosslinker mixture (bottom) on titanium-coated silicon wafers. Same magnification in all pictures.

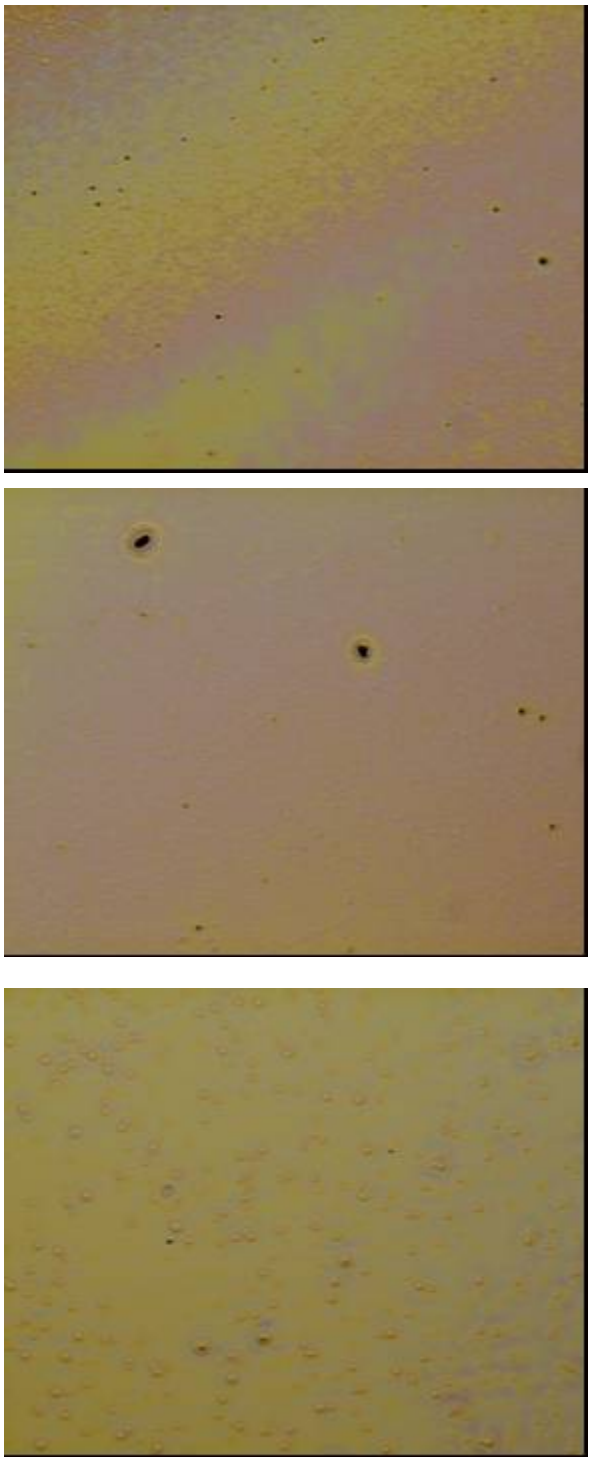

Figure 1-4f. Images of thin films of resin (top), crosslinker (middle), and resin/crosslinker mixture (bottom) on aluminum-coated silicon wafers. Same magnification in all pictures.

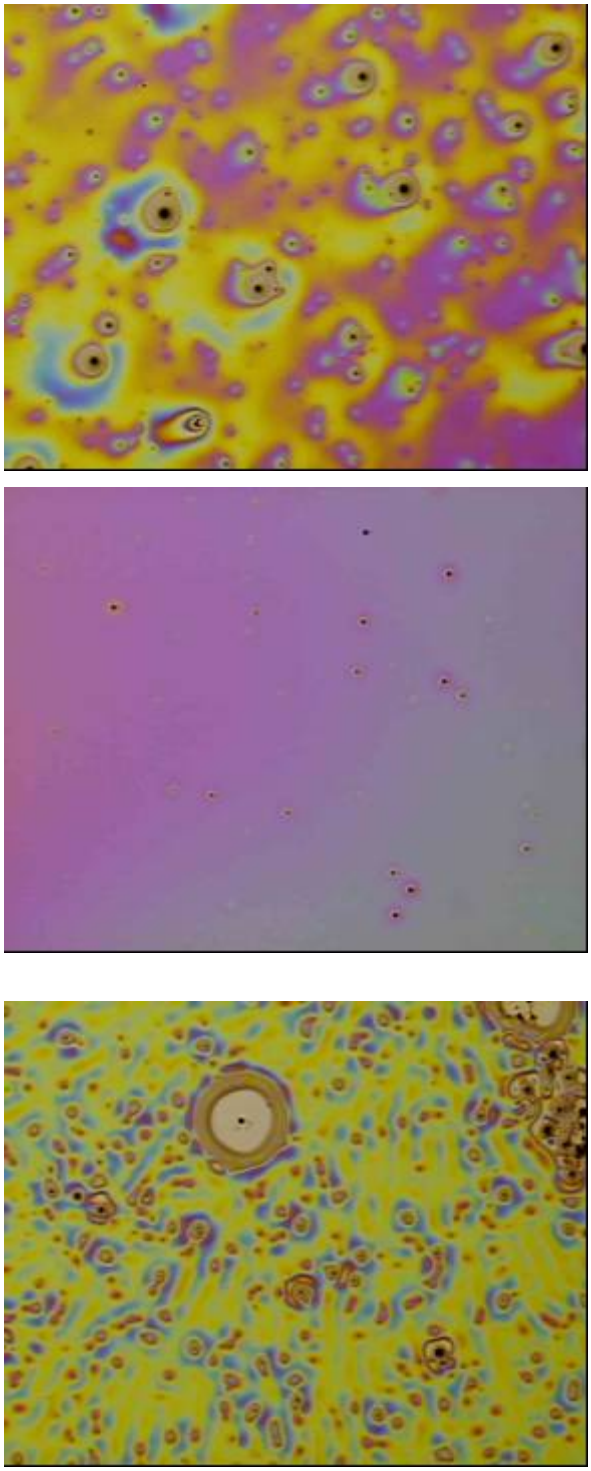

Figure 1-4g. Images of thin films of resin (top), crosslinker (middle), and resin/crosslinker mixture (bottom) on nickel-coated silicon wafers. Same magnification in all pictures.

We note that the behavior of spin-coated films of T403 alone on silicon with its native oxide was somewhat ambiguous in that different results (stable or not) were obtained at different times of the year. We believe this is related to varying humidity levels.

This interesting matrix of observations stimulated much of the work in this phase of the project. We were interested in understanding the factors that control the stability of films of the resin/crosslinker mixture on these various substrates. Several hypotheses were considered during the course of this work.

1. A-B interactions may be much stronger than A-A and B-B interactions. Recent simulations by Grest and coworkers indicate that this can lead to higher contact angles of the mixture on a substrate than for either component separately. In terms of Equation 1-1, this effect can be understood as an increase in γ_{lv} of the mixture. To our knowledge, no detailed analysis yet exists to describe the full effective interface potential in the case of binary mixtures of chemically complex molecules.

2. One of the components may adsorb preferentially and orient in a way that leaves a low energy, non-interacting surface that forms an interface with the bulk film. In particular, amines are known to adsorb strongly onto silicon oxide and glass surfaces based on experimental observations as well as arguments from acid-base interactions. So the T403 crosslinker may adsorb with its amine groups interacting with the surface and the low energy hydrocarbon backbone exposed to the bulk (see chemical structure of T403, Figure 1-1). However, if this occurred uniformly and completely over the entire surface, no chemical links to the bulk would be possible. This clearly cannot be the case as substantial stress can be transferred in joints of this epoxy with silicon oxide.

3. The effective interface potential evaluated solely in terms of dispersion interactions may control the stability. This has been argued for polystyrene films on silicon oxide.

4. The dewetting behavior may correlate with the isoelectric point of the substrate, although we do not expect strong electrostatic interactions with the present materials.

5. The dewetting behavior may correlate with the presence of an adsorbed layer of water on the surface of the substrate.

6. The dewetting behavior may be related to the presence of water vapor and its ability to penetrate through the film and adsorb to the substrate surface.

The stability of the mixture on tantalum countered what seemed to be a general trend with isoelectric point.

In further work we discovered that the timescale of dewetting for the two components on silicon with its native oxide was dramatically slowed when the humidity was reduced.

This motivated the following study of film stability performed in dry conditions, i.e. performed in a glove box and using anhydrous toluene that was never exposed to the ambient. Actually, the experiments in the glove box were performed at different levels of humidity in an attempt to extrapolate to perfectly dry conditions. Whereas the glove box was purged with dry nitrogen, and in some cases the humidity levels were below the measurable limits of our hygrometer, we can be certain that absolute absence of water was never achieved. Table 1-3 gives the matrix of samples examined. In addition to the effect of water vapor, we also studied the effect of compositional variation at the interface. The samples were composed of bulk films spun onto either bare UV-ozone cleaned silicon oxide or onto residual films of resin, T403, or the mixture. Residual films were studied with the intent that they would mimic the 8-10 Å film that remained on the substrate surface after dewetting. Residual films were prepared by spinning bulk films onto UV-ozone-cleaned silicon oxide and then rinsing exhaustively with toluene. A thin ~10–15 Å film was left behind after rinsing, which we refer to as the residual film. In the table below –b indicates the bulk film and –r indicates the residual film.

Table 1-3. Matrix of samples examined. –b indicates the bulk film and –r indicates the residual film.

T403-b on SiO_2	T403-b on T403-r	T403-b on resin-r	T403-b on mix-r
resin-b on SiO_2	resin-b on T403-r	resin-b on resin-r	resin-b on mix-r
mix-b on SiO_2	mix-b on T403-r	mix-b on resin-r	mix-b on mix-r

For comparison, the same combinations were prepared in ambient conditions. Optical images of these films are given in Figure 1-5a – Figure 1-5c.

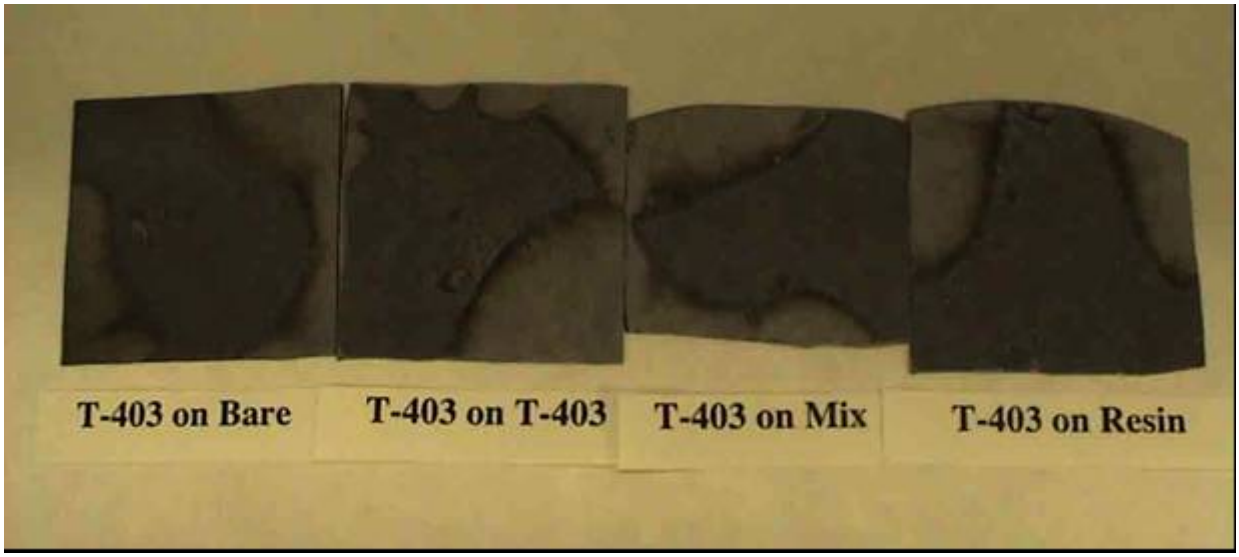

dry air, 3 days

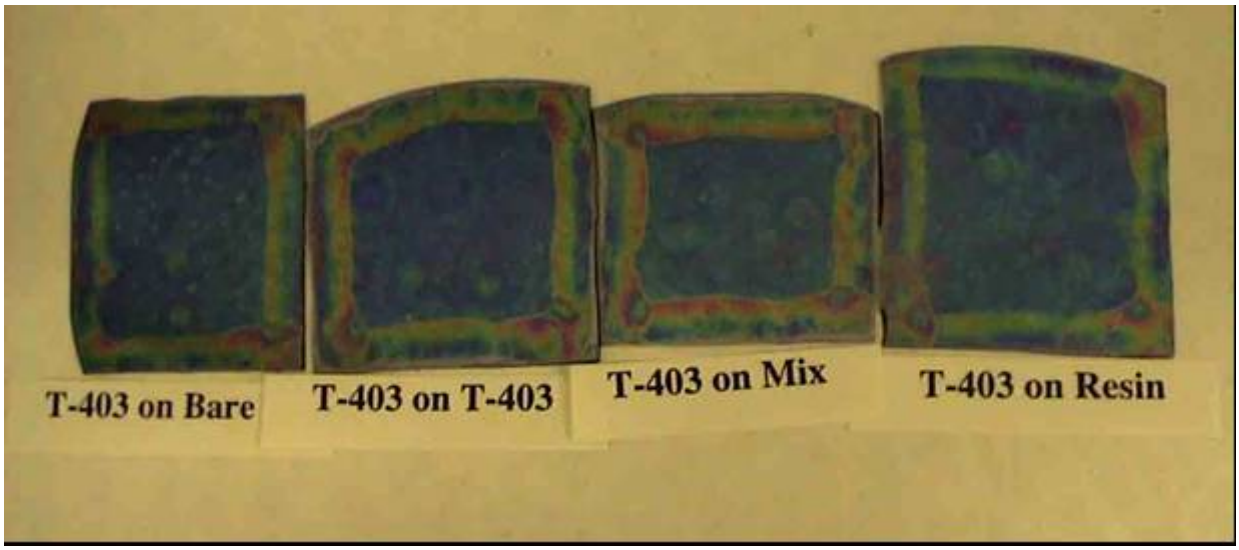

ambient, 3 days

Figure 1-5a. Images of bulk films of T403 on bare SiO_2 and on residual films of T403, the resin, and the 46 phr mixture in dry and ambient conditions.

T403 bulk films: The appearance was the same on all residual films and on bare SiO_2. The behavior is clearly independent of the nature of the residual film, and therefore appears to be driven by the bulk properties of T403. However, the results in dry conditions were very different from the results in ambient conditions. For films spun in the glove box, the films initially appeared grainy, thick, and rough, and no colors were observed. Most importantly, the films pulled in from the edges on a time scale of several days. This is a very different appearance, and presumably mechanism, from the phenomenon observed for dewetting of the resin/T403 mixture, where many holes

nucleate rapidly and then grow. In ambient conditions, films of T403 displayed colors (indicating smooth films) and were stable over several days. However, we note that the color was not uniform over the entire piece, but was different near the perimeter of the pieces, presumably indicating that the film was thinner near the edges. The dramatic difference for the as-spun films in ambient and dry conditions indicates that water vapor affects the films right from the spinning process itself, yielding more stable/smooth films in the presence of water vapor. Also, water vapor stabilizes these films against pulling in from the edges over the long term. The mechanism by which the films dewet from the edges in the dry box is unclear. The fact that there is no dependence on the nature of the residual film in this case is consistent with expectations based on Equation 1-1 considering that T403 has a much lower surface energy than the resin and thus should wet all the residual films if the residual films have surface energies comparable to a bulk liquid of the same composition. The results seem to suggest a cohesive force within the film that is very strong in the case of dry conditions, leading to a grainy appearance and pulling in from the edges, but weaker when water vapor is present.

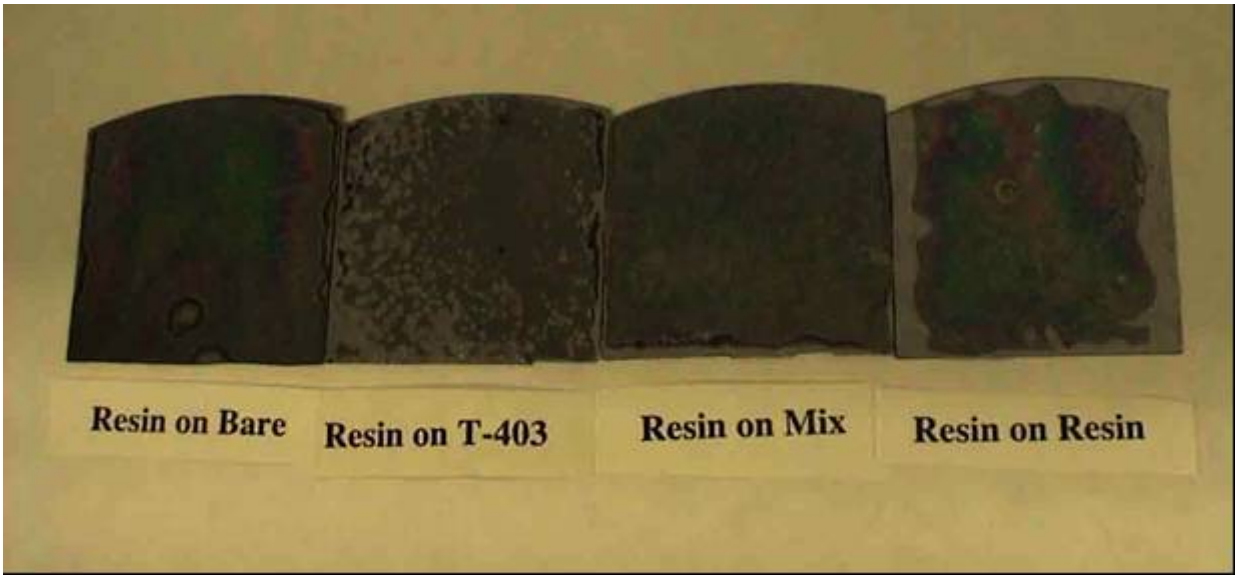

dry air, 3 days

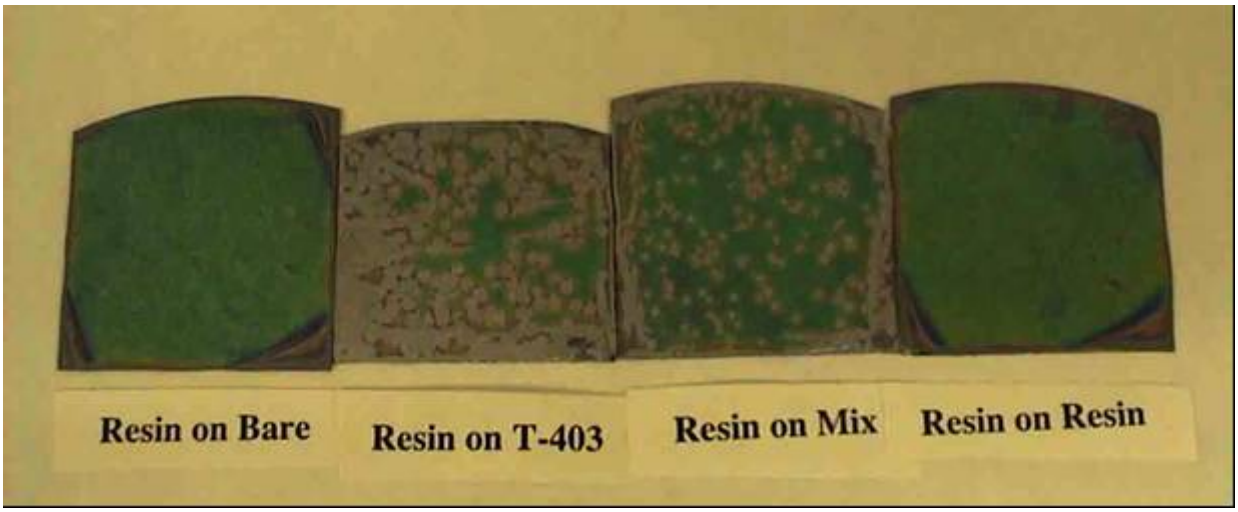

Figure 1-5b. Images of bulk films of RSL1462 resin on bare SiO_2 and on residual films of T403, the resin, and the 46 phr mixture in dry and ambient conditions.

Resin bulk films: The behavior of resin bulk films depended strongly on the presence and composition of the residual films, in stark contrast to the T403 films. The resin bulk film was stable on bare, UV-ozone cleaned silicon oxide both in ambient conditions and in the dry box. However, on a T403 residual film the resin bulk films dewet rapidly by nucleation of holes in ambient conditions, and dewet very slowly with a similar appearance in dry conditions. In this case, the process appears to be the same but water vapor apparently accelerates it. On residual films of the mixture, holes nucleated in ambient but the films never completely dewet. In dry conditions, the film was stable, and few if any holes were observed to nucleate. The bulk resin films were definitely more stable on the residual films of the mixture than on the residual films of T403. Finally, resin bulk films were stable on residual films of the resin in ambient conditions, whereas in dry conditions the resin bulk film pulled in from the edges. Few if any holes nucleated in the latter case. Thus, there appear to be different instability mechanisms for the resin bulk films on the residual films of T403 and the mixture compared to the resin bulk films on bare silicon oxide or residual films of the resin. This suggests that S may play an important role in some of these cases. The data (presence or absence of holes that nucleate and grow) suggest $S < 0$ for bulk resin films on residual films of T403 and the mixture, but $S \geq 0$ for bulk resin films on residual films of bulk resin and bare SiO_2. Since $S = \gamma_{sv} - \gamma_{sl} - \gamma_{lv}$, the above implies that $\gamma_{resin\text{-}r\text{—}vapor} > \gamma_{T403\text{-}r\text{—}vapor}$, assuming $\gamma_{resin\text{-}r\text{—}resin\text{-}b}$ and $\gamma_{T403\text{-}r\text{—}resin\text{-}b}$ are small. This is consistent with the trend in the surface energies of the bulk liquids (see Table 1-1). However, as noted below in Section 1.2.3 we were unable to directly measure differences in surface energy for these residual films. The instability of the resin bulk film on T403 residual films supports the hypothesis that dewetting of the mixture from bare silicon oxide could be driven by preferential segregation of T403 resulting in a low surface energy interfacial film.

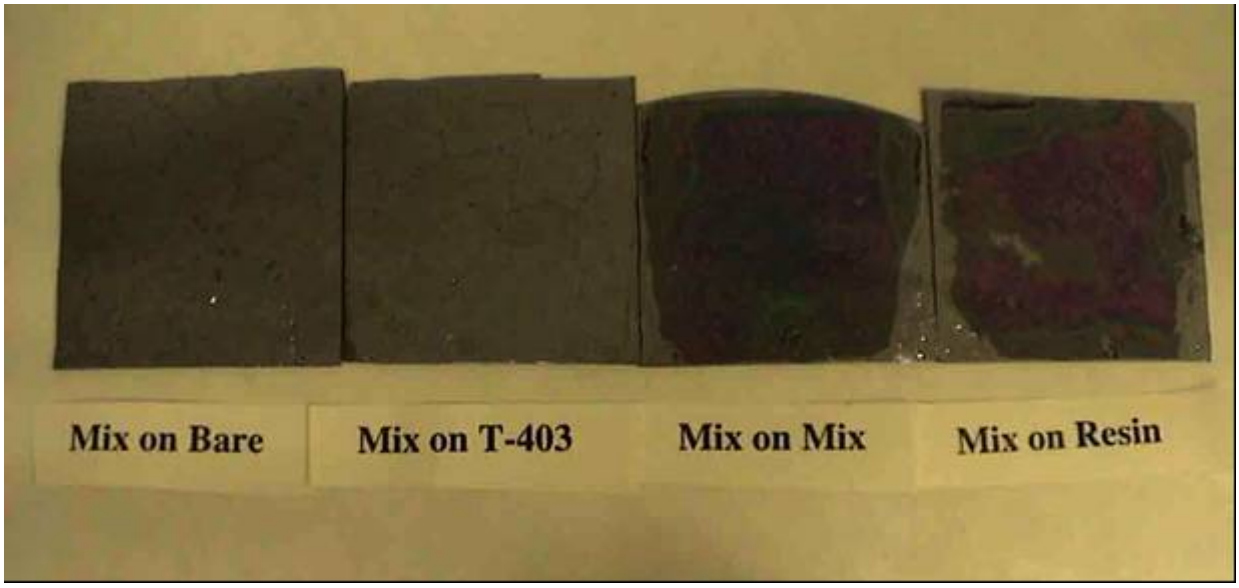

dry air, 3 days

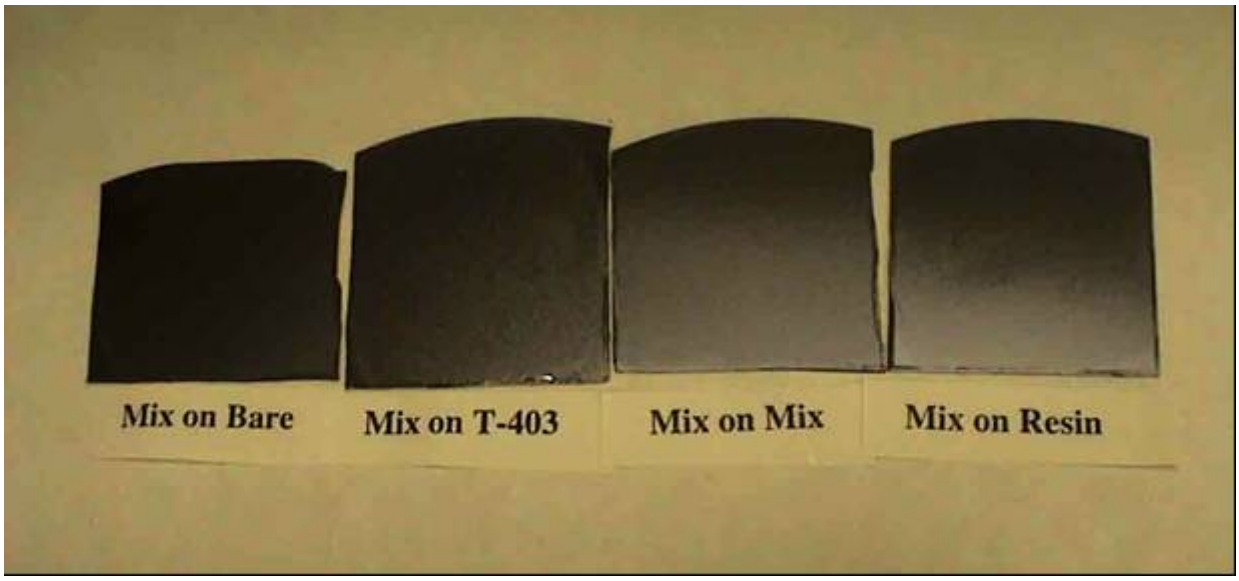

ambient, 8 minutes

Figure 1-5c. Images of bulk films of the mixture on bare SiO_2 and on residual films of T403, the resin, and the 46 phr mixture in dry and ambient conditions.

Bulk films of the mixture: Bulk films of the mixture showed a dramatic dependence on both the presence and composition of the residual film as well as on the humidity level. In ambient, the bulk film of the mixture rapidly dewetted from all residual films as well as from bare silicon oxide. In dry conditions, the bulk film of the mixture also dewetted from bare silicon oxide, but this occurred over a much longer time scale. Furthermore, fewer holes nucleated with progressively drier conditions. Since we could never obtain a

condition where the air was 100% free of moisture, the extrapolation of this behavior is unclear. That is, it is unclear whether dewetting would be entirely absent in absolutely dry conditions or whether it would occur very slowly from only a few or one nucleation site. The observations for the bulk film of the mixture on residual films of T403 were similar to those on bare silicon oxide: rapid dewetting in ambient, progressively slower dewetting in progressively drier conditions. However, the results were different for bulk films of the mixture on the residual films of the mixture and resin, in that the bulk films were stable against nucleation of holes in dry conditions on the timescale of 3 days. In each case, the bulk films pulled in from the edges to some extent. The instability of the bulk film of the mixture on T403 residual films supports the hypothesis that preferential segregation of T403 could drive dewetting of the mixture from bare silicon oxide.

Thus, clearly at least two mechanisms are involved. The first is indicated by nucleation from holes, and the second is indicated by pulling in from the edges. Table 1-4 summarizes which conditions produced stable films, films that were unstable by the first mechanism, and films that were unstable by the second mechanism. We point out that the presence of water vapor has opposite effects on stability for the two mechanisms. Water vapor promotes instability in the first mechanism but induces stability in the second mechanism. The first mechanism dominates for bulk films of the mixture in ambient on all residual films. The second mechanism dominates for T403 bulk films on all surfaces in dry conditions. For many cases, both mechanisms appear to be present.

Table 1-4. Summary of bulk film stability on bare SiO_2 and on residual films of T403, resin, and the mixture. Unstable-1 indicates that the film dewet by nucleation from holes. Unstable-2 indicates that the film pulled in from the edges.

Dry Air

	Substrate			
Bulk film	SiO_2	T403-r	resin-r	mix-r
T403	unstable-2	unstable-2	unstable-2	unstable-2
resin	stable	unstable-1	unstable-2	stable
mix	unstable-1	unstable-1	unstable-2	unstable-2

Ambient

	Substrate			
Bulk film	SiO_2	T403-r	resin-r	mix-r
T403	stable	stable	stable	stable
resin	stable	unstable-1	stable	unstable-1
mix	unstable-1	unstable-1	unstable-1	unstable-1

Several observations with respect to the first mechanism can be understood in terms of the spreading parameter, *S*, and support the hypothesis that preferential segregation of T403 could drive dewetting of the mixture from bare silicon oxide. The instability of the resin bulk films and bulk films of the mixture on T403 residual films supports this hypothesis, especially considering the absence of this dewetting mechanism for resin bulk films and bulk films of the mixture on resin residual films. In addition, the fact that the first mechanism is completely absent for the T403 bulk films (dry and ambient, and on all residual films and bare silicon oxide) is consistent with surface energy arguments. T403 has the lower surface energy of the two components and thus should be stable ($S < 0$) on any composition of residual film.

A few other interesting points can be made. It is unclear whether water vapor simply accelerates an existing nucleation process in the first mechanism, or actually alters the thermodynamic stability. In some cases, the nucleation of holes appears to be completely eliminated in dry conditions (e.g. resin-b on mix-r and mix-b on resin-r and mix-r), but in other cases holes nucleate in both conditions and the presence of water vapor simply increases the rate of nucleation (resin-b on T403-r and mix-b on T403). There is strong evidence that the first mechanism does not involve phase separation of the two components. First, it depends on surface characteristics – the mixture dewets dramatically on some surfaces but is stable on other surfaces. Second, the resin film dewets by this mechanism on residual films of T403 and the mixture in ambient conditions.

1.2.3 Surface energy studies

Attempts were made to measure the surface energies of the residual films left behind after exhaustive rinsing with toluene. We expected that surface energy measurements would explain some of the dewetting observations of the previous section based on the values of *S*. Unfortunately, the data were inconclusive. In that regard, the surface energies of the residual films were probed using contact angle measurements and the well-known JKR contact mechanics technique. Again, we note that the surface tension values of each bulk component and the mixture in liquid form have been reported previously to be 33.5 mN/m (T403), 47.8 mN/m (resin), and 35.2 mN/m (mix at 46 phr), Table 1-1.

Contact angle method:

Table 1-5 presents contact angle data that were obtained for various liquids on the residual films.

Table 1-5. Contact angles of liquids on residual films, in degrees.

	Residual film composition		
Liquid	**Resin**	**T403**	**Mixture**
DI water	50 ± 1	50 ± 1	51 ± 1
glycerol	62 ± 2	63 ± 2	48 ± 3
methylene iodide	12 ± 2	56 ± 2	57 ± 2
formamide	40 ± 3	33 ± 2	33 ± 2
ethylene glycol	44 ± 2	37 ± 2	27 ± 2

These data lead to widely varying estimates of surface energies for the residual films based on the two-liquid equations using either the harmonic mean method or the geometric mean method [5]. This is shown in Table 1-6, where p, d, and t correspond to the polar component, dispersive component, and the total surface energy, respectively.

Table 1-6. Calculated surface energies (harmonic mean) of residual films, in mN/m.

		Resin			T403			Mixture		
Liquid 1	**Liquid 2**	**p**	**d**	**t**	**p**	**d**	**t**	**p**	**d**	**t**
DI water	methylene iodide	24	36	60	31	21	53	30	21	51
glycerol	methylene iodide	2	51	53	13	24	37	27	21	48
ethylene glycol	methylene iodide	7	43	50	16	23	39	20	22	42
glycerol	ethylene glycol	13	24	37	23	15	38	13	35	48
DI water	formamide	30	22	52	29	25	54	27	26	53
methylene iodide	formamide	8	42	50	46	20	66	48	20	68

Unfortunately, the wide variation in these values does not allow a conclusion to be made about the relative magnitudes of the surface energies for each component and the mixture. This wide variation for the different liquid pairs may indicate that the monolayer films rearrange to some extent upon contact with the liquids. The data do appear to indicate that the polar component is much greater for the T403 residual than for the resin residual film.

Contact mechanics method:

We also probed the surface energy of the residual films using the JKR contact mechanics approach. A probe sphere of polydimethylsiloxane was used. The data are shown in Figure 1-6. While very little variation is seen in the unloading curves, especially near the point of pull-off, small variations are observed in the loading curves. The contact radius was consistently smaller on the mixed residual film upon loading than for the T403 or resin residual films. It is unclear whether this is significant. It could indicate a higher surface energy for the residual film of the mixture relative to the residual films of the resin or T403. This would be consistent with stronger A-B interactions than A-A or B-B interactions. We note that this is not necessarily in conflict with the relative values of the bulk liquid surface tensions. Whereas for the bulk liquid mixture, preferential segregation will occur such that the surface energy of the mixture is intermediate between that of the two components, whereas such segregation may not occur within residual films of the mixture due to interactions with the substrate surface.

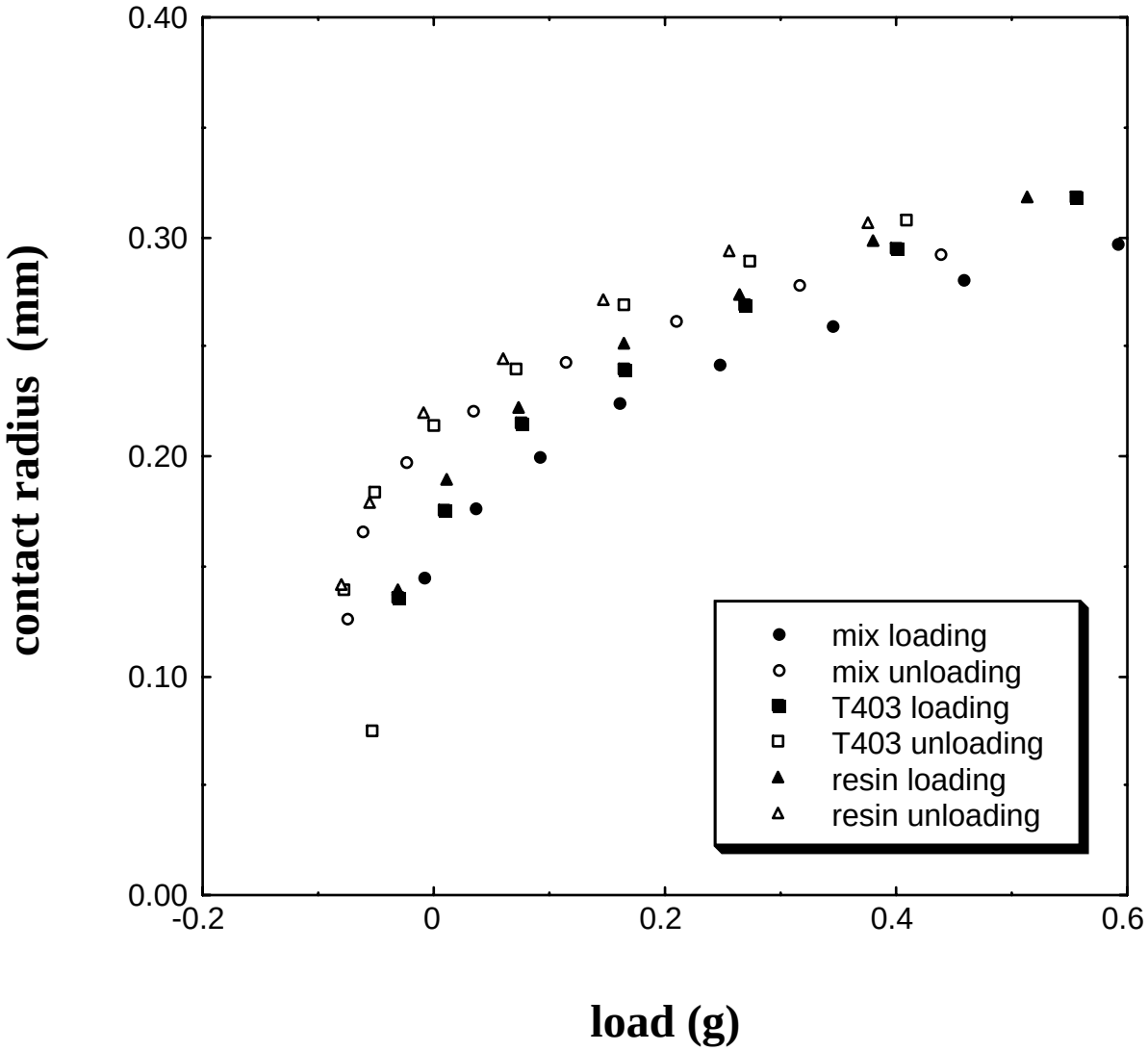

Figure 1-6. JKR data for PDMS hemispheres on residual films of T403, RSL1462 resin, and a 46 phr mixture.

1.2.4 Composition of the residual film by FTIR/ATR

It was hoped that measurement of the composition of the residual film left behind after dewetting of the mixture would provide the explanation for dewetting, and in particular, test the hypothesis of preferential segregation of T403. However, we were unable to measure the composition of the thin film left behind after dewetting, and so we focused our efforts instead on measuring the composition of a residual film of the 46 phr mixture left behind after a dip-coated film was exhaustive rinsing with toluene. Application of this information to the dewetting problem then requires the assumption that the compositions of the residual films achieved by the two routes are comparable. The composition of the residual layer was probed with FTIR-ATR. Our approach to

estimating the relative amounts of RSL1462 resin and T403 crosslinker in the residual film of the mixture on a silicon ATR plate was to reproduce the spectrum of the mixture by summing ATR spectra of films of the resin and crosslinker alone with known thicknesses. The individual resin and crosslinker spectra were scaled in intensity to achieve the best fit to the spectrum of the mixture. The factors used to scale the resin and crosslinker spectra were then multiplied by the thicknesses measured for the resin and crosslinker calibration coatings to get equivalent thicknesses for the resin and crosslinker in the mixed film.

Several infrared (IR) spectra were obtained in each case. From these, we have selected three that best represent the RSL1462 epoxy resin, the T403 amine crosslinker and the 46 phr mixture. We obtained the IR spectra by the ATR technique, using silicon ATR plates as the substrates on which the epoxy components were deposited. In this geometry, the coating was sampled by multiple reflections of the IR beam. The IR spectra selected were of dip- and spin-coated samples. The dip-coated samples had one toluene rinse or a "light" rinse. Some samples with additional rinses showed evidence for contamination during rinsing or chemical reaction. The spin-coated sample was not rinsed. Where there were multiple spectra of the same coating and rinsing conditions, the spectrum obtained at the longest instrument purging time was selected, since purging minimizes atmospheric water and carbon dioxide bands. A summary of the spectra and samples selected is given in Table 1-7. The spectra are shown in Figure 1-7a – Figure 1-7c.

Table 1-7. Spectra and samples selected for thickness calibration

Spectrum	***Date Obtained***	***Coating***
MIRF06	7/25/02	Resin: ATR plate "F", dipped in RSL1462 (0.5% solution)–Light Rinse
MIRN03	7/25/03	Crosslinker: ATR plate "N", T403 (spun, 0.1% in toluene)
MIRD03	7/9/02	Mixture: ATR plate "D", dipped in RSL1462 + T403 (1 Rinse)

Figure 1-7a shows IR spectra of a relatively thick film of RSL1462 resin between salt windows and a "dipped" film of the resin on an ATR plate (see Table 1-7). The thickness of the dipped film on the ATR plate was measured by ellipsometry to be 38 ± 12 Å. We normalized the intensities of the spectra to facilitate their comparison. The significant differences between the spectra are believed to be due to orientation effects and reaction of the resin in a near monolayer film on the ATR plate. Specifically, the methylene ($-CH_2-$) C-H stretching modes of the sample on the ATR plate are enhanced relative to the C-H stretching modes of its methyl ($-CH_3$) and aromatic and epoxide ring C-H groups. The low-intensity, broad band from 3100 to 3500 cm^{-1} is due to hydroxyl groups. The intensity of this band increases with repeated rinsing. Its presence is most likely due to reaction of epoxide groups.

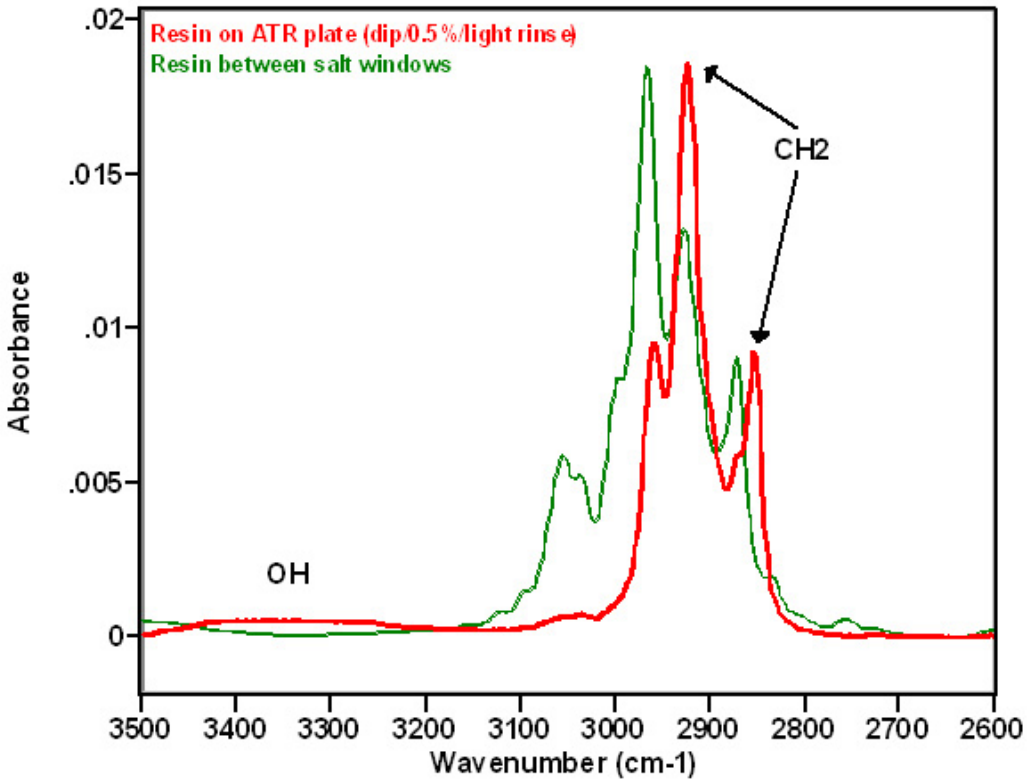

Figure 1-7a. IR spectra of RSL1462 resin between salt windows and on ATR plate.

Figure 1-7b shows IR spectra of a relatively thick film of T403 crosslinker between salt windows and a "spun" coating of T403 on an ATR plate (see Table 1-7). The thickness of the spun film on the ATR plate was measured by ellipsometry to be 25 ± 6 Å. The spectra in Figure 1-7b are relatively similar, but, as with the spectra of the resin (Figure 1-7a), bands due to methylene C-H groups (especially the band peaking near 2925 cm^{-1}) tend to be enhanced in the spectrum from the coating on the ATR plate. Note that bands due to N-H (amine) stretching motions (3100 – 3500 cm^{-1}) are present in both spectra in Figure 1-7b. This indicates that most of the amines groups are free, i.e. not complexed with each other or with surface silanols.

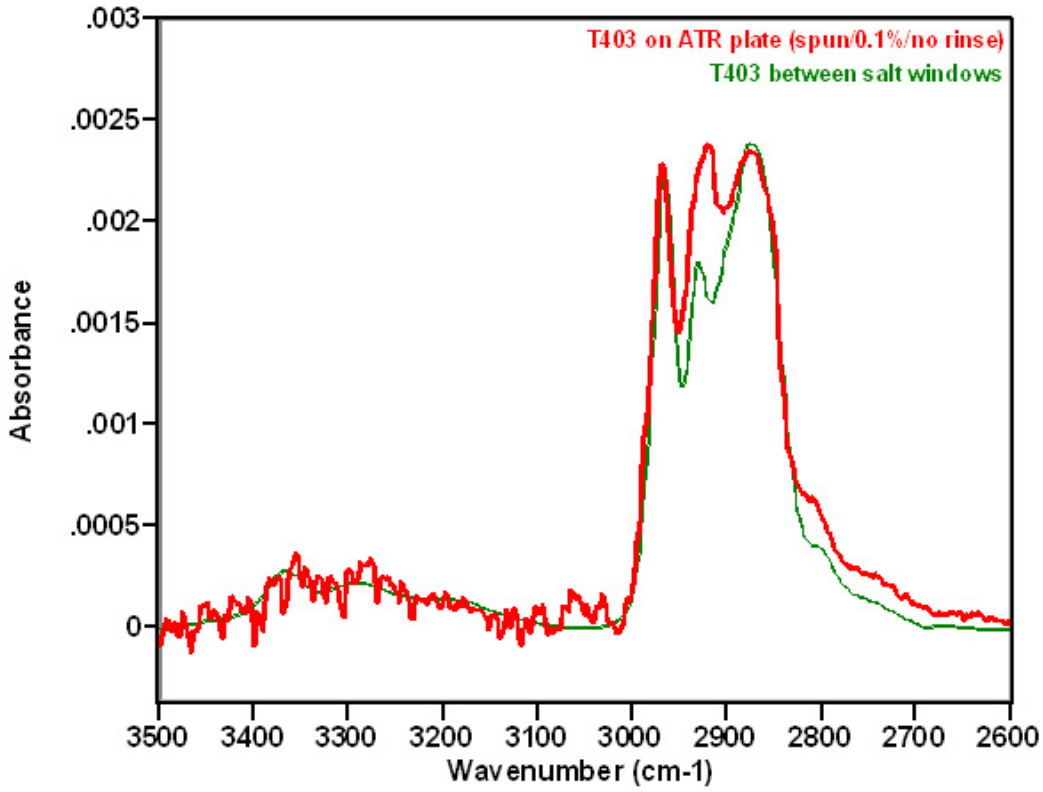

Figure 1-7b. IR spectra of T403 crosslinker between salt windows and on ATR plate.

In Figure 1-7c, we show the results of our attempt to reproduce the spectrum of the 46 phr mixture of RSL1462 resin and T403 crosslinker on an ATR plate (see Table 1-7) by summing ATR spectra of the resin (Figure 1-7a) and that of the T403 crosslinker (Figure 1-7b). The thickness of the dipped and rinsed film on the ATR plate was measured by ellipsometry to be 16 ± 15 Å. The wide variation obtained for multiple measurements reflects the variation in thickness over the surface area of the ATR crystal resulting from the dip and rinse procedure. The best fit of the summed spectra to the ATR spectrum of the resin/crosslinker mixture was obtained by scaling the intensities of the ATR spectra of both the resin and the crosslinker by 0.4. Therefore, the equivalent thicknesses of the resin and crosslinker in the mixture on the ATR plate can be obtained by multiplying the measured thicknesses for the resin coating alone and the crosslinker coating alone by 0.4. This gives an equivalent thickness of 15.2 Å of resin and 9.8 Å for T403. Using densities for T403 and RSL1462 of 0.98 g/cm^3 and 1.17 g/cm^3, respectively, this corresponds to a weight fraction of 0.35 for T403. The error is estimated at ±20 %. The bulk composition of 46 phr corresponds to a T403 weight fraction of 0.32. Thus, this measurement does not provide support for the hypothesis of preferential absorption of T403. However, we note that the residual film obtained by rinsing with toluene may differ from that left behind after dewetting.

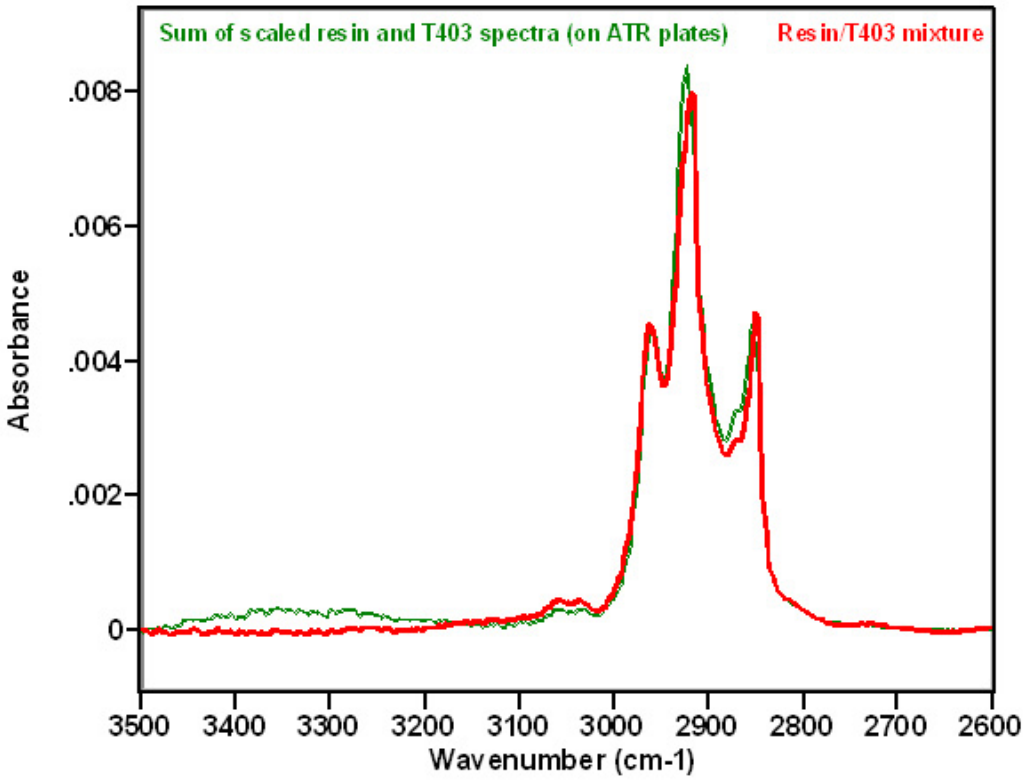

Figure 1-7c. IR spectra of Resin/T403 mixture on ATR plate and fitted spectrum (0.4 times ATR resin spectrum - Figure 1-7a– plus 0.4 times ATR crosslinker spectrum – Figure 1-7b).

1.2.5 Effective interface potential – vary oxide thickness

We explored the effective interface potential $\Phi(h)$ as calculated from the dispersion interactions alone as a possible contributing factor in some of our observations. Following Seeman et al., we used the following equation to model the three-interface system of silicon/SiO_2/organic film/air:

$$\Phi(h) = \frac{c}{h^8} + \Phi_{VDW}(h) \qquad \textbf{Equation 1-2}$$

and

$$\Phi_{VDW}(h) = \frac{-A_{SiO_2}}{12\pi h^2} + \frac{A_{SiO_2} - A_{Si}}{12\pi (h+d)^2} \qquad \textbf{Equation 1-3}$$

where h is the film thickness, d is the oxide thickness and A_i are the Hamaker constants. The term c/h^8 is a cut-off to capture short-ranged interactions. At $h = 0$ the excess interface potential must equal S (Equation 1-1), which is very large for organic films on silicon oxide due to the large value of γ_{sv} for rigorously clean silicon oxide. In our calculations, we used the value of c determined for PS by Seeman [3]. However, we note

that this is not well understood and is actually a phenomenological parameter set by the thickness of the residual film left behind after dewetting and the contact angle of the dewetted bulk on the residual film. The Hamaker constants were calculated from Equation 11.13 in ref. 2.

The refractive indices and dielectric constants were measured for T403, RSL1462, and the 46 phr mixture. These are required for calculation of the A_i using Equation 11.13 in ref. 2. The values are given in Table 1-8, along with the values for polystyrene, silicon, and silicon dioxide.

Table 1-8. Refractive indices and dielectric constants of materials of interest.

	Refractive index	Dielectric constant
T403	1.4605	8.96
RSL1462	1.5712	5.53
mixture	1.517	7.24
PS	1.557	2.55
silicon	3.883	12.5
SiO_2	1.448	3.8

As expected, the refractive index and dielectric constant for the mixture falls close the weighted average of the values for the two individual components. From this, it is immediately clear that this approach cannot account for the fact that the films of the mixture dewet under conditions for which films of the resin and crosslinker are stable.

Nevertheless, we explored the effects of varying the thickness of the oxide on the stability of bulk films of T403 and the resin, as Seeman et al. reported previously for PS. In addition, we attempted to reproduce the results reported by Seeman et al. for PS films on silicon oxide. Calculated excess interface potential plots are given in Figure 1-8 as a function of oxide thickness. The Hamaker constants, calculated using Equation 11.13 from ref. 2 and the data in Table 1-8, are given in Table 1-9.

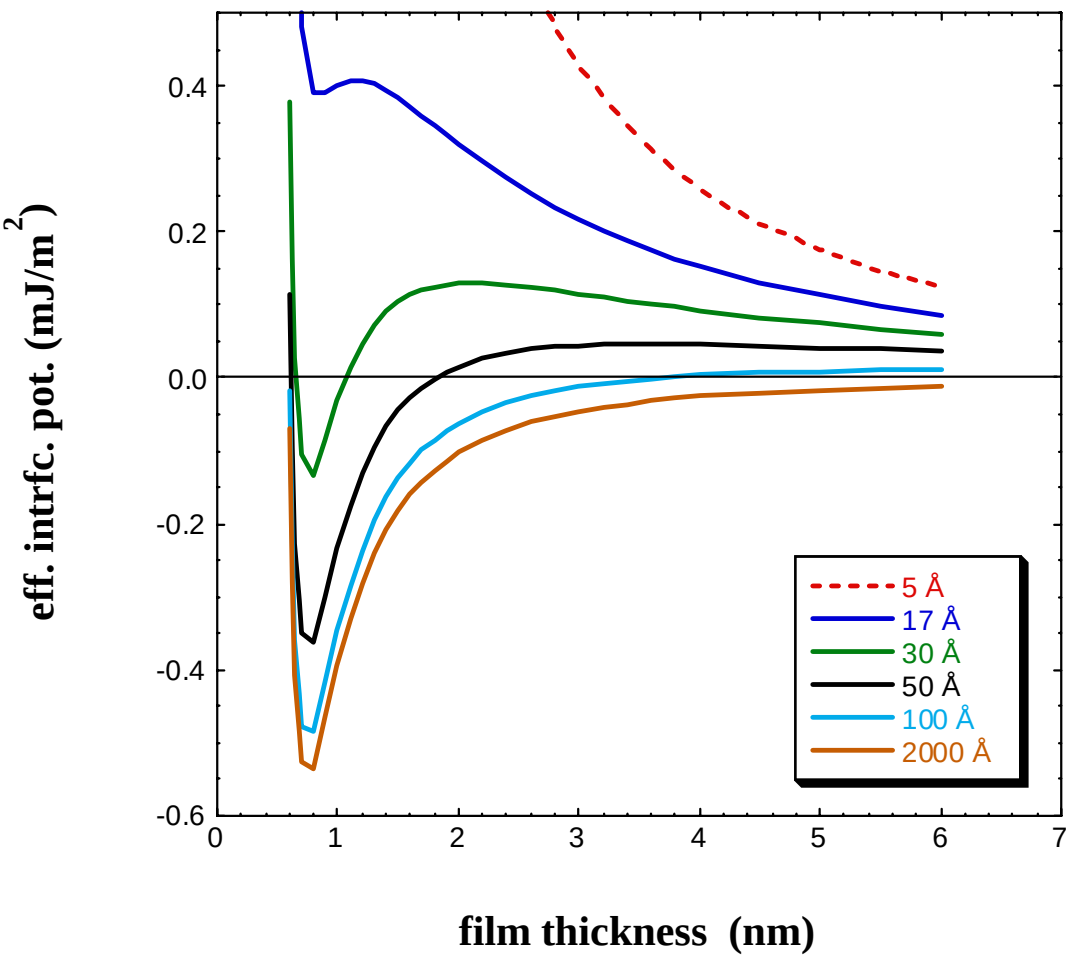

Figure 1-8a. Excess interface potential for PS on silicon dioxide as a function of oxide thickness.

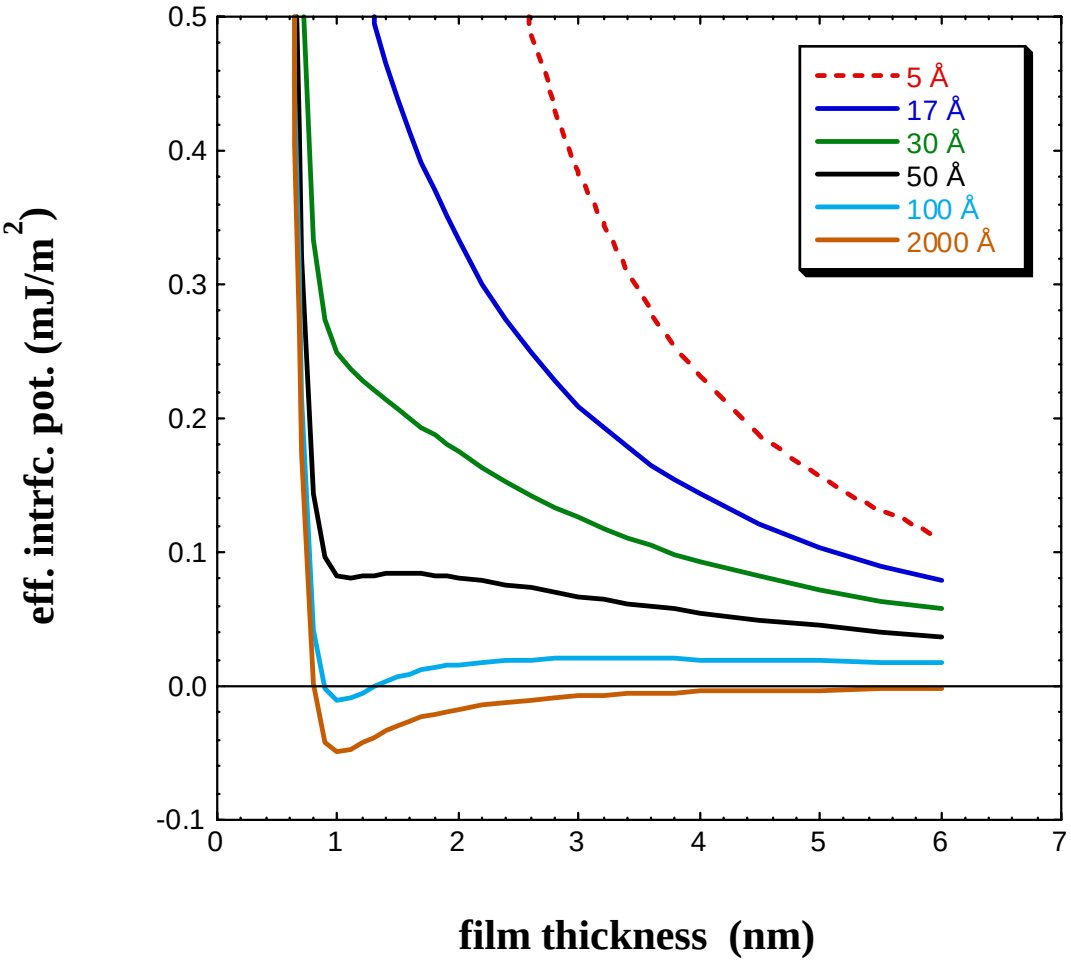

Figure 1-8b. Excess interface potential for T403 on silicon dioxide as a function of oxide thickness.

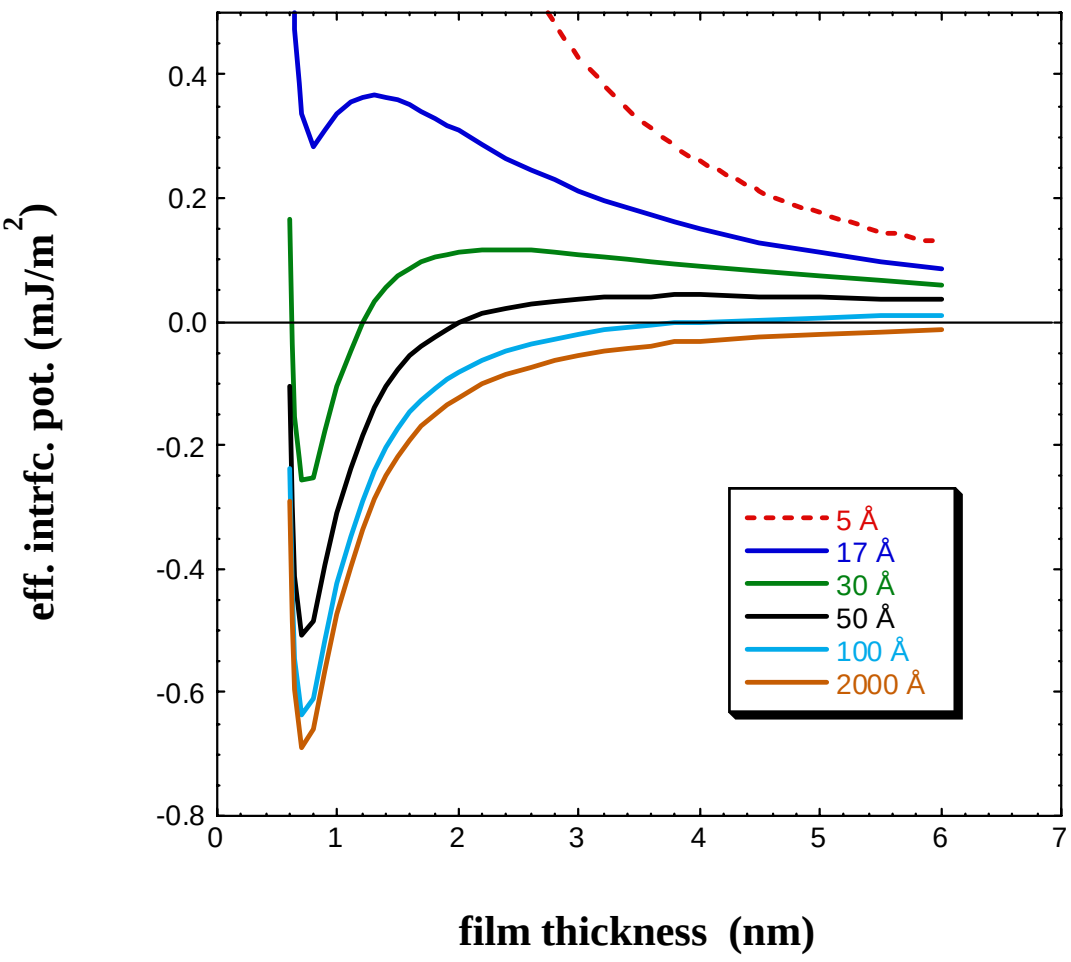

Figure 1-8c. Excess interface potential for RSL1462 resin on silicon dioxide as a function of oxide thickness.

Table 1-9. Hamaker constants calculated from refractive index and dielectric constant data.

Film/substrate	Hamaker constant (A)
PS/SiO_2	1.55e-20
PS/Si	-2.03e-19
Resin/SiO_2	1.85e-20
Resin/Si	-2.04e-19
T403/SiO_2	2.55e-21
T403/Si	-1.78e-19
Mixture/SiO_2	1.01e-20
Mixture/Si	-1.94e-19

The plot of the effective interface potential for PS in Figure 1-8a is somewhat different from that reported by Seeman et al. [3]. This is due mainly to the fact that Seeman et al. fixed the value of the effective interface potential at the minimum for the different oxide thicknesses, which they derived from the contact angle for dewetted PS on its residual film. As a result, the thickness at the minimum varied as a function of oxide thickness. In other words, they assumed that the contact angle was constant and the thickness of the residual film changed with oxide thickness, and in our calculations, we assumed that the thickness of the residual film is constant and the contact angle varies with oxide thickness. Unfortunately, these details regarding the first term are critical to predicting metastability, but are not well understood. Our choice was based on the fact, discussed further below, that we did not observe nucleation of holes for PS films on silicon wafers in a dry box. In addition, another difference between our calculation and that of Seeman et al. is that we used the calculated values of the Hamaker constants whereas Seeman et al. determined Hamaker constants experimentally from the dominant wavelength of fluctuations in the spinodally dewetting regime. For PS/SiO_2 and PS/Si, he obtained 2.2e-20 J and –1.3e-19 J, respectively. While these values are in rough agreement with the calculated values in Table 1-9, the difference is significant. For the calculated Hamaker constants the minimum in the effective interface potential is greater than 0 for silicon with a native (20 Å) oxide, indicating stability. However for the experimentally derived values of Seeman et al. the minimum is well below zero for silicon with a native oxide, indicating metastability.

Thus, using the calculated parameters in Table 1-9 and a fixed residual film thickness, a transition in stability is predicted to occur as a function of oxide thickness, starting from a stable film on the native oxide and becoming unstable with increasing thickness of the oxide.

The effective interface potential plots for T403 in Figure 1-8b indicate stability on nearly all thicknesses of silicon oxide. Only for very thick oxide layers do the calculations suggest that the films may become marginally unstable. The small minimum arises from the fact that the refractive index of T403 used in the calculation is slightly greater than that used for silicon oxide. If these numbers are slightly off, such that they were equal or the refractive index of T403 were less than that of silicon oxide, a minimum would not

exist. On the other hand, films of the resin are predicted to be stable at oxide thicknesses comparable to that for the native oxide (20Å), but to be clearly unstable for thick (2000 Å) oxide films. Thus, in both cases a transition from stable to unstable is predicted to occur as a function of oxide thickness. This transition is expected to be very dramatic for the resin, but much weaker for T403. However, we reiterate that this assumes the value of *c* in the first term in Equation 1-2 is the same for both T403 and the resin, and equal to the value Seemann et al. obtained for PS.

Observations of film stability and dewetting morphology were made for PS, T403, and the resin on silicon wafers with the native oxide as well as on silicon with a 2000Å thermal oxide. Side by side experiments were performed in ambient conditions and in dry conditions using a nitrogen-purged glove box. The results are summarized below.

Dry conditions (glove box):

PS films: On native oxide, the films (substrate heated to 150°C) were stable with respect to nucleation of holes on the time scale of 1 day. However, the films began to pull in very gradually from the edges. On the 2000 Å thermal oxide, the films (substrate heated to 150°C) began immediately dewetting by nucleation of small holes. However, the films never completely dewet as the holes did not grow indefinitely. This variation with oxide thickness may be the effect as a function of oxide thickness that is predicted in Figure 1-8a. More work is required to confirm this.

T403 films: On native oxide, the films were stable against nucleation of holes out to three days, but pulled in from the edges as shown previously in Figure 1-5a. The results were the same on the 2000 Å thermal oxide. This lack of variation with oxide thickness can be considered consistent with the plots in Figure 1-8b in that the predicted effect is marginal.

Resin films: On native oxide, the films were stable out to three days as shown previously in Figure 1-5b. On the 2000 Å thermal oxide, the films were stable against nucleation of holes, but began to pull in from the edges on a time scale of several days. The fact that in dry conditions no transition from stable to unstable was observed contrasts with the expectation based on the effective interface potential plot in Figure 1-8c. This cannot be explained by uncertainty in the value of *c* in the first term in Equation 1-2, as the film should be unstable on the 2000 Å oxide no matter what value of *c* is used. It may indicate that the effective interface potential based only on dispersion interactions is insufficient to describe the behavior of the chemically complex resin molecules interacting with the silicon oxide surface. This is an important finding and should be pursued in future work.

Ambient conditions:

PS films. In ambient conditions, we were not able to reproduce the same dewetting morphologies as reported by Seeman for films of PS with molecular weight of 2K spun from a 2 wt% solution in toluene. In particular, we did not observe the nucleation and growth of holes on either a ~ 20 Å native oxide or a 2000 Å thermal oxide. No obvious dewetting occurred for either oxide thickness even upon heating the substrate to 115°C to

lower the viscosity and facilitate dewetting. A small number of very small holes appeared on some samples, but this was ambiguous, as these holes did not appear to grow with time. The discrepancy between our observations and those of Seeman may be related to differing levels of water vapor in the air in the two cases. We note that Seeman did not control the humidity in his experiments (personal communication). Nucleation of holes in the PS film could either be accelerated or impeded by water vapor. Perhaps a different level of humidity in Seeman's case could explain the much more prevalent appearance and growth of holes in his experiments. We did not have time to explore the stability in the presence of a high level of humidity. More work is needed on this topic.

T403 films: On native oxide, the films spun from a 10% solution in toluene were uniform and stable over several days. As mentioned earlier, the long-term stability of T403 films on native oxide in ambient varied somewhat with the time of year, and we attribute this to varying levels of humidity. In this case, (films prepared in January with very low humidity), the films were stable. On the other hand, on the 2000 Å thermal oxide, the films were uniform as spun, but holes gradually nucleated and the films completely dewet over a period of 2 days. This contrasts with the results in dry conditions described above where no difference was observed for the two oxide thicknesses. The fact that differences in film stability are only observed for the two oxides in the presence of water vapor is puzzling. It is possible that the surface chemical composition is somewhat different for the two types of oxides, such that the thermal oxide interacts more strongly with water vapor leading to dewetting in that case.

Resin films: On native oxide as well as on the 2000 Å thermal oxide, films of the resin spun from 10% solutions in toluene were stable over a period of three days. Thus, whereas the transition from stable to unstable with increasing oxide thickness was expected to be more dramatic for the resin films than for the T403 films, no transition in stability was observed for the resin films. We do not have an explanation for this, but suggest that it may indicate that an effective interface potential based only on dispersion interactions is insufficient to describe the behavior of the chemically complex resin molecules.

1.2.6 Summary

We do not have a model that describes all the wetting/dewetting observations for films of the mixture and of each component on the various substrates and residual films. Clearly two mechanisms (at least) are involved and water vapor plays an important role. Interestingly, water vapor has an opposite effect on stability for the two mechanisms. The main observation was the dewetting of films of the mixture on certain substrates for which each component individually was stable. The data at present do not allow a definitive conclusion regarding this dewetting mechanism. The observations of the stability of bulk films on the various residual films supports the hypothesis that preferential adsorption of T403 could drive dewetting of the mixture, however we were unable to obtain direct evidence of such a segregation. Clearly, the simple excess interface potential based only on dispersion interactions is not a complete description of these systems. Moreover, that approach appears to be inadequate even for thin films of the resin alone, as strong instability was predicted as a function of oxide thickness, but was not observed. We propose that a systematic study be undertaken of A-B mixtures

having similar optical properties but varying in chemical functionality to shed more light on this. In addition, we note that molecular simulations should provide important insights.

1.3 Studies involving Shell RSL1462 and PACM

To gain further insight into our hypothesis of preferential adsorption of T403 leading to dewetting of the RSL1462/T403 system, we studied the wetting behavior of RSL1462 with two other crosslinkers—PACM (Air Products) and TETA (Shell). The structures of PACM and TETA are shown in Figure 1-1. In this section we discuss the studies involving PACM.

1.3.1 Kinetics of the crosslinking reaction in bulk

The extent of cure as a function of time at ambient temperature was obtained using FTIR and dynamic viscosity. Details of these procedures and results are given in Section 1.2.1.

1.3.2 Wetting/dewetting studies and the growth of crosslinked interfacial films

Wetting/dewetting studies were performed on silicon with its native oxide. Films were prepared by spin-coating as well as by dip-coating. Surprisingly, the difference in coating method had an important impact on the dewetting behavior in some cases.

Spin-Coating:

The spin-coating protocol was as follows. Wafers were treated with UV-ozone for various times. Solutions of the two components were deposited onto the wafers within a few minutes after UV-ozone treatment, and then left to sit for 1 minute. The wafers were then spun at 3000 RPM in ambient. The wafers were subsequently rinsed with toluene for 2 minutes following various delay times. The thickness of the residual films remaining after exhaustive rinsing were measured by ellipsometry. The effects of several variations in the protocol were examined, including using solution concentrations of 1% and 10%, using distilled versus undistilled PACM, varying the UV ozone treatment time from 1 min to 60 min, varying the delay time between completion of UV-ozone treatment and depositing the solution from 0 minutes to a few minutes, and cleaning the substrate using piranha instead of UV-ozone. In all cases, no films were apparent visually on the substrate after rinsing with toluene. The film thicknesses after rinsing as measured by ellipsometry are shown in Figure 1-9. For delay times out to 60 minutes the residual films were all 30 Å or less, on the order of a few molecular layers. A few conditions led to the growth of thicker residual films at 120 minutes. However, on this time scale, significant curing (> 20%) occurs in the bulk, and thus this may simply indicate the progress of the bulk curing reaction. Thus, no evidence of accelerated kinetics or the buildup of a crosslinked interfacial layer was seen in these tests. This contrasts dramatically with the results for dip-coated samples, as described below.

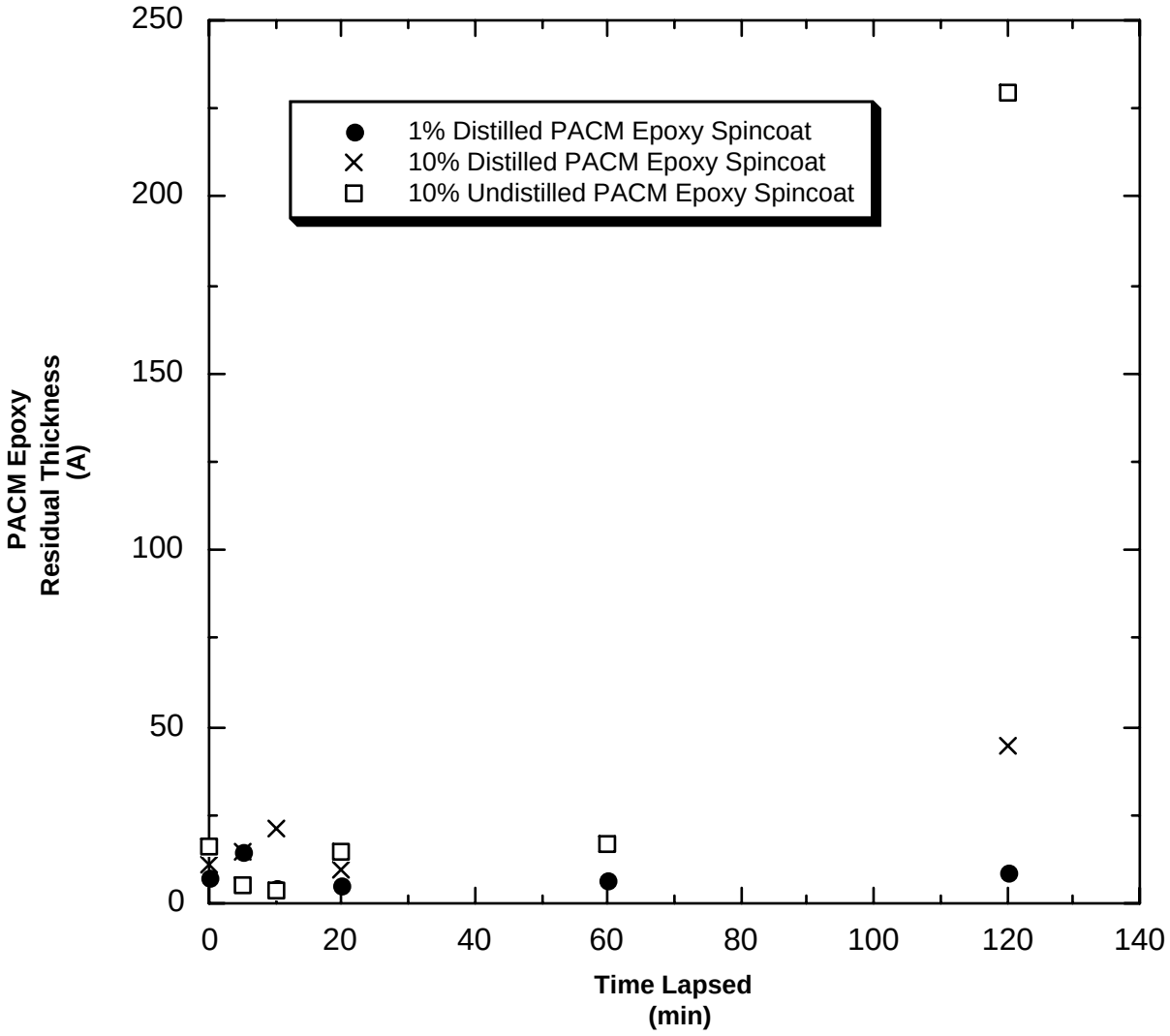

Figure 1-9. Thickness of PACM/RSL1462 residual film on silicon oxide as a function of delay time between spin-coating and rinsing with toluene.

Dip-Coating

Samples were coated with a dip-coating procedure in ambient and a simulated dip-coating procedure in both ambient conditions and in a glove box. The purpose of using the simulated dip-coating procedure was to conserve a limited amount of distilled PACM as we neared the end of this program.

The dip-coating procedure was as follows. Wafers were treated with UV-ozone for 20 minutes. The substrates were then dipped into a solution of the two components in

toluene in ambient and the excess was immediately shaken off. The samples with entrained films were left to stand for various delay times and then rinsed with toluene for 2 minutes. The thickness of the residual film as a function of the delay time prior to rinsing is given in Figure 1-10. Surprisingly, the thickness of this film builds up at the interface on a time scale that is faster than can be accounted for by the kinetics of the crosslinking reaction in bulk. For example, with only a 10 minute delay time, a film of 200 Å had built up at the surface whereas the kinetic data for the mixture in bulk (see Figure 1-3) indicates only about 2% cure in 10 minutes, which is insufficient to account for the formation of a gel layer. The gel point in bulk occurs at roughly 12.5 hrs. We note that the films for the dip-coated samples were very heterogeneous, and so the thickness values in Figure 1-10 are only an order of magnitude approximation. In particular, we do not believe that the thickness of the residual film decreases with delay time beyond 20 minutes. The observation of a thick crosslinked interfacial film for these conditions was a key result of this work and was repeated many times.

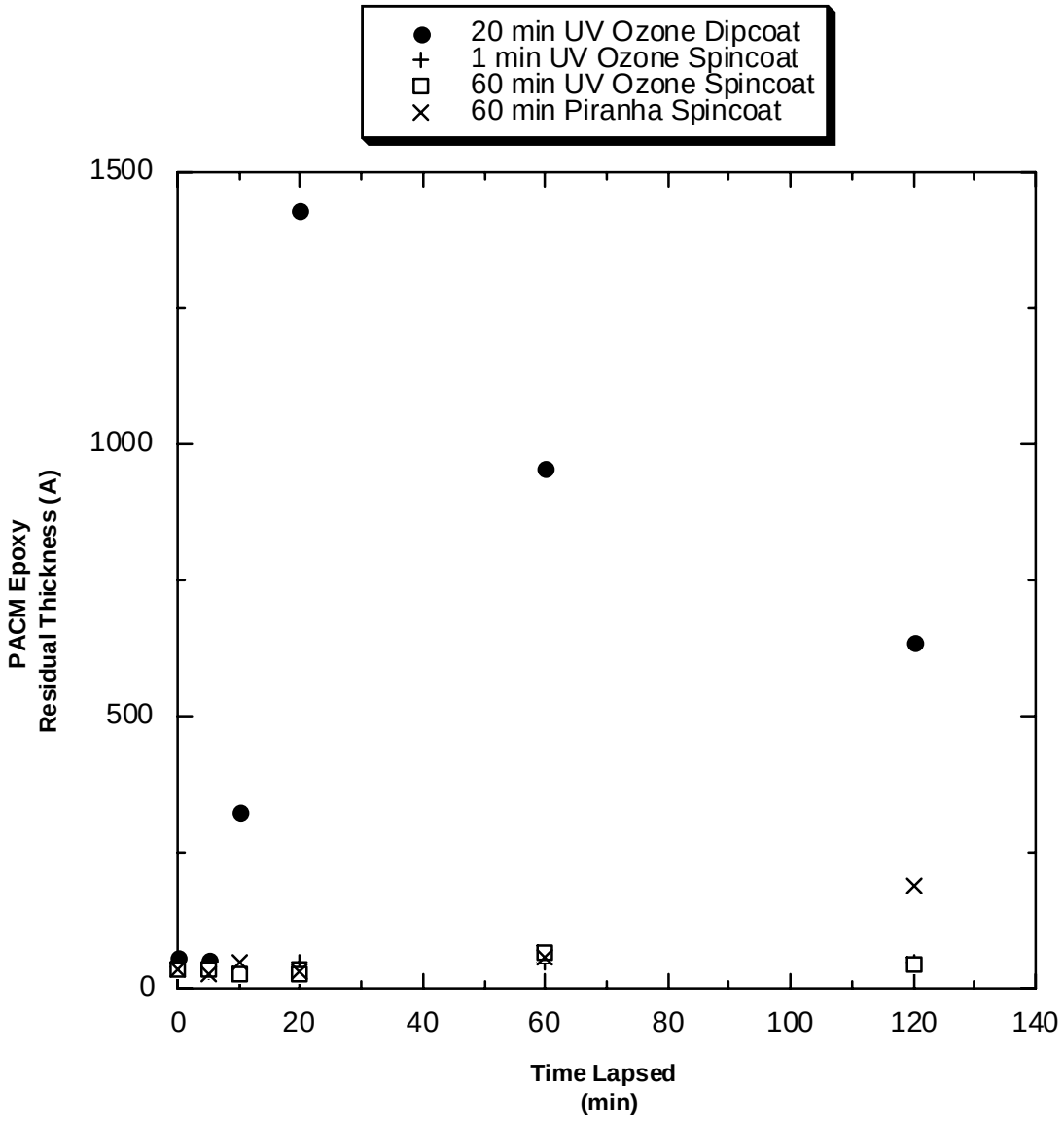

Figure 1-10. Thickness of PACM/RSL1462 residual film on silicon oxide as a function of delay time between spin or dip-coating and rinsing with toluene. The growth of a thick crosslinked interfacial film is much more pronounced for dip-coating than for spin-coating.

The simulated dip-coating procedure was performed both in a nitrogen-purged glove box and in ambient. The protocol was as follows. Wafers were treated with UV-ozone for 20 minutes. The samples were then transferred into a glove box, which constituted a delay time of ~ 10 minutes prior to coating. To be consistent, a delay time of 10 minutes was also used for the samples coated in ambient. Aliquots of 10% solutions in anhydrous toluene were pipetted onto the wafers until they were fully coated, and then the excess was immediately shaken off. The samples, having entrained films, were left to stand for delay times of 10, 30, 60, 90, and 120 minutes and then rinsed with toluene for 2 minutes.

Dramatically different results were obtained depending upon whether the samples were prepared in the glove box or in ambient. For the samples prepared in the glove box, no films were observed visually on the samples after rinsing. The thicknesses of the residual films measured by ellipsometry were < 5 Å and 18 Å for the 10 and 120 minute delay times, respectively. We also note that prior to rinsing, the films dewetted. This contrasts dramatically with experiments with PACM/RSL1462 outside the glove box for which dewetting was never observed.

For the samples in ambient, the films were stable prior to rinsing in all cases. Films were visually apparent on all samples after rinsing. A plot of thickness of the residual film versus delay time prior to rinsing is shown in Figure 1-11, where the thickness of the films after curing was determined using a Dektak profilometer.

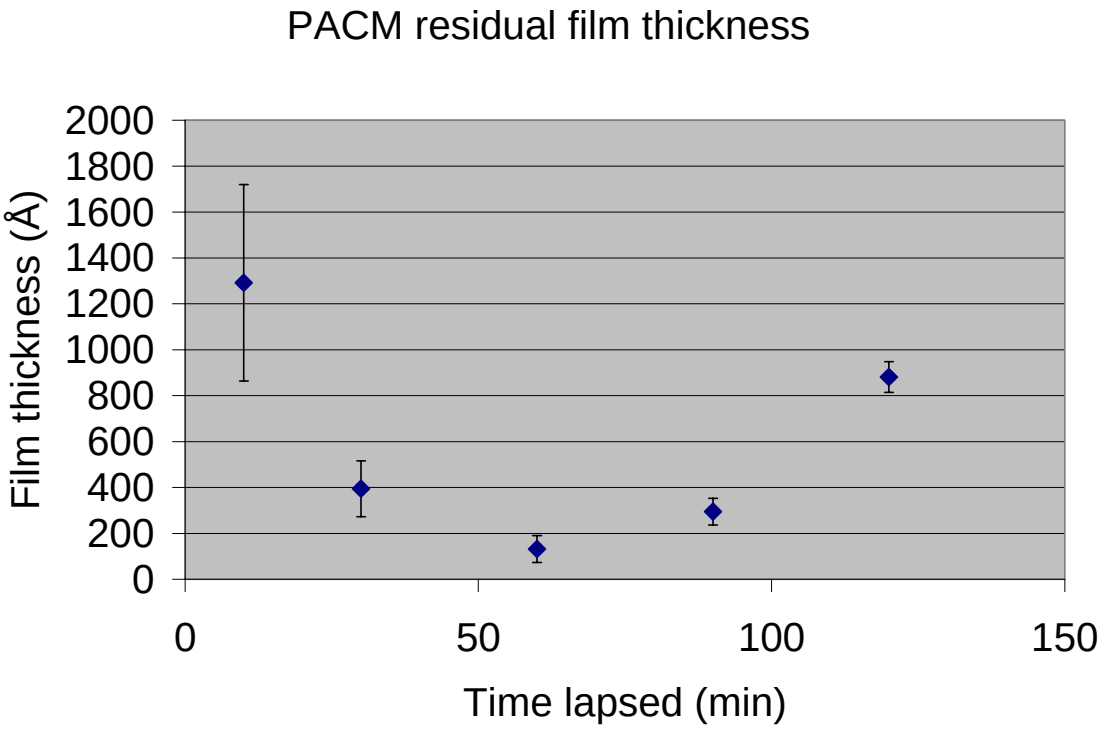

Figure 1-11. Residual film thickness of PACM/RSL1462 dip-coated films as a function of delay time between simulated dip-coating and rinsing with toluene. The error bars represent the 95% confidence interval for 6 measurements in various places on one sample.

Finally, one further experiment is worth noting. One set of samples was coated using the simulated dip-coating procedure described above in ambient conditions. However, after shaking off the excess the samples were covered with plastic or glass dishes until they were rinsed with toluene. The results, indicated in the table below, showed no growth of a thick interfacial film in contrast to uncovered samples in ambient where thick interfacial films were always observed.

Table 1-10. Interfacial film thickness of dip-coated samples that were covered prior to rinsing

Delay time before exhaustive rinsing	Thickness (Å)	Observations
10 min	11	nothing visible on wafers
60 min	32	nothing visible on wafers
120 min	5.5	nothing visible on wafers

Discussion:

This system was unique among the three examined in that it showed an extremely wide range of both wetting phenomena and interfacial reactivity as a function of the processing conditions.

Reactivity: These data provide evidence for more rapid cure kinetics at the interface than in bulk. In particular, a thick, partially cured interfacial film occurs for dip-coated films in ambient on a time scale for which little reaction occurs in the bulk. However, the growth of a thick interfacial film was not observed if the dip-coating was performed in a nitrogen-purged glove box, which clearly indicates that water vapor, O_2, or CO_2 plays a critical role in accelerating the kinetics. Water vapor is the likely accelerator, as accelerated cure kinetics in the presence of water vapor has been confirmed previously in studies of bulk epoxies [6]. This arises from the increased reactivity of a hydrogen-bonded transition state, in which a water molecule forms a hydrogen bond with the oxygen of the epoxide group. It seems unlikely that the accelerated kinetics could be due to a monolayer of water on the substrate surface because that should exist in all cases (both ambient and dry box) of this study. Indeed others have shown that rather extreme conditions are required to remove the monolayer of adsorbed water [7]. Therefore, we tentatively conclude that the accelerated cure is due instead to water vapor rapidly diffusing through the thin films after deposition and collecting at the substrate surface in ambient. Another possibility is that water was present in the solution and interacted with the resin molecules prior to dip-coating. Surprisingly, a thick partially cured interfacial film does not occur for spin-coated films in ambient. If water vapor does indeed accelerate the reaction, it is unclear why dip-coating versus spin-coating would make a difference. Spin-coating might possibly remove a thin layer of adsorbed water, or lead to some shear alignment of molecules at the interface, but we have no direct evidence of either of these phenomena. We also note that a thick, partially cured interfacial film was not observed for dip-coating in ambient when the samples were covered during the delay period prior to rinsing. This seems consistent with the above interpretation based on water vapor diffusing into the film, in that the flux of evaporating toluene may purge the enclosed volume above the sample of water vapor.

Dewetting: Dewetting of the mixture was never observed in ambient, regardless of application method (spin-coating or dip-coating). Dewetting was only observed for dip-coated exposed samples in a nitrogen-purged glove box. This suggests that water vapor diffuses through the film and stabilizes the film against dewetting. This contrasts with the T403/RSL1462 system, where dewetting of the mixture on silicon oxide was observed

both in dry conditions and in ambient. Finally, we note that when a cover was used over the sample in the glove box, no dewetting was observed. The stabilization observed with a cover in the glove box must be due to a mechanism unrelated to the presence of water vapor.

1.4 Studies involving Shell RSL1462 and TETA

To enhance our understanding of the apparent acceleration of the curing reaction at the interface, as discussed in Section 1.3, we chose to study another system that cures even more rapidly at room temperature, RSL1462 with TETA (triethyl triamine) crosslinker. The structure of TETA is shown in Figure 1-1.

Kinetics of the crosslinking reaction in bulk. The extent of cure as a function of time at ambient temperature was obtained using FTIR and dynamic viscosity. Details of these procedures and results are given in Section 1.2.1.

For this system, measurements were made both in an atmosphere of dry nitrogen and also in air. The gel time in dry nitrogen is indicated by an arrow in Figure 1-3. Again, reasonable agreement was obtained with the cure kinetics obtained by FTIR. However, we note that the RSL1462/TETA system gels at lower conversion than for the RSL1462/PACM system. That is expected based on the greater functionality of TETA (6 reactive protons) than for PACM (4 reactive protons). We also note that the gel time in ambient conditions (4.17 hrs) was reduced (faster cure) relative to the gel time in dry nitrogen (5.05 hr). Furthermore, visual inspection of the samples cured in ambient provided evidence that the exposed edges cure faster than the center. These observations demonstrate that a component in the air at ambient, likely water vapor, accelerates the cure reaction, and supports the explanation of accelerated cure at the interface of PACM/RSL1462 samples in ambient.

1.4.1 Wetting/dewetting studies and the growth of crosslinked interfacial films

Studies were performed mainly on silicon with its native oxide. A few were performed on gold-coated silicon wafers. Films were prepared by spin-coating as well as by a simulated dip-coating procedure.

Spin-coating

The spin-coating protocol was as follows. Wafers were treated with UV-ozone for 30 minutes. Solutions of the two components (10 wt % in toluene) were deposited onto the wafers and then left to sit for 1 minute. The wafers were then spun at 3000 RPM. The wafers were subsequently rinsed with toluene for 2 minutes following delay times of 0, 1, 5, 10, 20, and 60 min. All samples including the sample with no delay time before rinsing showed a very thick, visually-apparent film after rinsing. The results were qualitatively the same with DETA (diethyl triamine).

This was repeated in a side-by-side comparison between silicon oxide and gold substrates. The samples were rinsed with toluene immediately. For the silicon oxide surface, thick films resulted which displayed various colors. For the gold surface, very

thick films resulted which were sufficiently rough that no colors were evident. The experiment was repeated with a 2% solution and similar results were obtained.

Regarding TETA by itself, with the same protocol but no rinsing, TETA alone formed smooth films on silicon oxide but a heterogeneous film with big droplets on gold. We did not look for the presence of a residual film. The origin of this difference is unclear. The result on gold could be due to pseudo partial dewetting (minimum in the effective interface potential) or to true dewetting ($S < 0$). We would expect stronger short-ranged interactions between the amine groups and silicon oxide than between the amine groups and gold.

Simulated Dip-coating

Samples were coated with a simulated dip-coating procedure both in a nitrogen-purged glove box and in ambient. The protocol was the same as that described in Section 1.3.2 for the PACM/RSL1462 system. The samples were left to stand for delay times of 10, 30, 60, 90, and 120 minutes and then were rinsed with toluene for 2 minutes.

As with the PACM/RSL1462 samples, no dewetting occurred in ambient prior to rinsing. For the samples in ambient, thick visually-apparent films were observed for all delay times. The film thickness was determined using a Dektak profilometer, giving an average film thickness of 1700 ± 700 Å for the sample with a 60 minute delay time. The other samples were too soft to measure using the Dektak. This was repeated for samples cleaned using piranha rather than UV-ozone. The results were qualitatively the same.

In contrast, for the samples in the glove box, no visually observable films remained on the samples. The thicknesses of the residual films measured by ellipsometry were 8 Å and 16 Å for the 10 and 120 minute delay times, respectively. The absence of a thick interfacial film in this case is one of the most dramatic results of this study, and contrasts sharply with all observations for this system in ambient conditions where thick interfacial films were observed even with no delay time prior to rinsing. This is further strong evidence that water vapor accelerates the amine-epoxide cure reaction at the interface. We also note that prior to rinsing, the films were stable – no dewetting was observed. This contrasts with the other two systems, where dewetting of the mixtures on silicon oxide was observed in the glove box.

Discussion: The buildup of a thick residual film of TETA/RSL1462 is even more dramatic than for PACM/RSL1462. As for the PACM/RSL1462 system, it does not appear to be due to a monolayer of adsorbed water because that should exist in all cases (both ambient and dry box) of this study. In addition, such a layer of adsorbed water is unlikely to be present on a gold surface, at least not to the extent as on silicon oxide, yet the thick residual film is observed on both silicon oxide and gold in ambient. Again, we propose that water vapor rapidly diffuses through the thin films after deposition in ambient or is present in solution, and collects at the substrate surface. We have as yet no direct evidence of an excess concentration of water within the film. An excess of water might be detectable with neutron reflection.

1.5 Summary

The three systems varied dramatically in both wetting properties and in accelerated interfacial reactivity. For the T403/RSL1462 system, the dominant finding was a dewetting mechanism for films on silicon oxide under all conditions. No accelerated interfacial reactivity was observed. For the PACM/RSL1462 system, both dewetting and interfacial reactivity were strongly dependent upon the processing conditions. For the TETA/RSL1462 system, accelerated interfacial reactivity dominated the behavior in ambient, but was entirely absent in dry conditions.

We have learned that low levels of water vapor affect both wetting/dewetting and the presence of an accelerated reaction kinetics at the interface. Regarding the latter, it is not clear why the interfacial region is more strongly affected relative to the bulk of the film, but this was clearly evident for the PACM/RSL1462, TETA/ RSL1462, and DETA/RSL1462 systems. We propose that water vapor rapidly diffuses through the thin films after deposition or is present in the coating solution in ambient, and collects at the substrate surface. The fact that no effect was seen for the T403/RSL1462 system is likely due to the fact that dewetting occurs more rapidly than the accelerated cure reaction in that case. The curing reaction is much slower for T403 than for the other systems. The results of this study, and the understanding described above, will have substantial practical impact in guiding the selection of adhesive materials that will not be susceptible to dewetting. Simply choosing a system for which the accelerated cure kinetics at the interface are sufficiently fast can eliminate dewetting entirely. This appears to occur independent of the substrate material. This mechanism can be rapidly verified by spin-coating or dip-coating and then rinsing with toluene. The presence of a macroscopic film that is not removed with exhaustive rinsing indicates accelerated cure kinetics near the interface.

While much insight has been gained into these complex systems, some important questions remain.

1. Although the early observation of dwetting of T403/RSL1462 on silicon oxide inspired much of the work of this study, we still do not have definitive proof of the dewetting mechanism. The matrix of bulk films spun onto the various residual films demonstrates that preferential segregation of the crosslinker could drive dewetting. However, no direct support for preferential adsorption of the T403 to the silicon oxide surface was found. Strong A-B interactions could provide a driving force for decreasing the surface area to volume ratio. The impact of strong A-B interactions on the effective interface potential has not been worked out. However, from this reasoning it is not clear why dramatically different results should occur on different substrates, as shown in Table 1-2.

2. We do not understand why the presence of water vapor should accelerate the reaction kinetics preferentially near the interface, as was observed for the cases of PACM, TETA, and DETA mixed with RSL1462.

3. We do not understand why, in the absence of accelerated reaction kinetics, water vapor stabilizes the PACM/RSL1462 films in ambient but not the T403/RSL1462

systems. No dewetting of PACM/RSL1462 was observed in ambient even when a thick interfacial crosslinked film did not form.

4. We do not understand why dip-coated films of the PACM/RSL1462 mixture dewet in dry conditions. Is that due to strong A-B interactions or preferential adsorption of the PACM to the silicon oxide surface? Would dip-coated films of T403/RSL1462 dewet in dry conditions as well?

5. We do not understand why films of RSL1462 on 2000 Å silicon oxide are stable when the effective interface potential calculation predicts instability, as for PS. Perhaps the presence of more complex interactions need to be included in the effective interface potential. We recommend a follow on study involving other comparisons between molecules that have similar refractive index but very different chemical functionality.

2 Fluid dispensing

In the fabrication of micro- and nano-scale devices, the need exists to accurately and reproducibly dispense small volumes (<1 nL) of viscous materials such as adhesives. Here, several methods of dispensing small quantities of adhesives are discussed.

2.1 Fluid dispensing model

Four dispensers were tested for their suitability in applying adhesives. From these options, the Picospritzer by Stoelting appeared to give the best results. The Picospritzer gives a millisecond (ms) duration pressure pulse through a tube to the headspace above a liquid column in a capillary (see Figure 2-1). The pulse does not dislodge a droplet from the tube, but it causes the meniscus to bulge far enough from the capillary opening to be wicked onto the surface.

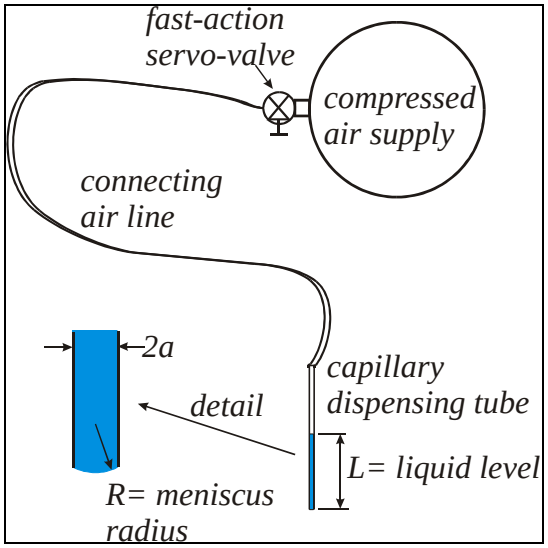

Figure 2-1. Geometry used to develop governing equations for the Picospritzer system.

A model of the system was developed to show the interplay between parameters such as the column diameter and length, fluid properties, and the pulse duration. The pressure pulse causes the liquid column to accelerate in the capillary and increase the volume of liquid in the capillary. Inertial forces, frictional forces, and tension forces in the meniscus oppose the pressure force. If it is assumed that the frictional pressure drop in the capillary is described by Hagen-Poiseuille relation, then the governing equation for the meniscus volume is given by,

$$\frac{L\rho}{\pi a^2}\frac{dV}{dt^2}+\frac{8\mu L}{\pi a^4}\frac{dV}{dt}+\frac{2\sigma}{R\{V\}}=P_H \qquad \textbf{Equation 2-1}$$

where V is the volume of the liquid in the meniscus, P_H is the pressure pulse magnitude, and ρ, μ, and σ are respectively the density, viscosity, and surface tension of the dispensed liquid. R is the radius of the meniscus and it is related to V through the geometric relation,

$$V = \frac{\pi}{3}\left(2R + \sqrt{R^2 - a^2}\right)\left(R - \sqrt{R^2 - a^2}\right)^2. \qquad \textbf{Equation 2-2}$$

The expression for the volume growth of the meniscus was solved numerically, and a typical result is shown in Figure 2-2. Gravity gives the meniscus an initial volume of about 130 picoliters (1.3 x 10^{-13} m^3), and a 1380 Pa (0.2 psi) pulse will double the volume to 260 picoliters in about 8 ms. At that point, the meniscus will extend 50 μm from the capillary tube and contact the application surface where it is to be deposited.

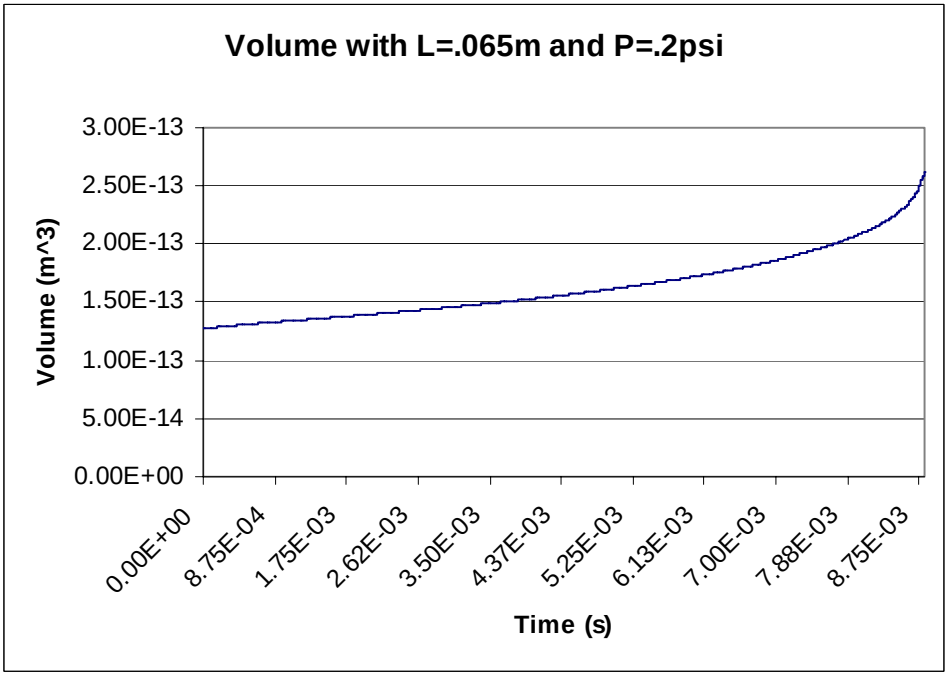

Figure 2-2. Growth of fluid in meniscus as a function of time for an initial fluid column length of 65 mm, a capillary tube radius of 50 μm, and a pressure step increase of 1380 Pa (0.2 psi).

Parametric studies have been performed with the model, and experiments are being designed for verification. It has been observed that the model predicts much lower drive pressures than we are currently using for a given pulse duration. Originally, it was believed that compressibility and frictional effects in the air hose connecting the pulse valve with the dispenser were attenuating the pressure pulse. Based on work by Ducoffe [8], however, it appears that the headspace above the dispense column should reach about 80% of the reservoir pressure in about 2 ms. This makes it appear unlikely that the pressure pulse is being attenuated in the air hose. Compliance in the tubing that connects the pressure valve and the dispenser tube is likely contributing to a reduction in the pressure.

2.2 Spray deposition of polymers

A picospritzer is effective in applying both polymer coatings and adhesives that are suspended in solvents. The minimum dispensed volume is typically on the order of 100

picoliters and, with a 1% solution of polymer in solvent, approximately 1-ng of polymer will be dispensed per drop. While the picospritzer worked well for hand dispensing, efforts to automate the process were largely unsuccessful. Solvents would evaporate away from the meniscus while the tip was translating and the characteristics of the solution would be altered. Cooling the dispenser tip and operating in a saturated environment did help, but still did not provide consistent results.

Spray-coating was explored as an alternative to drop coating polymers. Solutions were aerosolized using a nebulizer manufactured by Burgener Research of Mississauga, Ontario, Canada. The nebulizer provides a solvent flow of 0.005 to 2.0 ml/min and produces a droplet size of approximately 30-70 microns. A schematic of the spray system is shown in Figure 2-3. Liquid is fed into the nebulizer through a syringe pump and it is atomized at the tip of the nebulizer by a parallel flow of nitrogen gas. The spray pattern from the nebulizer has an 8 degree half-cone angle.

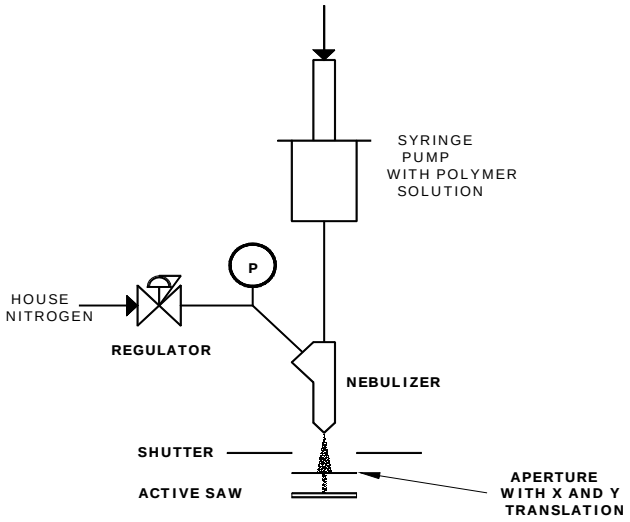

Figure 2-3. Micron-droplet spray system.

An aperture is situated slightly above the target surface to mask-off areas that are not to be sprayed. Shadow masks were fabricated by ultrasonically machining 200-µm by 600-µm slots in a 1500-µm thick Pyrex slide. Figure 2-4 shows that there is a slight taper in the mask from the entrance to the exit. Thinner masks (500-µm thick) exhibited less taper, but it was found that the thicker masks produced a better-defined spray pattern. Bullen Ultrasonics of Eaton, Ohio produced the shadow masks.

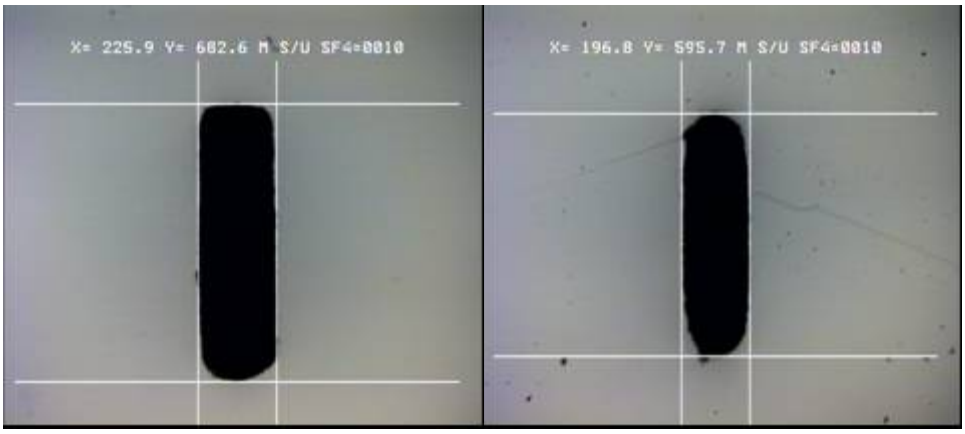

Figure 2-4. Pyrex shadow mask. Top shown in left figure, bottom shown in right figure.

The quartz surface of a surface acoustic wave (SAW) sensor was used as the target for our coating studies. SAW transducer lines launch a compression wave across the quartz surface, and a second set of transducers sense the surface wave. Basically, the SAW acts as a tiny scale that senses how well mass covers and adheres to the quartz.

The pattern of the coating on the surface is a function of several variables:

- Air flow rate
- Spray time
- Solution flow rate
- Polymer concentration in the solution
- Nebulizer height above SAW
- Nebulizer position over the aperture
- Aperture thickness
- Aperture dimensions
- Aperture exit distance above SAW

We did not perform an extensive study of these parameters, but with some minor iteration it was found that a fairly well defined pattern could be achieved by spraying. In general it was found that better pattern definition was achieved with a thicker mask that is closer to the quartz surface, and with the nebulizer properly aligned and 2 inches above the mask. Figure 2-5 shows the deposited pattern between the wave-launch and pick-up lines on the quartz. A mass of approximately 8 ng of material was deposited on the quartz. Assuming uniform deposition, the coating was on the order of 30-nm thick.

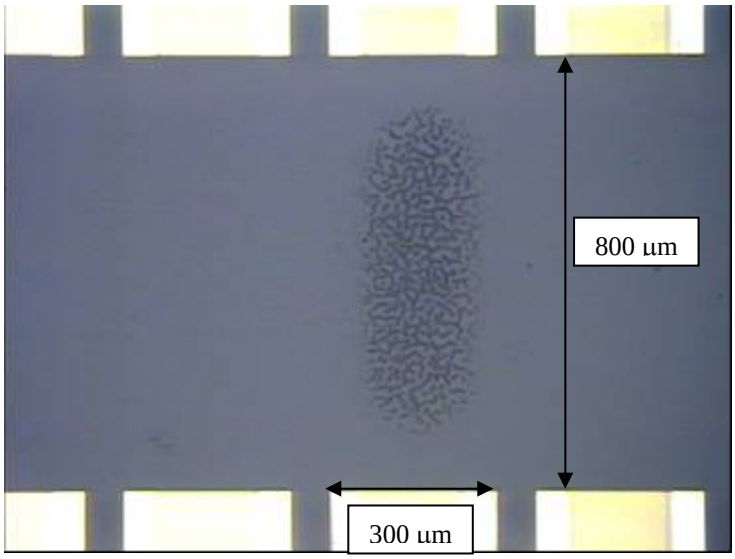

Figure 2-5. Spray pattern on the quartz surface of a surface acoustic wave (SAW) sensor.

While the spray pattern was well defined, the distribution of the mass on the surface was not always optimal. As Figure 2-6 illustrates, dewetting of the film was a major problem. Spray-deposited films exhibit dewetting behavior to a greater extent than do spin-coated films. Polymer on quartz is a metastable system and, without proper surface preparation, liquid tends to bead up on the surface. Dewetting was mitigated by aggressive cleaning in a hot Piranha solution (3 parts H_2SO_4, CAS# 7664-93-9, and 1 part H_2O_2, CAS#7722-84-1 at 100°C), but Piranha cleaning the surface was not effective for all coatings, and it is not suitable for many micro assemblies.

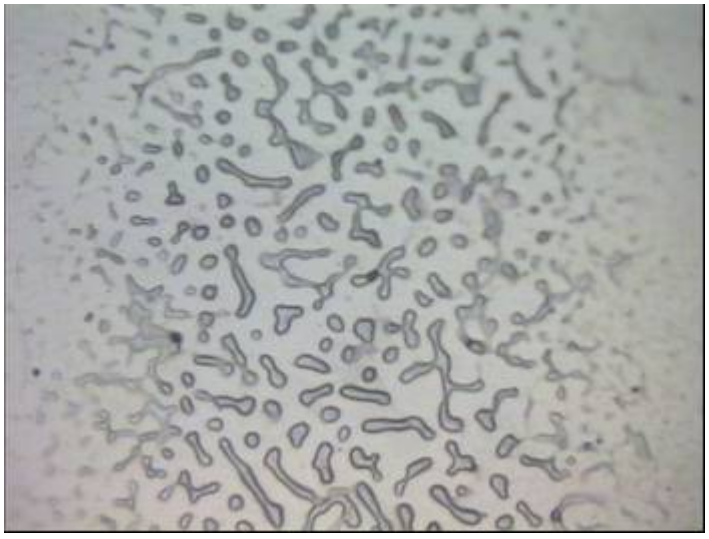

Figure 2-6. PECH polymer sprayed in a 0.0625 mg/ml solution of 5% toluene and balance chloroform.

Some of the best results were achieved by mixing Fullerines (C_{60}) and a dispersant (Spruso, manufactured by OMG Americas Inc.) with the polymer solution. Figure 2-7 illustrates the coating that was achieved with a 0.0625 mg/ml solution of polyepichlorohydrin (PECH) polymer in chloroform with 0.05% Spruso and 0.00625 mg/ml of C_{60}. The addition of C_{60} to polymers to prevent dewetting is discussed in greater detail in Section 3. Some discontinuities are still present, but coverage of the surface is much better. This improved coverage is also apparent in the output signal of the SAW. Figure 2-8 shows that when wetting is good between the polymer and the quartz surface, the SAW response gradually increases as mass is added to the surface. Also shown is the response when wetting is poor. In this case, mass was added in a stepwise fashion. After about 5 steps, the polymer began to collect in small islands and additional coating steps had little impact on the SAW response.

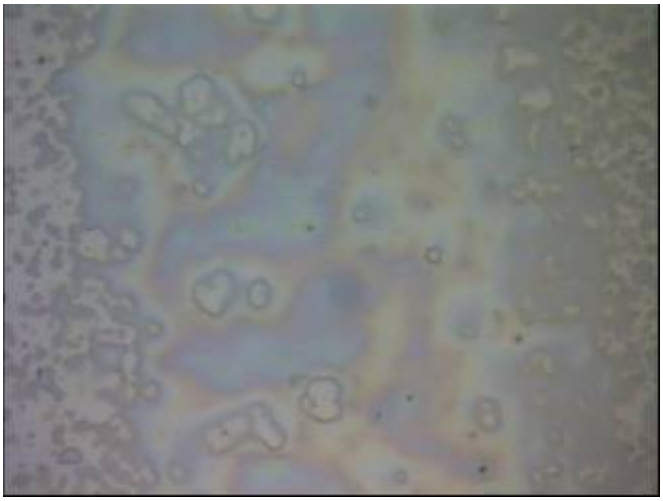

Figure 2-7. Quartz coated with PECH in chloroform solution with 0.05% Spruso and 0.00625 mg/ml C_{60}.

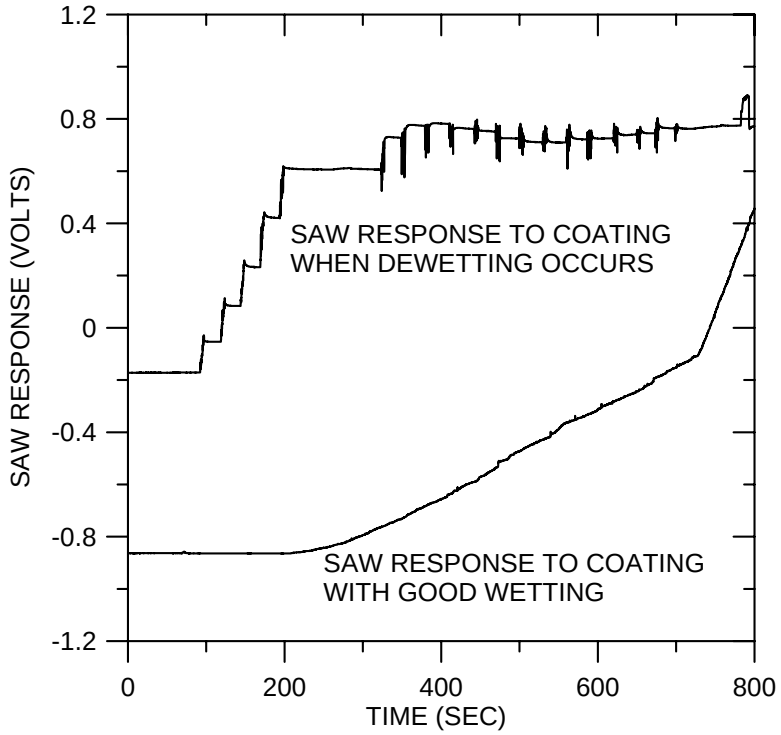

Figure 2-8. SAW response as coating dewets from surface. Also shown is the response when wetting is good.

2.3 Measuring deposited mass

The SAW gives an indication of the deposited mass, but this measurement is strongly influenced by surface adhesion. Without intimate surface contact on the quartz the added mass of the polymer will not couple well with the surface wave, and the measurement will be in error. Another type of resonator was developed under a separate program, and this new resonator proved to be well suited for measuring nanogram levels of added mass.

A sketch of this new resonator is shown in Figure 2-9 along with an array of the fabricated devices. The small paddle pivots about the tabs on either end. A magnetic field in the plane of the paddle will impose a normal force on the paddle when current runs through the conductor lines. At the appropriate frequency, an alternating current will cause the paddle to resonate. The resonant frequency in Hz is given by the expression,

$$\omega_n = \frac{1}{2\pi}\sqrt{\frac{24\,\beta\,b\,c^2 G}{\left(M_c + \rho\,w\,a\,L\right)\left(c^2 + L^2\right)}}, \qquad \textbf{Equation 2-3}$$

where

w = width of paddle = 1500 µm
L = length of paddle = 600 µm
a = length of pivot arm = 202 µm
b = width of pivot arm = 157.8 µm

c = thickness of paddle and pivot arm = 8µm
G =shear modulus of elasticity =$E/[2(1+\nu)]$ = 165 GPa /[2(1+0.28)] = 64.5 GPa
ρ = density = 2910 kg/m^3
B = magnetic flux = 0.18 T
ω_n = resonant frequency
and it is assumed the coating mass, M_c, is roughly uniform across the paddle.

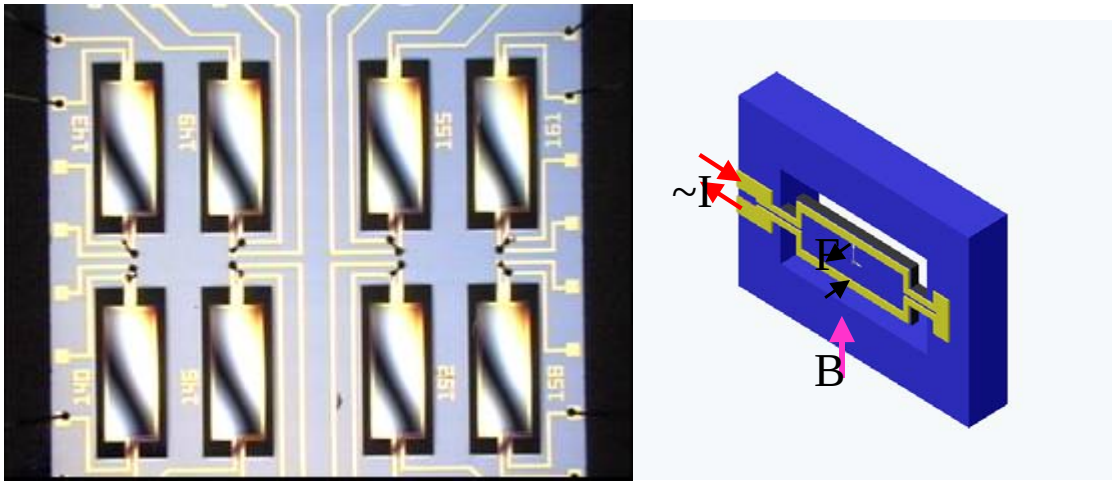

Figure 2-9. New resonator used for mass measurement. Fabricated array (left) and descriptive sketch (right).

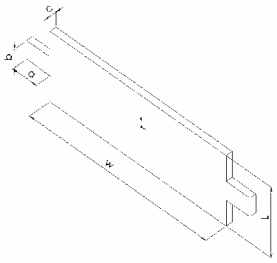

w = width of paddle = 1500 µm
L = length of paddle = 600 µm
a = length of pivot arm = 202 µm
b = width of pivot arm = 157.8 µm
c = thickness of paddle and pivot arm = 8µm

Figure 2-10. Geometry of the resonator paddle.

As coating is added to the surface of the paddle, the resonant frequency drops and the added mass can be determined using Equation 2-3. A typical result for a drop coating application is illustrated in Figure 2-11. After 15 drops of a polymer solution is deposited on the surface with a Picospritzer, the resonant frequency drops by 17 Hz. This shift corresponds to about 41 ng of added mass according to the above equation, so each drop contained roughly 2.7 ng of polymer. This resonator can easily be used to measure deposited masses from other spray- and drop-coating techniques.

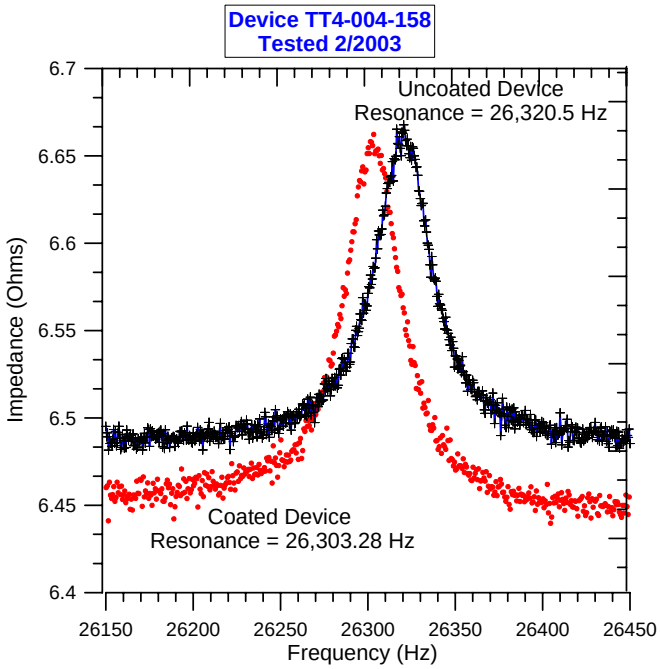

Figure 2-11. Resonance shift caused by 15 drops of a polymer coating applied by the Picospritzer. At resonance, the impedance reaches a maximum.

3 Inhibiting dewetting of thin polymer films

3.1 Introduction

Thin polymeric films find use in many technologies such as dielectric insulators, diffusion barriers, sensors, [9] fuel cells, support media and most recently the IBM Millipede [10] to name a few. During their manufacture, by spin or dip coating processes, for example, films are prepared having a kinetically trapped structure or morphology under highly non-equilibrium conditions. If the polymer glass transition temperature is below the device operating temperature, thermodynamic equilibrium will eventually be achieved. This may result in dewetting of the film from the substrate. Chemical or physical modification of the substrate or polymer can induce wetting, even under non-equilibrium conditions, to create a desirable film and is frequently performed.

Fabrication of surface acoustic wave (SAW) sensors [11] demands a given polymer be used without chemical modification or physical treatment, such as crosslinking, to retard dewetting. In addition, substrate surface treatment may not be possible due to the given manufacturing process. Thus, a robust process is required for a tractable SAW sensor and its manufacture.

We have discovered that nanoparticles such as dendrimers [12] and most recently polystyrene nanoparticles [13] retard dewetting to produce stable films. This technology allows simple manufacture of stable films because the nanoparticle is soluble in the coating solvent. Further, neither the coating process nor the substrate need be modified.

The specific case that is currently being studied is the elimination of dewetting of the polymer films used in the μ-ChemLab. The polymers used in this chemical sensor, including PECH and BSP3, all have glass transition temperatures well below room temperature, which is the temperature at which the sensors are operated. Because of this, the films are mobile and tend to dewet when exposed to a saturated vapor such as DMMP or methanol. This leads to degradation of sensor performance. However, current techniques for elimination of dewetting, such as surface treatment and modification or crosslinking of the polymer, are not possible due to potential complications with the absorption sensitivity of the film. Thus, a robust process is required for manufacture of the μ-ChemLab.

3.2 Experimental

Polyepichlorohydrin (PECH) was obtained from Aldrich and used as received. BSP3 was prepared as given in ref. [14]. The structures of PECH and BSP3 are shown in Figure 3-1.

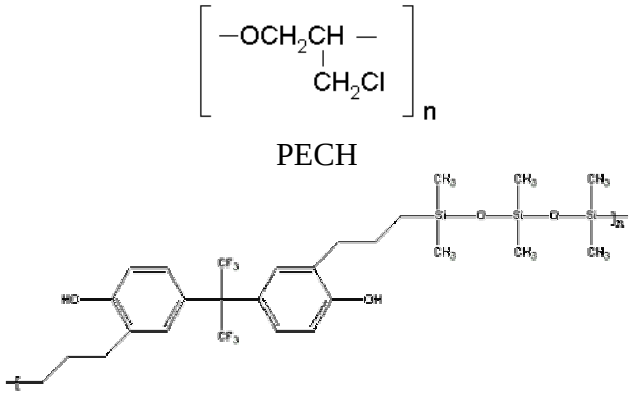

Figure 3-1. Chemical structures of PECH and BSP3.

In the studies, PECH and BSP3 were dissolved in a solvent and then spin-coated onto silicon wafers at 5000 rpm for 40 seconds to produce thin films less than 50 nm in thickness. After spin-coating, the wafers were placed in a saturated methanol vapor environment to activate dewetting. For the studies where fullerenes were used, a concentration of 1% by mass with respect to the polymer was used. The fullerenes were added to the polymer/solvent solution and then spin-coating was carried out as previously described.

3.3 Results and Discussion

Here, we show that the addition of fullerenes [15] (C_{60}) to both PECH and BSP3 inhibits dewetting of thin polymer films. In Figure 3-2, a 36 nm film of PECH is observed after exposure to methanol for various times to show that dewetting readily occurs.

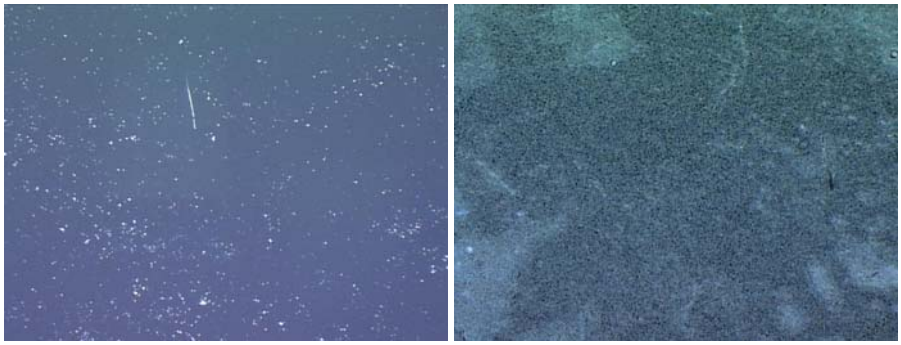

a) immediately after spin-coating b) after 45 minutes

c) after 20 hours

Figure 3-2. Progress of dewetting of a 36 nm PECH film over time: a) immediately after spin-coating, b) after 45 minutes, c) after 20 hours of exposure to saturated methanol vapor.

In Figure 3-3, fullerenes were added to the same solution of PECH as above and then spin-coated. It can be seen that the addition of the fullerenes inhibits dewetting as no holes are formed even after 17 hours of exposure to methanol vapor.

a) immediately after spin-coating b) after 17 hours

Figure 3-3. Elimination of dewetting of a 36 nm PECH film with addition of fullerenes: a) immediately after spin-coating, b) after 17 hours of exposure to saturated methanol vapor.

In Figure 3-4, a BSP3 film is shown. It appears as though BSP3 dewets much more rapidly and extensively than PECH, as the final stage of dewetting is reached after only 45 minutes of methanol exposure.

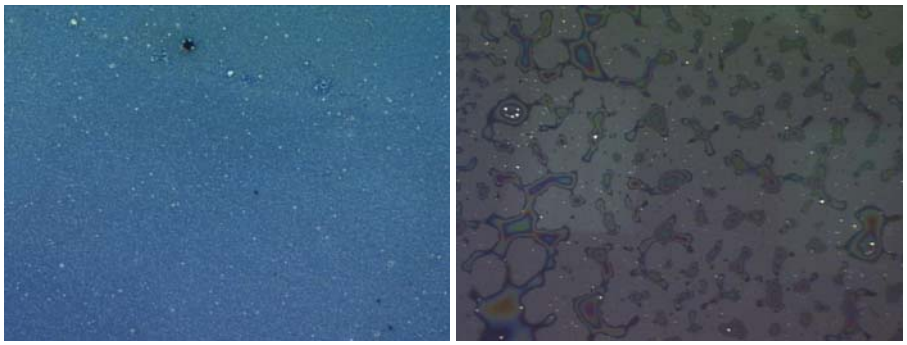

a) immediately after spin-coating b) after 45 minutes

Figure 3-4. Dewetting of a BSP3 film: a) immediately after spin-coating, b) after 45 minutes of exposure to saturated methanol vapor.

Again, it is shown in Figure 3-5 that the addition of fullerenes inhibits dewetting. Here, fullerenes were added to the same BSP3 solution as above and then spin-coated. Even after 1 week of methanol exposure, the film is still stable.

a) immediately after spin-coating b) after 45 minutes

c) after 1 week

Figure 3-5. Elimination of dewetting of a BSP3 film with addition of fullerenes: a) immediately after spin-coating, b) after 45 minutes, c) after 1 week of exposure to saturated methanol vapor.

3.4 Conclusions

Addition of nanoparticles to these two very different systems completely eliminates dewetting. It is likely that our observation is a general phenomenon that can be applied to

many polymer systems. Currently, we do not have physical evidence of a mechanism of the effect. Ongoing research is planned to address this.

3.5 Future Work

We plan to continue studying the addition of nanoparticles to the polymers used in the µ-ChemLab. In addition to the fullerenes currently being used, other nanoparticles, such as silica nanoparticles and crosslinked polystyrene nanoparticles, will be studied as well. Specifically, we plan to focus on the surface tension, surface energy, thermal properties, and wetting characteristics of the blends to gain a better understanding and explanation of this phenomenon of suppression of dewetting. In addition, we plan to implement this method of dewetting suppression into the manufacture of the µ-ChemLab.

3.6 Computational modeling

The efforts to date to model mixtures of dilute nanoparticles in polymer melts near a surface, with application to the stabilization of the polymer film by the nanoparticles, are summarized here. The technique used is classical density functional theory (DFT) as described in Frischknecht et al. [16] In its current implementation, this theory makes several assumptions. The first is that the polymers are freely-jointed chains consisting of N tangent spheres of radius σ, shown in Figure 3-6, so that their radius of gyration is given by

$$R_g^2 = N\sigma^2/6 \qquad \textbf{Equation 3-1}$$

This is a good assumption for polymer melts. Second, the DFT is a mean-field theory. As input, it currently assumes that the effective monomer-monomer interactions are given by the repulsive "direct correlation functions" $c(r)$ calculated from the polymer reference interaction site model (PRISM) theory, plus an attractive Lennard-Jones type potential which is added as a perturbation. PRISM theory has been shown to be quite accurate in calculating the properties of repulsive polymer melts. [17] The DFT calculations are done in the grand canonical ensemble, i.e. an open system. This means that the chemical potential of the system is fixed rather than the number of molecules. For liquids near a surface, the chemical potential is essentially fixed by the bulk density of the liquid far from the surface. We should thus think of the liquid near the surface as being in equilibrium with a bulk liquid far away from the surface. In the DFT, the bulk liquid is taken to have a free energy of $\Omega = 0$.

Figure 3-6. Coarse-grained model of polymer and particles.

For this initial work, a system of PS nanoparticles in a PS melt was considered. The questions are: how many sites N do we need, and what does σ correspond to in real units? There is no unique way to fit a real polymer into the coarse-grain model of Figure 3-6. One option is to assume that N is the actual degree of polymerization of the polymer, i.e. each sphere represents a monomer. Then σ is determined by equating the radius of gyration of the model polymer with the real one of interest. This can be done generally. From Fetters et al., [18] for PS melts at 413 K the radius of gyration is given by

$$R_g^2/6M = 0.0723 \text{ Å}^2 \text{ mol/g} \qquad \textbf{Equation 3-2}$$

where M is the molecular weight. The degree of polymerization $N = M/m_o$ where $m_o = 102$ is the molecular weight of the monomer, so equating the two expressions for R_g^2 we find $\sigma = 6.65$ Å. Alternatively, one could ask on what length scale PS is a Gaussian chain, i.e. what is its thermal persistence length? Recent work by Brulet et al. [19] suggests that the persistence length is about 9.2 Å, somewhat larger than an effective monomer diameter. If we increase σ to 9.2 Å, then we must decrease N to keep R_g^2 constant.

The advantage to considering PS nanoparticles in a PS melt is that one might expect the only important interactions to be the entropic ones, so that we can use a purely athermal (repulsive) model system. As a sample calculation, consider a chain with $N = 20$ sites of diameter $\sigma = 6.65$ Å (using $N = M/m_o$, this corresponds to PS with molecular weight 2040, a fairly short chain but about the same length as those used by Barnes et al. [20]), and nanoparticles with diameter 1.5 $\sigma \approx 10$ Å, i.e. 1 nm. We also need to specify a density. Typical monomer densities for polymer melts are on the order of $\rho = 0.85\ \sigma^3$, so we use that value here for the polymer melts. A nanoparticle density of approximately 5% by weight then corresponds to a nanoparticle number density of approximately 0.011 σ^3.

We take the interactions to be of the repulsive Lennard-Jones form:

$$U(r) = \begin{cases} \frac{4\varepsilon_{ij}}{k_B T}\left[\left(\frac{\sigma_{ij}}{r}\right)^{12} - \left(\frac{\sigma_{ij}}{r}\right)^{6}\right], r < r_c \\ 0, \qquad\qquad\qquad\quad r > r_c \end{cases} \qquad \textbf{Equation 3-3}$$

where r is the separation between species, T is temperature, k_B is Boltzmann's constant, and we take $\varepsilon_{ij}/k_B T = 1$ for all species so that the interactions are all the same strength, essentially hard-core like interactions. The monomer diameter $\sigma_{pp} = 1$, the nanoparticle diameter $\sigma_{nn} = 1.5$, and the cross-term for the monomer-nanoparticle interaction is $\sigma_{pn} = 1.25$. The cut-off distance is simply given by the location of the minimum of the Lennard-Jones potential, $r_c = 2^{1/6}$, so the interactions are purely repulsive. We measure all energies in units of $\varepsilon/k_B T = 1$, and all lengths in units of σ.

Next we need to specify the interactions with the substrate. We have some options here. First we can take the substrate to just be a hard surface, with potential

$$V(z) = \begin{cases} \infty, z < 0 \\ 0, z > 0 \end{cases} \qquad \textbf{Equation 3-4}$$

where z is the distance between the particles and the surface, located at $z = 0$. In that case, we get the profiles shown in Figure 3-7. We see that the particles preferentially go to the surface and displace the polymer. The surface free energies are $\Omega_s = -2.15\ kT$ for the homopolymer and $\Omega_s = -4.98\ kT$ for the mixture, so the surface free energy is lower when the nanoparticles are added. This shows that even with purely entropic interactions, the nanoparticles can lower the surface tension of a polymer melt. However, we note that since the surface energies are negative, the polymer mixture is wetting the surface.

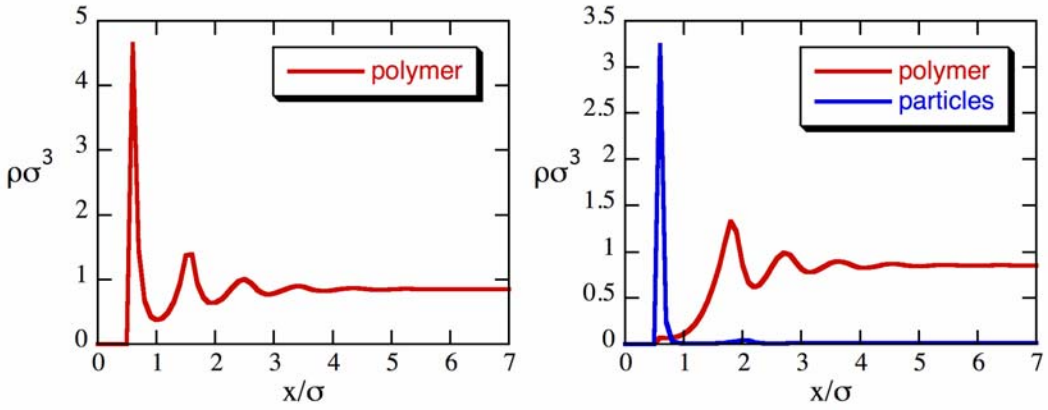

Figure 3-7. A polymer film and a polymer/nanoparticle mixture next to a hard surface.

We can also employ a repulsive surface, with a potential of an integrated Lennard-Jones form:

$$V(z) = \frac{4\pi\varepsilon_{wi}}{45}\left(\frac{\sigma_{wi}^{12}}{z^9}\right) \qquad \textbf{Equation 3-5}$$

We took the surface-fluid interactions to be $\varepsilon_{wi} = 1$ for both polymers and particles, with $\sigma_{wi} = 1.25$ for both components. The results for this surface potential are shown in Figure 3-8. We see that the nanoparticles still preferentially segregate to the surface. Now however the surface free energies are $\Omega_s = 4.72\ kT$ for the polymer film and $\Omega_s = 5.51\ kT$ for the polymer/nanoparticle mixture, so now the added nanoparticles increase the surface free energy. Since the surface energies are positive, this is a system that would like to dewet the surface in the sense that the surface energy is higher than the bulk free energy.

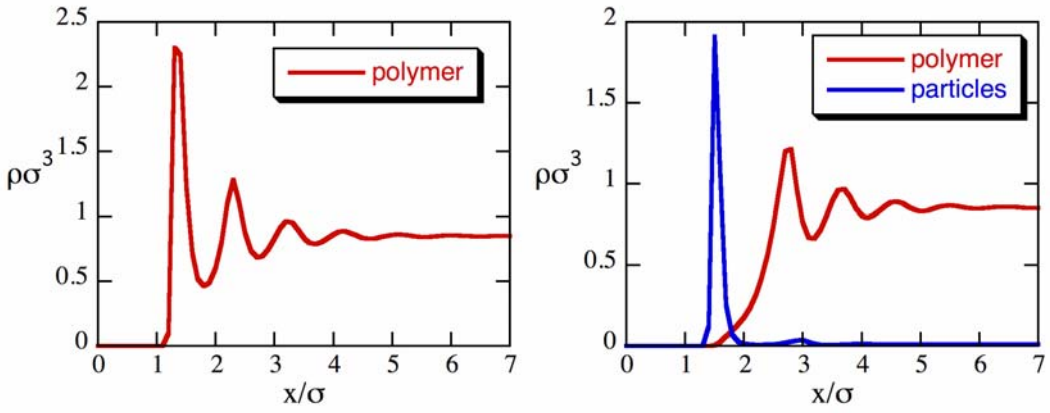

Figure 3-8. A polymer film and a polymer/nanoparticle mixture next to a repulsive Lennard-Jones surface. Note the lower contact densities compared to Figure 3-7.

These preliminary results are not sufficient to make any conclusions about the effects of nanoparticles on the stability of polymer films. These and other similar calculations do indicate that the nanoparticles tend to segregate to the surface, which has been hypothesized. This segregation must be entropic in nature. The presence of the surface reduces the configurational entropy of a polymer melt. It may be the case that the polymers can gain back some of that entropy if the particles pack near the surface. Packing entropy may also play a role here. This is what drives the polymer melt to a hard surface in the first place, and perhaps the packing is more efficient with the particles on the surface instead of the polymer chains, since the particles do not have connectivity constraints. It would thus be interesting to vary systematically the chain length and the nanoparticle size to investigate these effects in the purely entropic system.

Thus, there are many variables to be explored which could change the picture we have so far. These include: chain length dependence; size of the nanoparticles relative to the polymer monomers; interactions (i.e. if we include attractive interactions); interactions with the surface; total density; and composition. Another adjustment to the model would be to allow the bond length between monomers to be different from the monomer diameter σ, which would allow us to build a more accurate coarse-grained model. All of these variables could influence the results.

More fundamentally, the current version of the DFT we are using will not support a true wetting transition. This is because the approximate free energy used in the DFT is quadratic in form, so it cannot support two different solutions (i.e. polymer liquid and "vapor") at the same free energy. This shortcoming has been remedied by Muller et al., [21] and we could incorporate aspects of their free energy into our code. This would allow a closer mapping between the thermodynamic properties of our model polymer and the true experimental behavior.

4 Capillary wicking in micron-sized gaps

4.1 Introduction

Underfill is desired for direct-chip-attachment (DCA) applications, including “flip chip” technology, in which the chip is bonded to the substrate using solder bumps. This technology allows high interconnect density. The chips are underfilled with silica-filled epoxy to match the thermal coefficient of expansion of the solder.

Benefits of underfill include enhanced reliability from protection of the chip, solder bump joint and interconnect board, relief of thermal stresses, and minimization of fatigue. A schematic of an underfilled package is shown in Figure 4-1.

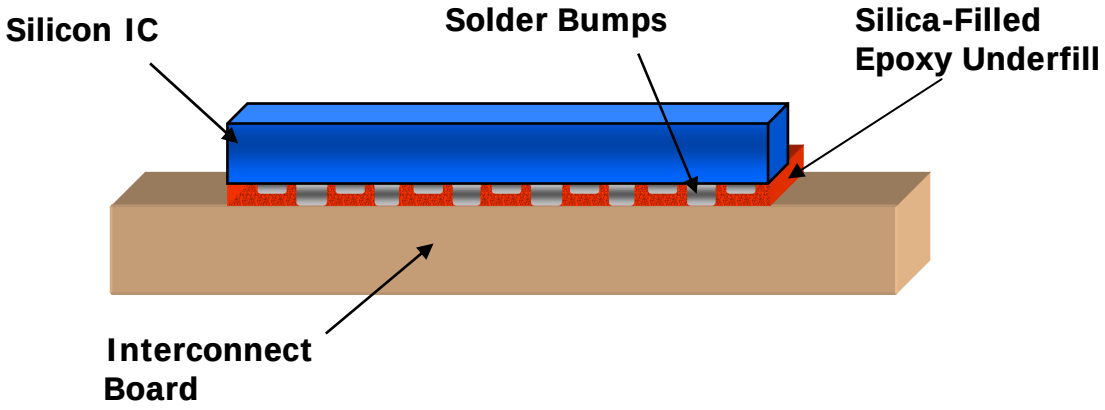

Figure 4-1. Schematic of an underfilled IC package.

The underfill process is driven by capillary action. Ideal flow of the underfill material can be modeled as laminar flow between parallel plates, as illustrated in Figure 4-2.

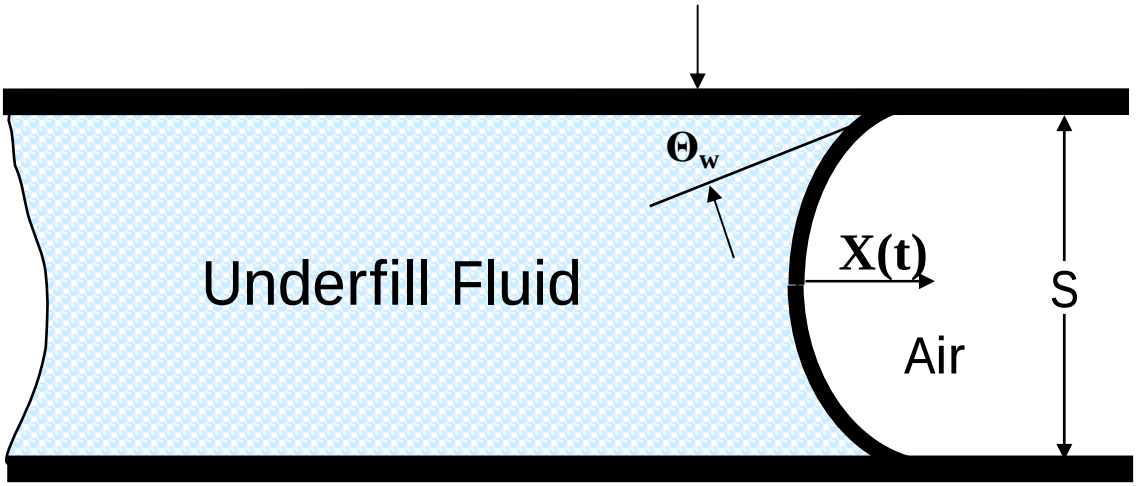

Figure 4-2. Schematic of the driving forces in capillary wicking between two plates.

Simple capillary flow of a Newtonian fluid in laminar, Poiseuille flow between two parallel plates is derived from basic equations and concepts. The mean speed of the fluid flow (U_m) is linearly proportional to the axial pressure gradient (dP/dx)

$$U_m(t) = -\frac{S^2}{12\mu}\frac{dP}{dx}. \qquad \textbf{Equation 4-1}$$

Equating the mean speed to that of the moving front (U_m=dx/dt) the position of the front is obtained as[22]

$$(1-K_r)\frac{X_f^2(t)}{2} + K_r L X_f(t) = \frac{\sigma[2\cos(\theta_w)]St}{12\mu}. \qquad \textbf{Equation 4-2}$$

Ignoring the presence of air (K_r=0) this simplifies to the Washburn equation,[23]

$$X_f^2(t) = \frac{\sigma\cos(\theta_w)St}{3\mu} \qquad \textbf{Equation 4-3}$$

where

$K_r=\mu_{air}/\mu$
L=channel axial length
$X_f(t)$=position of the liquid-air front at time t
S=plate separation distance
σ=surface tension
μ=viscosity of the underfill fluid
Θ_w=wetting contact angle.

Assumptions of the Washburn model include

- the fluid is continuous
- any filler material does not affect the flow
- viscosity, surface tension and wetting angle do not vary with time
- there are no effects from surface phenomena such as varying roughness.

With these assumptions in mind there is one important implication—X_f^2/t is a linear function of plate separation distance.

4.2 Results and discussion

In the following work, Brookfield silicone viscosity standards were wicked into fused silica capillaries. The standards used had viscosities of 98, 494, and 970 cp. A video camera attached to an optical microscope was used to record the liquid wicking into the capillary. The video tape was then reviewed to determine the wicking distance as a function of time. The square of the wicking distance is plotted as a function of time for each of three fluids in four different capillary diameters, Figure 4-3a-d.

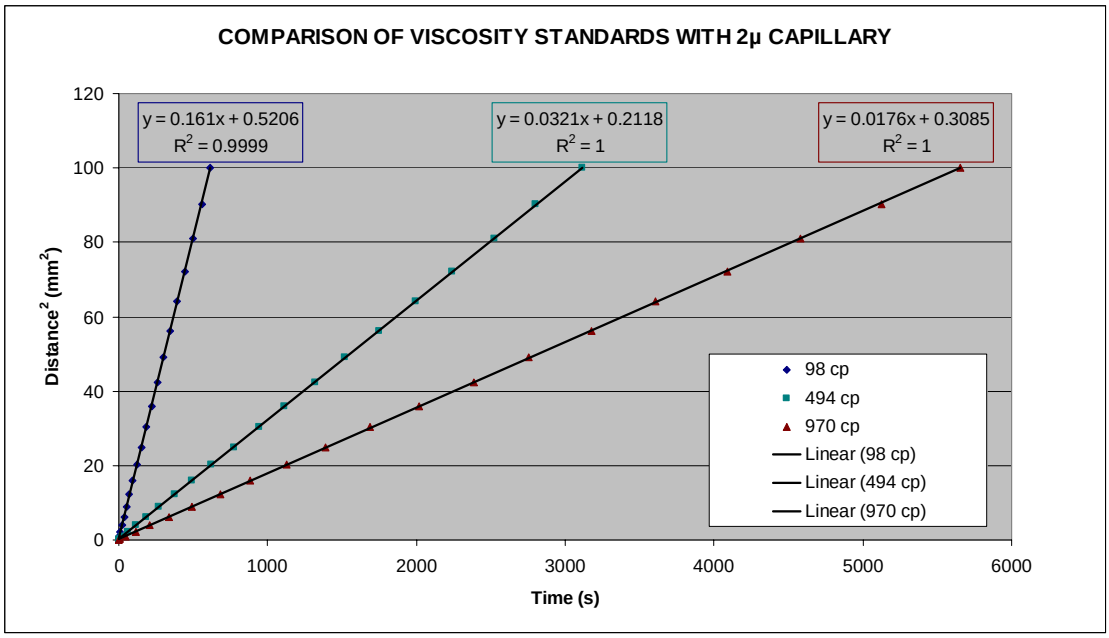

Figure 4-3a. Plots of capillary wicking data for three silicone viscosity standards in 2-micron diameter capillaries.

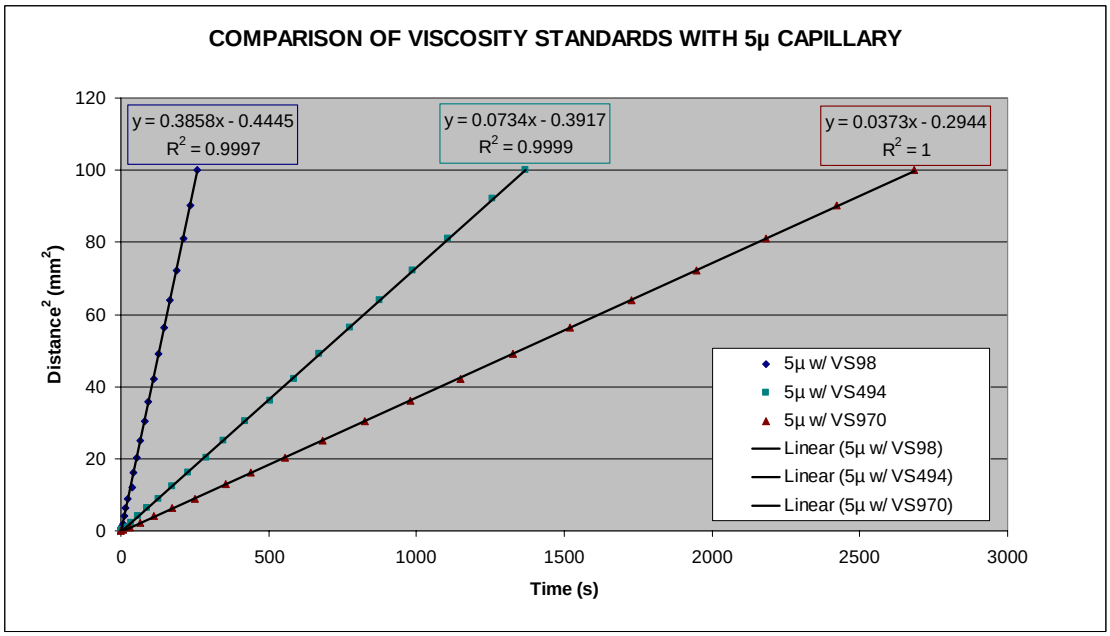

Figure 4-3b. Plots of capillary wicking data for three silicone viscosity standards in 5-micron diameter capillaries.

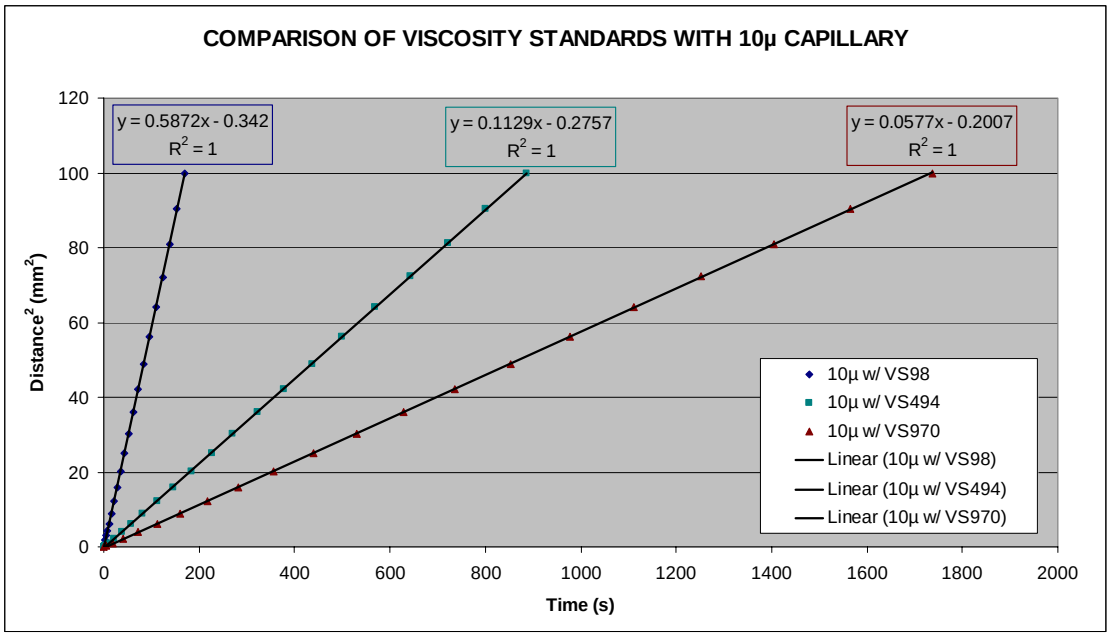

Figure 4-3c. Plots of capillary wicking data for three silicone viscosity standards in 10-micron diameter capillaries.

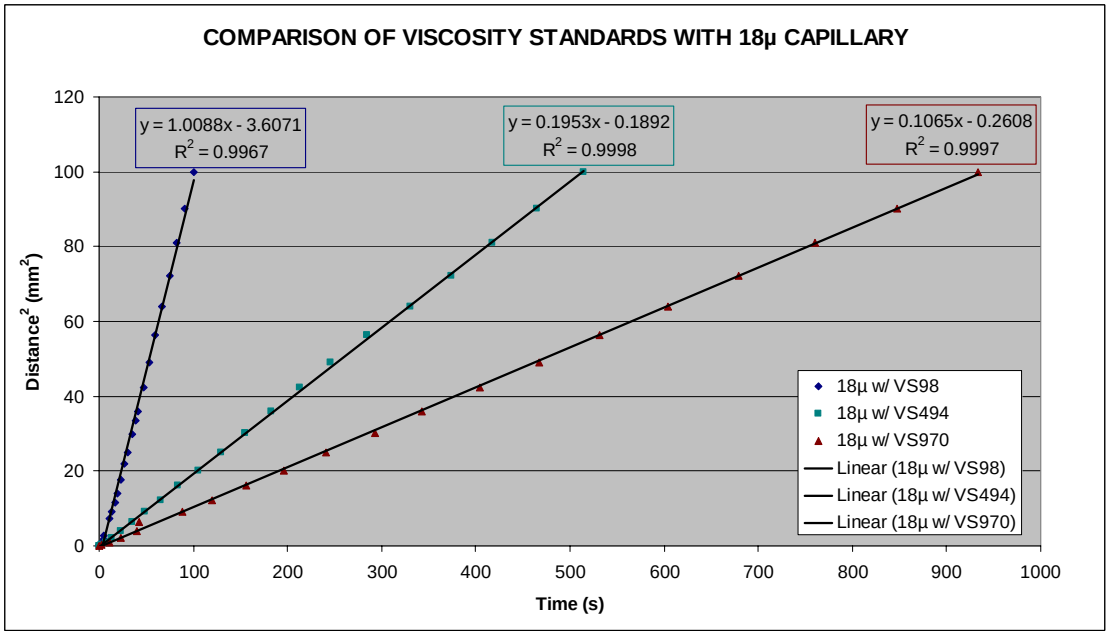

Figure 4-3d. Plots of capillary wicking data for three silicone viscosity standards in 18-micron diameter capillaries.

As can be seen in Figure 4-3a-d, the linear fit to the raw data is excellent. These data were compared to the predicted distance squared vs. time plots, using the Washburn equation. Plots of the experimental and curves predicted by the model are shown in Figure 4-4a-d.

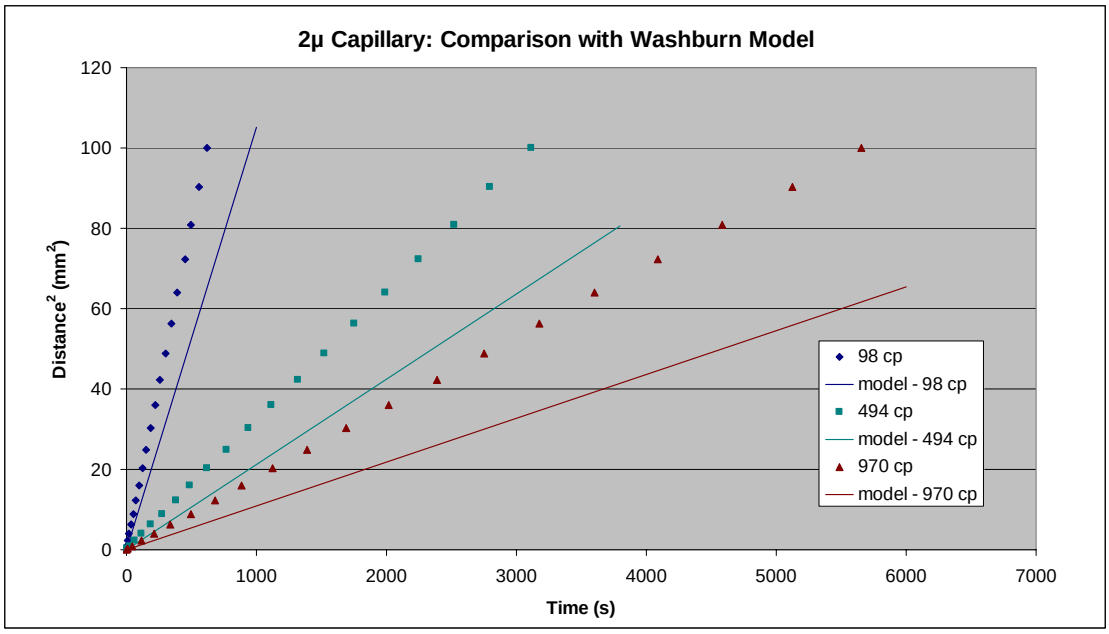

Figure 4-4a. Comparison of Washburn model with experimental data for silicone wicking in 2-micron diameter capillaries.

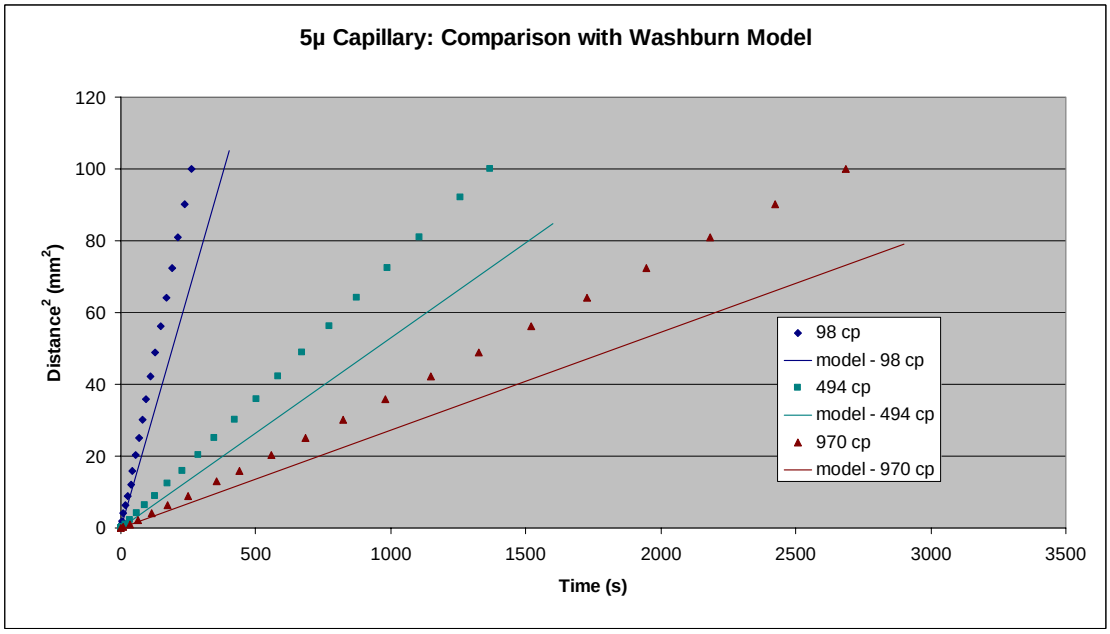

Figure 4-4b. Comparison of Washburn model with experimental data for silicone wicking in 5-micron diameter capillaries.

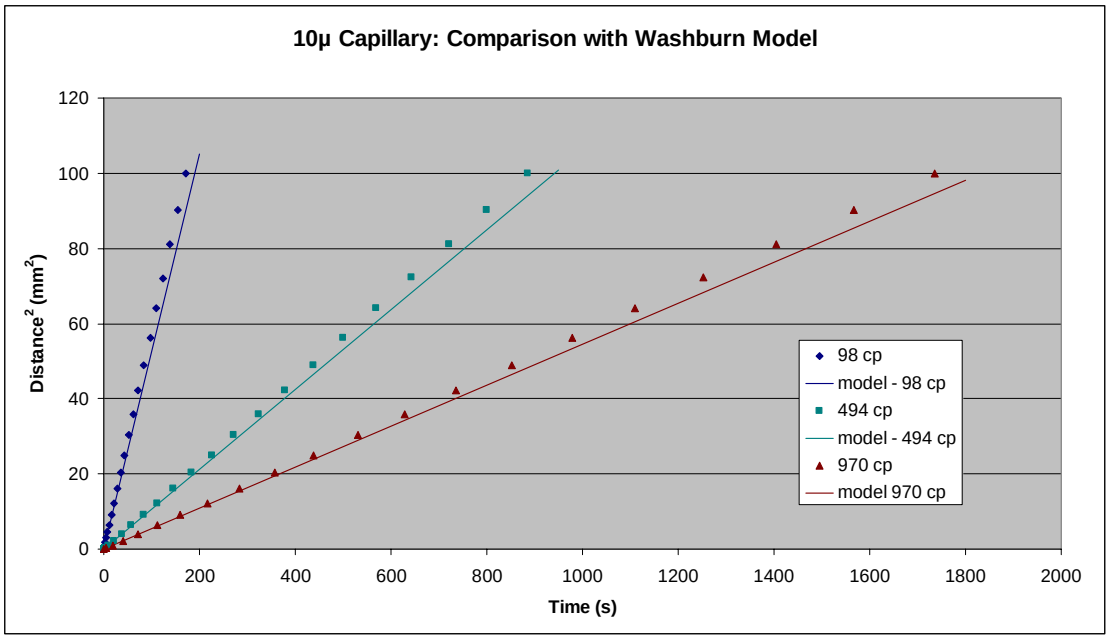

Figure 4-4c. Comparison of Washburn model with experimental data for silicone wicking in 10-micron diameter capillaries.

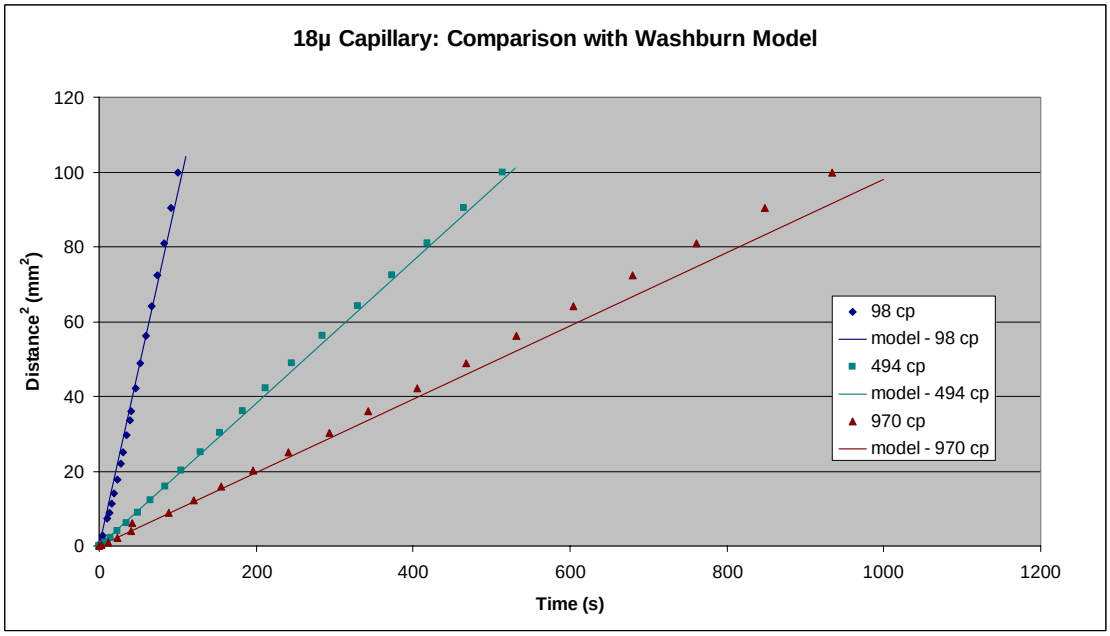

Figure 4-4d. Comparison of Washburn model with experimental data for silicone wicking in 18-micron diameter capillaries.

Although the fit of the model is fairly good for the 10 and 18 micron capillaries, it is poor for the 2- and 5-micron capillaries. To quantify this fit, we used the experimental data to back-calculate the surface tension of the silicone. The calculated surface tension is compared to the true surface tension of the silicone, 22 mJ/m^2, and is shown in Figure 4-5.

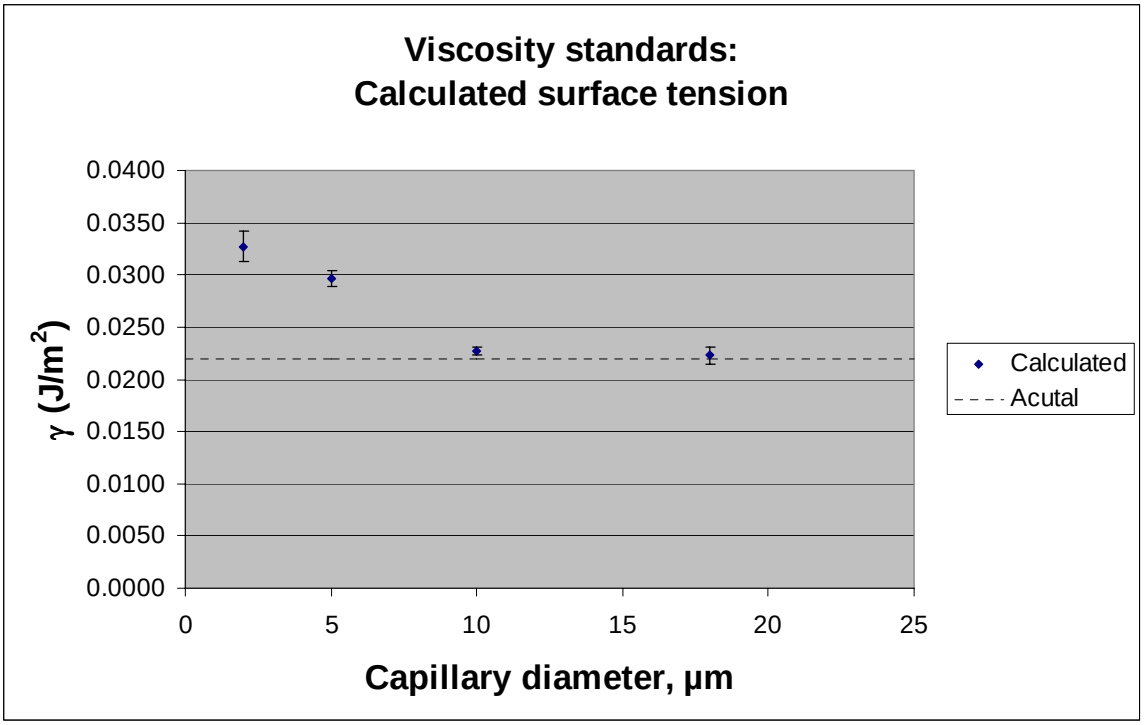

Figure 4-5. Comparison of surface tension, calculated from experimental data, with actual surface tension of silicone.

Note the trend of calculated surface tension increasing with decreasing capillary diameter, and of increased deviation from the actual value. Since the surface tensions of the liquids are not changing, the deviation suggests that the model used to calculate the surface tension is no longer valid at capillary diameters below ~10 µm.

Further investigation was necessary to validate this surprising result. To this point, the value used for capillary diameter was the value given by the manufacturer. SEM images of cross-sections of each capillary were used to experimentally verify the capillary diameters. In some cases, particularly in the smaller capillaries, significant deviations from the reported diameters were observed. The following table gives the reported and actual capillary diameters.

Table 4-1. Reported and actual diameters of capillaries.

Reported diameter (µm)	Actual diameter, by SEM (µm)
2	2.8
5	7.0
10	11.1
18	20.0

Comparisons with the Washburn equation were re-calculated with the corrected diameters, and are plotted in Figure 4-6a-d.

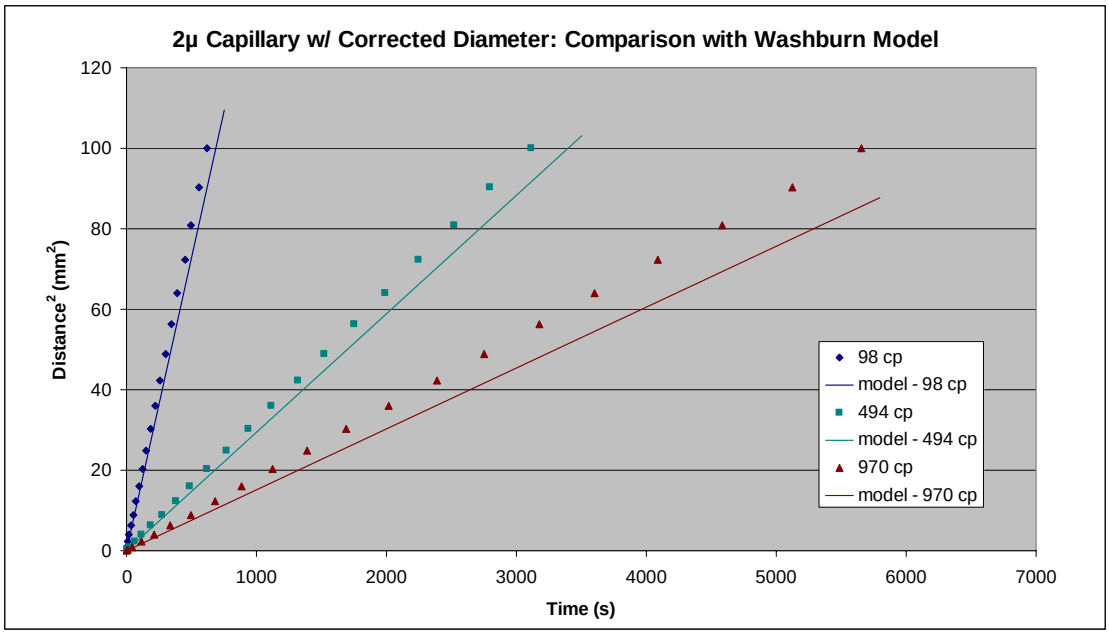

Figure 4-6a. Comparison of Washburn model, using corrected capillary diameters, with experimental data for silicone wicking in 2-micron diameter capillaries.

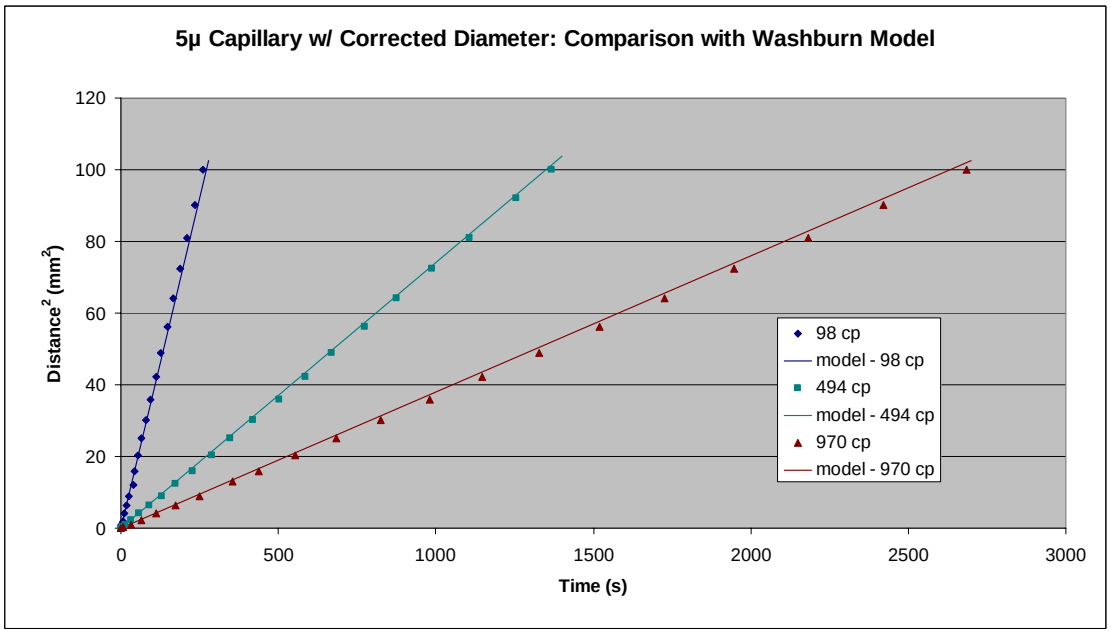

Figure 4-6b. Comparison of Washburn model, using corrected capillary diameters, with experimental data for silicone wicking in 5-micron diameter capillaries.

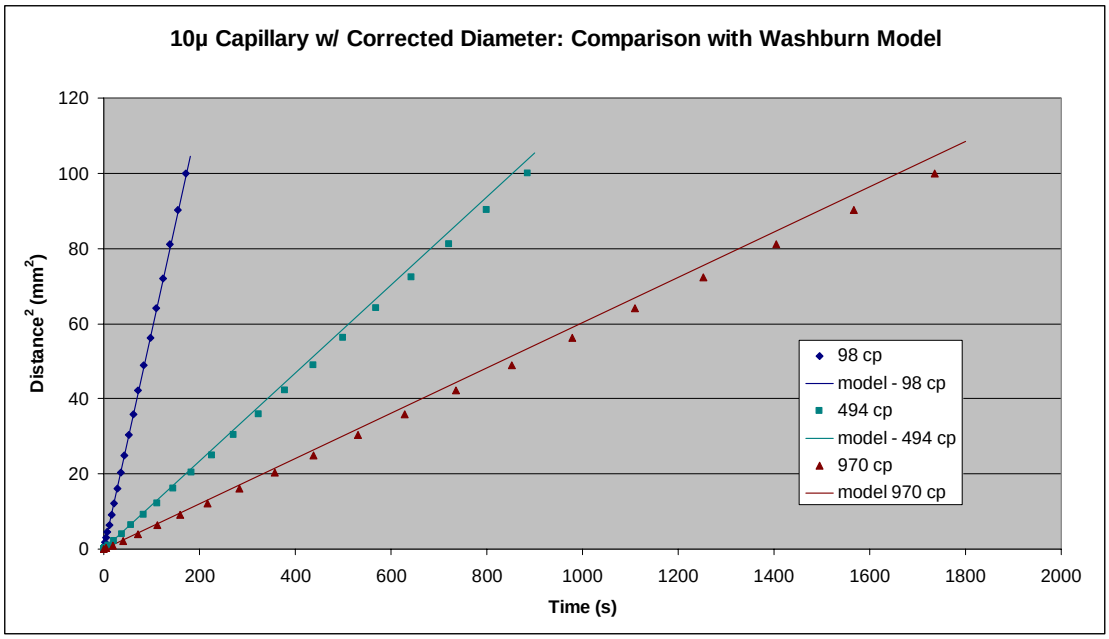

Figure 4-6c. Comparison of Washburn model, using corrected capillary diameters, with experimental data for silicone wicking in 10-micron diameter capillaries.

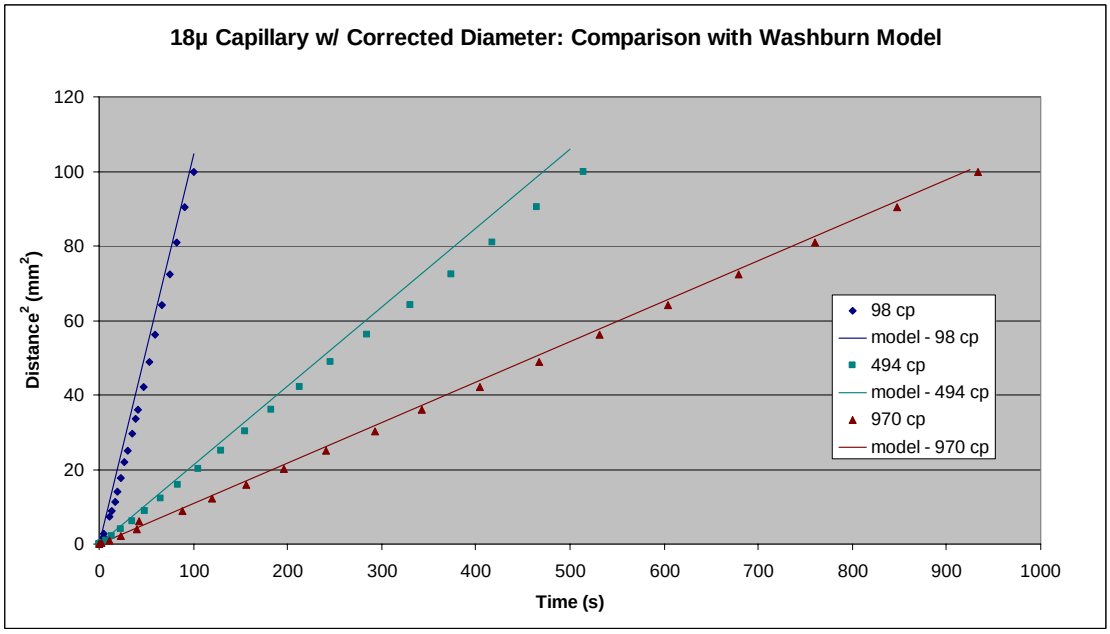

Figure 4-6d. Comparison of Washburn model, using corrected capillary diameters, with experimental data for silicone wicking in 18-micron diameter capillaries.

Although the fit is much better after applying the corrected diameters, the fit of the 2-micron data is still much worse than that of the larger capillaries. The comparison of actual and calculated surface tension values was repeated with the corrected capillary diameters, and is shown in Figure 4-7.

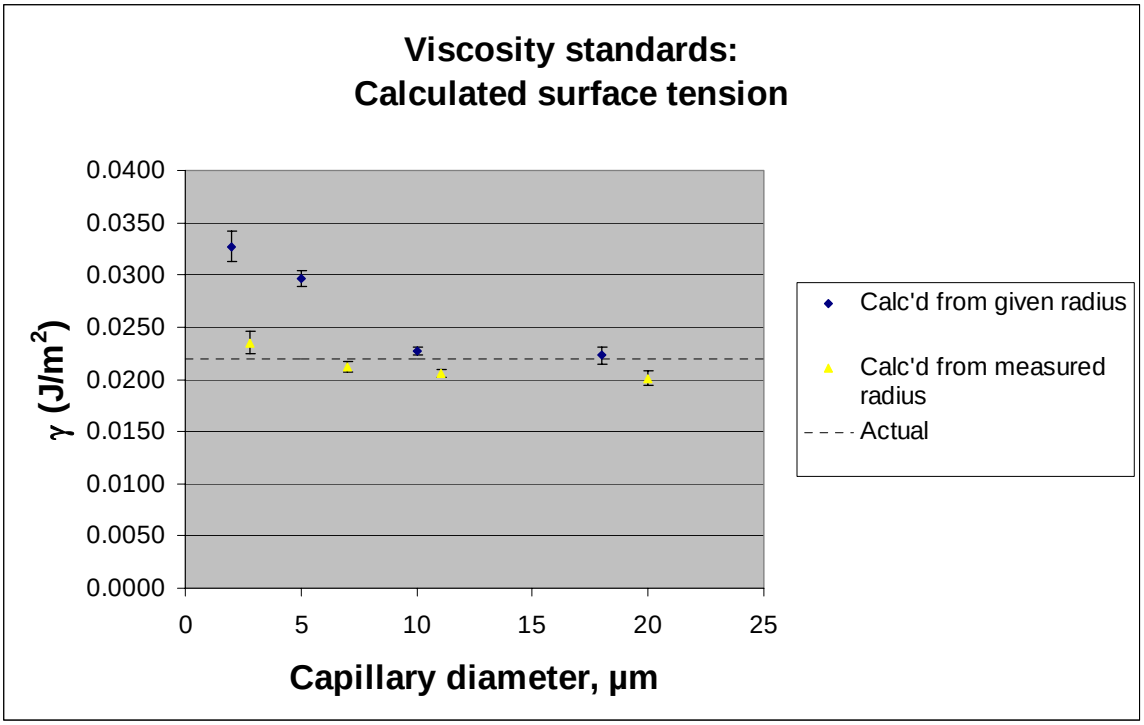

Figure 4-7. Comparison of surface tension, calculated from experimental data using the given and corrected diameters, with actual surface tension of silicone.

While the fit of the data calculated using the corrected diameters is much closer to the actual surface tension of silicone, a trend of increasing apparent surface tension with smaller capillaries still exists. To see if this trend is a true deviation of the Washburn equation in very small capillaries, capillaries with diameters below 2 microns would be required. Unfortunately, during the course of this work, we were unable to acquire capillaries with inside diameters smaller than 2 microns. If smaller capillaries could be acquired, future work in this area would be of great interest.

5 Summary and conclusions

This project focused on areas in which issues were arising with the use of adhesive bonding on the micro- and nano-size scales. Recommendations have been given regarding designing and fabricating thin films of adhesives and polymeric materials. The work described herein is expected to improve the reliability and manufacturability of micro- and nano-scale devices.

References

1. F. Brochard-Wyart, J. M. diMeglio, D. Quere, P. G. de Gennes, *Langmuir,* 1991, **7**, 335.
2. J. Israelachvili, *Intermolecular and Surface Forces*, 1992, Academic Press, London, p. 205.
3. R. Seeman, S. Herminghaus, K. Jacobs *J. Phys.: Condens. Matter*, 2001, **13**, 4925.
4. H Yim, M. Kent, W. F. McNamara, R. Ivkov, S. Satija, J. Majewski *Macromolecules,* 1999, **32,** 7932.
5. S. Wu *Polymer Interface and Adhesion*, 1982, Marcel Dekker, Inc, New York, p. 178.
6. I. T. Smith, *Polymer*, 1961, **2**, 95.
7. K. Shin, X. Hu, X. Zheng, M. H. Rafailovich, J. Sokolov, V. Zaitsev, S. A. Schwarz, *Macromolecules*, 2001, **34**, 4993.
8. A. L. Ducoffe, *J. Applied Phys*., 1953, **24**, 1343.
9. J. W. Grate, S. J. Patrash, S. N. Kaganove, B. M. Wise, Anal. Chem., 1999, 71, 1033.
10. W. P. King, T. W. Kenny, K. E. Goodson, G. Cross, M. Despont, U. Dürig, H. Rothuizen, G.K. Binnig and P. Vettiger, App. Phys. Let., 2001, 78, 1300.
11. J. W. Grate, R. A. McGill, Anal. Chem., 1995, 67, 4015.
12. M. E. Mackay, Y. Hong, S. Hong, T. P. Russell, C. J. Hawker, R. Vestberg, J. Douglas, Langmuir, 2002, 18, 1877.
13. R.S. Krishnan, M.E. Mackay, in preparation.
14. J. W. Grate, S. N. Kaganove, S. J. Patrash, R. Craig, M. Bliss, Chem. Mater. 1997, 9, 1201.
15. K. Barnes, A. Karim, J. Douglas, A. Nakatani, H. Gruell, E. Amis, Macromolecules, **33** (2000) 4177.
16. A. L. Frischknecht, J. D. Weinhold, A. G. Salinger, J. G. Curro, L. J. D. Frink, J. D. McCoy, *J. Chem. Phys.*, 2002, **117**, 10385.
17. K. S. Schweizer, J. G. Curro, *Adv. Polym. Sci.*, 1994, **116**, 319.
18. L. J. Fetters, D. J. Lohse, D. Richter, T. A. Witten, A. Zirkel, *Macromolecules*, 1994, **27**, 4639.
19. A. Brulet, F. Boue, J. P. Cotton, *J. Phys. II France*, 1996, **6**, 885.
20. K. A. Barnes, A. Karim, J. F. Douglas, A. I. Nakatani, H. Gruell, and E. J. Amis, *Macromolecules*, 2000, **33**, 4177.
21. M. Muller, L. G. MacDowell, P. Muller-Buschbaum, O. Wunnike, M. Stamm, *J. Chem. Phys*., 2001, **115**, 9960.
22. G. L. Lehmann, P. C. Li, E. J. Cotts, "Modeling the Underfill Flow Process," Proceedings of *Surface Mount International*, 1996.
23. E. W. Washburn, *Physical Review*, 1921, **17**, 273.

Distribution:

1	MS	0188	LDRD office, 1011
1		0888	S. T. Kawaguchi, 1811
2		0892	D. R. Adkins, 1764
6		0958	R. K. Giunta, 14172
1		0958	J. A. Emerson, 14172
1		0958	K. P. Lamppa, 14172
1		0958	J. A. Ruffner, 14172
1		0961	C. L. J. Adkins, 14101
4		1411	M. S. Kent, 1851
1		1411	J. S. Hall, 1851
1		1411	A. L. Frischknecht, 1834
1		1415	G. S. Grest, 1114
1		1421	D. H. Read, 1120
1		9018	Central Technical Files, 8945-1
2		0899	Technical Library, 9616